2014

# JOINING AND HERMETIC SEALING OF SILICON CARBIDE USING IRON, CHROMIUM, AND ALUMINUM ALLOYS

Andrew Morgan
*Virginia Commonwealth University*

# JOINING AND HERMETIC SEALING OF SILICON CARBIDE USING IRON, CHROMIUM, AND ALUMINUM ALLOYS

A thesis submitted in partial fulfillment of the requirements for the degree of

MASTER OF SCIENCE

by

**Andrew Morgan**

DIRECTED BY: DR. GOKUL VASUDEVAMURTHY
COMMITTEE CHAIR AND ASSISTANT PROFESSOR
MECHANICAL AND NUCLEAR ENGINEERING

Virginia Commonwealth University
Richmond, Virginia
July, 2014

# Acknowledgments

I am deeply indebted to my advisor, Dr. Gokul Vasudevamurthy, for his invaluable guidance and inspiration in the field of material science. I would like to acknowledge Dr. Karla Mossi for her friendly and supportive advice during my graduate research at Virginia Commonwealth University. I sincerely thank my research colleagues, James Carr, Caleb Massey, and Yonathan Kassaye for their assistance and help throughout my research. I express my gratitude to the faculty, staff, and students of the department of mechanical and nuclear engineering who have helped me in many ways. In particular, I am extremely grateful to Allison Bell who has made my entire journey somewhat bearable.

A special acknowledgment goes out to Dr. James McLeskey, who through his exciting and captivating lectures confirmed my passion for engineering. My research was greatly assisted by the staff and students at the Virginina Wright Microelectronics Center: Dr. Gary Atkinson, Joshua Starliper, Joshua Smak, and Zach Ashley. I am grateful to each of you for teaching me thin film deposition techniques and ultimately transforming me to an electron beam evaporator guru.

I am wholeheartedly grateful to Dr. Vishnu Sundaresan, who introduced me into academic research by taking me in as an undergraduate research assistant. Even when at a different institution, his continued support and advice was immeasurable. Finally, I am profoundly thankful for my girlfriend and my family for their enduring support and love throughout my entire college career.

# Contents

# List of Tables

# List of Figures

# List of Acronyms

**ATF** accident tolerant fuel

**BSE** backscatter electron

**CTE** coefficient of thermal expansion

**CVD** chemical vapor deposition

**DBA** design basis accident

**DF** dark field

**ECCS** emergency core cooling system

**EDS** electron dispersive spectroscopy

**GWe** giga-watts electric

**HT** heat treatment or heat treated

**LANL** Los Alamos National Laboratory

**LOCA** loss of coolant accident

**LWGR** light water graphite-moderated reactor

**LWR** light water reactor

**MFP** mean free path

**NITE** nano-infiltrated-transient-eutectic

**ORNL** Oak Ridge National Laboratory

**PVD** physical vapor deposition

**PWR** pressurized water reactor

**RIA** reactivity initiated accident

**SEM** scanning electron microscopy

**SBO** station black out

**TMI** Three Mile Island

**UHP** ultra high purity

# Abstract

JOINING AND HERMETIC SEALING OF SILICON CARBIDE USING IRON, CHROMIUM, AND ALUMINUM ALLOYS

By: Andrew M. Morgan, M.S.

A thesis submitted in partial fulfillment of the requirements for the degree of Master of Science

Virginia Commonwealth University, 2014
Directed by: Dr. Gokul Vasudevamurthy, Assistant Professor
Mechanical and Nuclear Engineering

Silicon Carbide (SiC) is increasingly gaining attention as a potential fuel cladding material, on account of its favorable thermo-mechanical and neutronic properties. The major limitations of such a cladding is currently associated with joining and hermetic sealing. The work presented here investigated the use of Al, Cr and Fe metals and a specialized alloy (FeCrAl) to achieve hermetic sealing of SiC tubes as well as a joining technology of SiC. Major part of solving this issue requires addressing joining of ceramic and metallic components, which are largely dissimilar in both thermal and mechanical properties. Preliminary experiments to bond SiC with FeCrAl resulted in adverse separation partially attributed to the differences in thermal expansion mismatch. To alleviate these problems, thin and thick coatings of the metals and alloys were applied to SiC. Qualitative microstructural characterization of the final product indicated satisfactory bonding between the materials.

# Chapter 1

# Introduction

## 1.1 Objective

This research investigates several methods of joining SiC to FeCrAl and SiC to aluminum as well as coating SiC in an effort to determine whether a hermetically sealed accident tolerant fuel (ATF) clad for light water reactors (LWRs) comprised of these materials is feasible. A hermetically sealed fuel clad would be impenetrable to gasses or liquids, which is critical for retaining fission products trapped in the fuel cladding. This work has been split up into three phases. In Phase I, outlined in Section 3.2, diffusion bonding of SiC to FeCrAl and SiC to aluminum using thin metallic inserts of FeCrAl and aluminum, respectively, was investigated. The purpose of this phase is to investigate if diffusion bonding can serve as a joining technology for SiC tubes. Here, the various combinations of temperature, hold time, and ramp rate were explored. Dip coating and casting of aluminum and FeCrAl onto SiC by induction heating was examined in Phase II, explained in Section 3.3. Dip coating and casting proves an economical solution of hermetically sealing SiC on a mass-production scale. Thin-film coatings deposited onto SiC by methods of magnetron sputtering and electron beam evaporation consisted of the first part of Phase III and is outlined in Section 3.4. In the second part of Phase III, the coated SiC specimens were then subjected to high-temperature diffusion bonding, as explained in Section 3.5. Optical microscopy,

scanning electron microscopy (SEM), and electron dispersive spectroscopy (EDS) were used to qualitatively characterize the experiments. The purpose of the coatings is twofold: first it provides hermetic sealing by saturating the porous SiC by thin films of dense alloys, second, it introduces compositional graded interlayers to reduce the coefficient of thermal expansion (CTE) mismatch between SiC and FeCrAl in an effort to join the materials.

## 1.2 Problem and Significance

The demand for nuclear power is increasing due to its clean and reliable characteristics. With the concern of increasing $CO_2$ emissions and oil prices, the world has considered nuclear power to address these issues. The emissions given off from nuclear power plants are significantly lower than those given off from fossil-fueled power plants [3]. Thirteen percent of the global electric demand is powered by nuclear energy. In the United States alone, 104 nuclear reactors produce 103 giga-watts electric (GWe), making it the largest producer of nuclear energy. Twenty percent of the Unites States' electric generation is supplied by nuclear energy. Based off these statistics, it is evident that nuclear power is a crucial resource, especially when considering the concern of greenhouse gas emissions [4]. An emerging area of research in regards to nuclear power is the material selection used for fuel cladding. With the combination of extreme temperatures and stress, the corrosive nature of water, and the radiation fluxes, material properties can easily degrade and cause severe accidents.

## 1.3 Current LWR Fuel Cladding

A typical fuel pin used in LWRs is shown in Figure 1.1. The fuel pin consists of fuel pellets, cladding material, a spring, an insulating pellet, and an end cap. As the fuel pellets are loaded into the pin, an insulating pellet is added to the top and are all compressed by a spring. The spring ensures that all fuel pellets are compressed together to prevent any vibration or movement. The plenum is the space occupied by the spring and exists for the accumulation of gasses. Finally, the

end cap seals the fuel pin to prevent any fission products and gasses from escaping into the coolant.

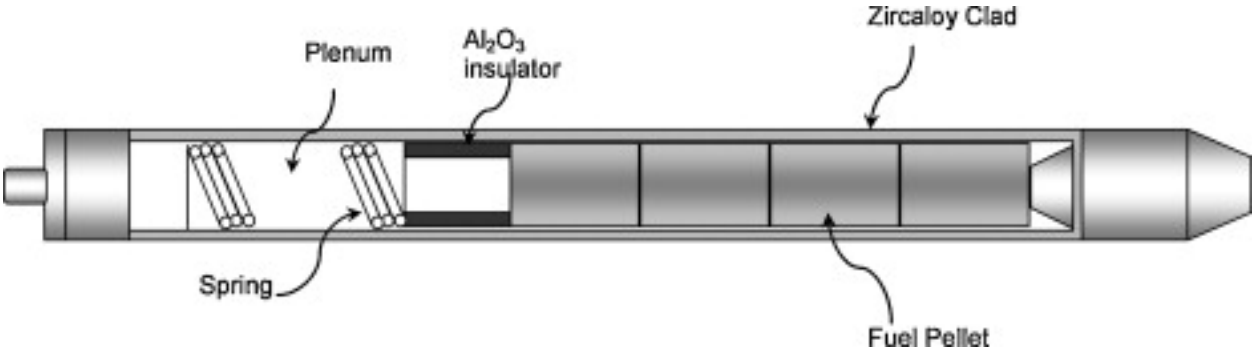


Figure 1.1: A Typical Fuel Pin used in LWRs, Obtained from [1]

There are different types of fuel cladding materials that have been studied for their failure mechanisms such as creep, pellet-clad interaction, and corrosion. These often occur in loss of coolant accident (LOCA) and reactivity initiated accident (RIA) scenarios. The material properties of a fuel clad must be able to withstand an extremely harsh environment. In addition, the clad tubes are subjected to corrosion since they are in contact with flowing water. A desired fuel clad will exhibit properties such as high strength, high thermal conductivity, good corrosion resistance, and a low cross-sectional area for neutron absorption. Since the 1950s, when stainless steel cladding became obsolete due to its susceptibility to high-temperature corrosion, zirconium based alloys have been adopted as the standard fuel cladding material. The two common zirconium alloys used are Zircaloy-2 and Zircaloy-4. These two alloys are composed of zirconium, tin, iron, and chromium in varying weight percentages with the addition of nickel is Zircaly-2. The addition of tin, iron, chromium, and nickel all contribute to the increased corrosion resistance of the alloy in high-temperature water and steam. Newer designs for fuel cladding, ZIRLO and M5 have implemented niobium to further increase the ability of the clad to withstand higher burn-up fuels [5]. While strength and corrosion resistance of zirconium-based fuel cladding have been enhanced, the hydrogen production associated with such cladding can lead to undesired consequences. The main source of hydrogen production in Zircaloy cladding is due to the oxidation that occurs from

the coolant-cladding interface. As shown in Equation 1.1,

$$Zr + 2H_2O = ZrO_2 + 2H_2 \tag{1.1}$$

for every mole of oxidized zirconium, two moles of hydrogen are produced. With hydrogen production occurring from the interaction between high-temperature zirconium and steam, there is a major concern for combustion that may occur if flammability criteria is met. Large pressure loads will result from combustion that may ultimately breach the containment [6, 7].

## 1.4 Fuel/Core Safety and ATF

With the discovery of new fuel and fuel clad designs that lead to enhanced reactor performance and higher burn-up, there exists a concern whether the aforementioned designs may not be suitable for the current fuel safety criteria. The current criteria, established in the 1960s and 1970s, have lived up to its expectations as no accidents have occurred as a result of inadequate safety criteria. There are three different types of fuel criteria defined by the Nuclear Energy Agency [8]. They are:

- Safety Criteria - Criteria imposed by the regulator. If preserved, safety criteria ensure that the impact of a design basis accident (DBA) on the environment is acceptable.
- Operational Criteria - Criteria specific to the fuel design and provided by the fuel vendor as part of the licensing basis. Operational criteria ensure that safety criteria are not violated.
- Design Criteria - Limits employed by vendors and/or utilities for fuel and core design. Design criteria are preserved during the normal operation and anticipated transients.

Certain events related to fuel safety criteria including pellet-cladding interaction, cladding oxidation/hydriding, pellet relocation and dispersal, and cladding embrittlement and fragmentation can affect the fuel and ultimately lead to core degradation. During an accident, the ability to cool the core is inhibited by different causes such as pump failure or pipe breaks. With no active coolant,

the remaining coolant evaporates from the decay heat, leading to higher fuel temperatures [9]. The rate at which this happens can be anywhere from seconds to hours based on whether it's a small or large break LOCA, or an station black out (SBO), in which there is no external power to operate the pumps. As the fuel temperature quickly rises to around 800 °C, many physical and chemical degradation events arise in the core. For example, in the temperature range of 700-1200 °C, the current $UO_2 - Zr$ fuel rods will start to burst and release fission products into the coolant [10]. Usually in the scenario in which depressurization occurs from coolant boiling off, the emergency core cooling system (ECCS) is enabled. However, in the event that the ECCS is not operational, the excess steam will cause hydrogen production from the reaction of high-temperature zirconium and steam [7, 11]. This is explained in more detail in Section 1.3. If temperatures reach and/or exceed 1500 °C, severe core degradation is expected and the primary focus shifts to the containment integrity threatened by possible explosions [9].

Swift fuel pellet expansion against the cladding can occur in $UO_2 - Zr$ systems during RIA events. This can lead to fuel cladding failure and, in severe cases, complete core disruption [9, 12]. In current pressurized water reactors (PWRs), reactor feedback mechanisms are used to prevent unwanted RIA events from occurring. If a power upsurge occurs, the reactor will produce fast negative reactivity feedback to allow extra time for the safety systems to engage and shut the reactor down [12]. The largest and most devastating nuclear accident resulting from reactivity initiation was in Chernobyl, Ukraine on April 26, 1986, where reactor 4 was completely disrupted. Reactor 4 of the Chernobyl plant was a light water graphite-moderated reactor (LWGR), which lacked a containment building as well as the reactor feedback mechanisms used in current PWRs [12, 13]. The immediate effects of RIA events are an increase in power and thus fuel temperature. As fuel temperatures rise, similar consequences arise as that during a LOCA.

These failure modes previously mentioned provide motivation to investigate ATF. By employing materials with higher melting temperatures and reduced oxidation rates, many of these detrimental processes can be delayed if not avoided. The primary goal of ATF is to allow extra time for operators to properly respond to the situation and to alleviate the burden of reactor safety

systems [12].

## 1.5 Recent Developments in Advanced ATF for LWRs

The idea of replacing metal cladding with ceramic composite materials began to emerge after the core meltdown that occurred in Three Mile Island (TMI). Early studies considered the use of a composite consisting of alumina fibres and an alumina matrix. The composite would reduce the rate of ballooning, which could ultimately block coolant flow. Thus the fuel would not have melted and core replacement would have been feasible. However, it was later determined that the strength of the clad was compromised upon irradiation and that the clad was not hermetic—it was permeable by fission gasses [14]. One area of interest in researching ATF is to increase performance metrics in areas such as high burn-up to reduce waste, increase power density, and increase fuel reliability. While ATFs still desire these characteristics, the Fukushima-Daiichi nuclear power plant accident focused on other performance characteristics under severe accidents such as reduced hydrogen production. Both the Fukushima and TMI accidents resulted from a loss of cooling to the reactor due to the ballooning of the Zircaloy fuel clad [15]. Currently, the development of advanced ATFs are under way and are directed by national laboratories and joint efforts from industry and universities across the United States [16]. The following outlines research efforts of advanced ATF cladding only, as the scope of this thesis is limited to fuel cladding rather than the fuel system (fuel + clad).

Advanced ATF materials include advanced steels, refractory metals, ceramic composites, and Zircaloy with innovative coatings. Alloys consisting of Fe, Cr, and Al (FeCrAl) and SiC materials are being developed for oxidation and irradiation tests by Oak Ridge National Laboratory (ORNL) and Los Alamos National Laboratory (LANL). A study conducted by ORNL investigated the oxidation kinetics of SiC-based materials, stainless steel with high Cr and Al content, and FeCrAl alloys. The testing materials consisted of $1-2$ *mm* thick specimens of chemical vapor deposition (CVD) SiC, nano-infiltrated-transient-eutectic (NITE) SiC, FeCrAl alloy PM2000, Fe-Cr

alloys with varying Cr content of 15, 20, and 25%, Zircaloy-2 and Zircaloy-4, and stainless steel specimens 304L, 317L, 321L, and 347. The specimens were subjected to an exposure of 100% steam for 8 hours at temperatures of 800, 1000, and 1200°C. The results indicated that the Zircaloy specimens were heavily oxidized at 800 and 1200 °C. The stainless steel members all exhibited similar oxidation, the least of which was 317L. However, at 1200 °C, half of the 317L specimen was oxidized. The two materials that had the least oxide formation from an exposure at 1200 °C was the CVD SiC and the PM2000 FeCrAl alloy, with the CVD SiC forming more than twice the oxidation than the PM2000 [17] (See Section 1.6.4 for oxidation studies on SiC). The use of SiC in LWRs is discussed in the following section.

## 1.6 SiC in LWRs

Since the development and optimization of zirconium alloys for the use of LWR fuel cladding, it has been shown that zirconium based fuel claddings perform reliably. However, with the zirconium burn-up limit of 62 MWd/kgU, the nuclear industry is looking at employing higher burn-up materials. SiC, a potential, ceramic, alternative fuel cladding material can achieve higher burn-up and increased power uprates. More importantly, the material properties of SiC would allow longer safety margins at LOCA and RIA scenarios [18, 19]. Some of the key advantages with SiC cladding compared to zirconium based materials are: lower thermal neutron absorption, minimal hydrogen generation, high-temperature strength retention, high-temperature oxidation resistance, and slower degradation in accident scenarios [20]. The following subsections outline the material properties of SiC. The phase diagram of SiC is shown in Figure 1.2.

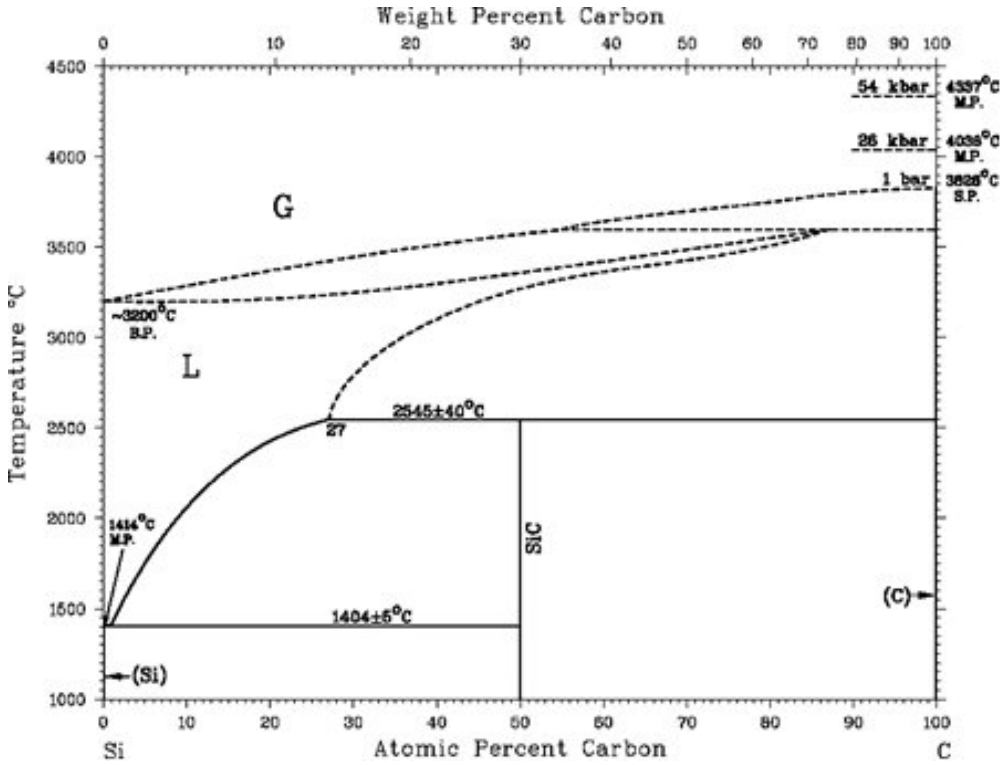


Figure 1.2: The C-Si Phase Diagram

### 1.6.1 Crystal Structure of SiC

The fundamental structural unit in SiC is a covalently bonded primary co-ordination tetrahedron (either $SiC_4$ or $CSi_4$), where a silicon atom is surrounded by four carbon atoms or vice versa [21]. Because of the various possibilities of atomic plane stacking, there are multiple polytypes of SiC [22]. The most abundant polytypes are 3C, 4H, 6H, and 15R. The number indicated in the polytypes indicates the periodicity of the bilayer as represented by the Ramsdel notation. The trailing letters C, H, and R represent the types of crystal, being cubic, hexagonal, and rhombohedral, respectively.

### 1.6.2 Material Properties of SiC

SiC is fabricated by different methods, which results in varying properties. In general, SiC exhibits properties such as high strength, high thermal conductivity, extreme hardness (up to 50% harder

than Tungsten Carbide), excellent corrosion resistance, and a low CTE. Table 1.1 compares various material properties of different types of SiC produced by Saint-Gobain Ceramics.

Table 1.1: Material Properties of Hexoloy Grades SiC

| Material | Hexoloy SA | Hexoloy SP | Hexoloy SE | Hexoloy SG |
|---|---|---|---|---|
| Grain Size, $\mu m$ | 4-10 | 4-10 | 4-10 | 4-10 |
| Density, $g/cm^3$ | 3.10 | 3.04 | 3.05 | 3.00 |
| Hardness* (Knoop), $kg/mm^2$ | 2800 | 2800 | 2800 | 2800 |
| Flexural Strength** 4 pt @ 21°C, $MPa$ | 380 | 240 | 280 | 311 |
| Modulus of Elasticity @ 21°C, $GPa$ | 430 | 400 | 420 | - |
| Poisson Ratio | 0.14 | 0.14 | 0.14 | 0.17 |
| Fracture Toughness @ 21°C, $MPa-m^{1/2}$ | 4.60 | 4.30 | 4.60 | 3.90 |
| Thermal Conductivity @ 21°C, $W/mK$ | 125.6 | 110.0 | 157.3 | 118 |
| CTE, up to 700°C, $10^{-6}mm/mmK$ | 4.02 | 4.20 | 4.02 | 4.60 |
| Max Service Temperature, $^{\circ}C$ | 1900 | 1900 | 1900 | 1900 |
| Mean Specific Heat @ 21°C, $J/gmK$ | 0.67 | 0.59 | 0.67 | 0.65 |
| Apparent Porosity, % | <2.0 | - | $5-10$ | - |
| Electrical Resistivity @ 21°C, $\Omega-cm$ | $10^2-10^8$ | - | $10^2-10^8$ | $1.0-10.0$ |

* Knoop $0.1kg$ load

** Test Bar Size: 3 x 4 x 45 mm

### 1.6.3 Joining SiC for ATF Applications

Joining SiC to SiC or to other materials has been performed by different methods. Techniques such as reaction bonding, the pyrolysis of perceramic polymers, glass-ceramic joining, and metallic brazing have all been accomplished [23, 24]. In reaction bonding, carbon is infiltrated with molten silicon to form SiC [25]. $SiC/SiC_f$ ceramic matrix composites were joined by high-temperature pyrolysis of a preceramic polymer [26]. In most of these methods, interlayer materials and active fillers are added for two main reasons, increasing the bond strength and lowering the processing conditions such as temperature and pressure. However, in nuclear applications, diffusion bonding using reactive metal foils is the most promising method. Metal diffusion bonding methods typically

consists of a thin metallic foil pressed between two plates of SiC, which would be heat-treated at temperatures above 1200 °C. These diffusion bonding experiments have been accomplished with materials such as titanium, molybdenum, and chromium [27, 28, 29]. Even with this excellent joining method, there still remains a challenge of achieving hermeticity, specifically at the tube-cap interface, to prevent any fission products or byproducts of escaping into the coolant. Stempien *et al.* reports that two samples that were bonded via a 10 $\mu m$-thick Ti foil pressed between two Hexoloy SA SiC blocks under 30 MPa later debonded after being irradiated for one and a half months at operating PWR conditions [30]. It was determined that swelling occurs in SiC at an irradiation temperature of 300 °C by the vacancy and interstitial point defects [24].

### 1.6.4 SiC Oxidation under Simulated PWR Conditions

Studies on the oxidation kinetics of SiC have been conducted for both-short and long-term exposures. The majority of these studies were long-term exposures (>500 hr.), in which SiC was subjected to a relatively low pressure (<0.1 MPa) in a wet air environment. Under these conditions, SiC exhibits an amorphous $SiO_2$ layer on the exposed surfaces [31, 32, 33]. Park *et al.* investigated the long-term corrosion behavior on CVD SiC from simulated PWR conditions. The CVD SiC measured 20 x 20 x 3 mm and was obtained my Morgan Technical Ceramics. Half of the specimens were initially oxidized in air at 1000 °C for 2 hours to investigate the effect of an $SiO_2$ surface pre-oxide layer. The specimens were exposed to a pressure of 18.5 MPa at 360 °C for 90 days. The results indicated that the pre-oxide layer reduced the dissolution of SiC in water at 360 °C. There, however, exists an uncertainty due to the fact that the $SiO_2$ layer can dissolve in water at relatively high temperatures. It was also observed that there was no acceleration behavior in the PWR simulation loop over the 90 day cycle [34]. A series of tests conducted by Cheng and Tortorelli examined the short-term (<48 hr.) oxidation behavior of CVD SiC under high pressure pure steam (0.34-2.07 MPa) at temperatures between 1000-1300 °C. The specimens exhibited a dual-layer $SiO_2$ scale, the inner layer being a dense amorphous $SiO_2$ and the outer layer revealed a porous cristobalite. It was noted that increased temperatures lead to accelerated diffusion and the

formation of the amorphous inner layer, while the thick cristobalite layer was attributed to extreme pressures [31].

# Chapter 2

# Theory

## 2.1 Diffusion

It is imperative to review the theory of diffusion to understand the variables and mechanisms that influence the feasibility of bonding. Diffusion is the mechanism of material transport facilitated by atomic motion. To grasp a basic understanding of diffusion between two materials, consider a diffusion couple that consists of two metals whose faces are in direct contact with each other. As the materials are heated for a certain time interval at a high temperature, atoms from each material will diffuse into each other, creating an intermediate alloyed region. This simple process is known as interdiffusion. There are many variables that determine whether diffusion can occur, however the main criteria to facilitate diffusion is that there must be a vacant, adjacent lattice site and the atom must possess enough energy to break the atomic bonds to allow atom displacement. The two main diffusion mechanisms related to metallic diffusion of different materials are vacancy diffusion and interstitial diffusion. Vacancy diffusion is the process when one atom moves from its original lattice position to an adjacent empty lattice site, or simply a vacancy. Vacancies are defects in materials, thus the rate of vacancy diffusion is correlated to the number of vacancy defects present in the material. As vacancy diffusion occurs, the migrating atom introduces a vacancy during the process. The other mechanism is interstitial diffusion, which involves smaller

atoms that jump from an interstitial site to another adjacent interstitial site. Interstitial diffusion occurs more frequently as it is easier for smaller atoms to jump to interstitial sites since the bond energies are lower and there more interstitial sites than there are vacancies. Interstitial atoms are usually carbon, hydrogen, nitrogen, and oxygen. The diffusion mechanisms are schematically illustrated in Figure 2.1.

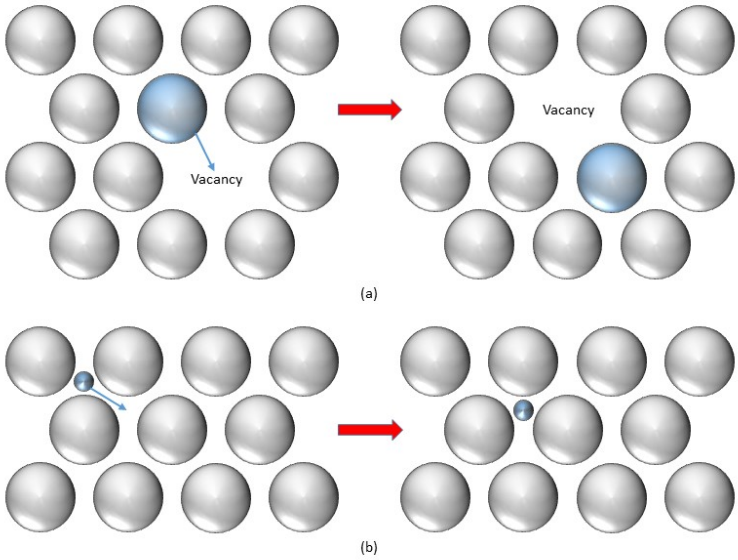


Figure 2.1: (a) Vacancy Diffusion and (b) Interstitial Diffusion

### 2.1.1 Laws that Govern Diffusion

The rate of mass transfer during diffusion, or the diffusion flux (J), is defined as the mass of the atoms (M) diffusing though unit area (A) per unit time (t). This is represented mathematically as

$$J = \frac{M}{At} \tag{2.1}$$

More often than not diffusion flux changes with time, but in some cases where it does not, steady-state diffusion occurs. In steady-state diffusion, the concentration of the diffusing atoms are constant. As the concentration is plotted against position, the concentration profile is obtained. In

steady-state diffusion, the concentration profile is linear. The slope at any point of the concentration profile results in the concentration gradient, which is defined as

$$J = \frac{dC}{dx} \cong \frac{\Delta C}{\Delta x} = \frac{C_A - C_B}{x_A - x_B} \tag{2.2}$$

Finally, the flux is proportional to the concentration gradient and is scaled by the diffusion coefficient, D. This expression, shown in Equation 2.3, is known as Fick's first law and is expressed as

$$J = -D\frac{\Delta C}{\Delta x} \tag{2.3}$$

The negative sign in Equation 2.3 denotes that diffusion is from high to low concentration. In most cases, the atoms will relocate themselves so that the concentration gradient changes over time. This common scenario causes the net flux to change over time, which is known as nonsteady-state diffusion. These types of problems are modeled by the partial differential equation

$$\frac{\partial C}{\partial t} = \frac{\partial}{\partial x}\left(D\frac{\partial^2 C}{\partial x^2}\right) \tag{2.4}$$

Equation 2.4 is often referred to as Fick's second law. To solve this expression, appropriate boundary conditions must be specified. One common solution is for a semi-infinite solid shown in Equation 2.5, in which the surface concentration, $C_s$, is constant at the surface ($x = 0$).

$$\frac{C_x - C_0}{C_s - C_0} = 1 - erf\left(\frac{x}{2\sqrt{Dt}}\right) \tag{2.5}$$

Here, $C_x$ and $C_0$ represent the concentration at depth $x$ after time $t$ and the concentration at $t = 0$, respectively. The $erf$ function is the Gaussian error function.

### 2.1.2 Parameters that Influence Diffusion

There are three main factors that influence diffusion. They are diffusing material, temperature, and bonding type. Based off the diffusing material and the parent or host metal, a temperature-independent coefficient is obtained. This coefficient has a proportional relationship to the diffusion rate. The most significant factor influencing diffusion is the temperature. The equation for the diffusion coefficient, D, is

$$D = D_0 \exp\left(-\frac{Q_d}{RT}\right) \tag{2.6}$$

where $D_0$ is the temperature-independent diffusion coefficient based off the host and diffusing materials ($m^2/s$), $Q_d$ is the activation energy for diffusion ($J/mol$, $eV/atom$, or $cal/mol$), $R$ is the universal gas constant ($J/mol-K$, $eV/atom-K$, or $cal/mol-K$), and $T$ is the temperature (K). It is evident that temperature plays a significant role in diffusion since it is coupled in the exponential term. The activation energy is indicative to the types of diffusion that may occur. Surface diffusion requires the least amount of activation energy and it is the movement of atoms along the lattice sites present on the material's surface. The next type of diffusion is grain boundary diffusion, which requires slightly higher activation energies than surface diffusion. It is the movement of atoms along grain boundaries, which generally are areas of high disorder. Finally, volume diffusion is the movement of atoms within the crystal structure and requires very high activation energies [35, 36, 37, 38, 39, 40].

## 2.2 Diffusion Bonding

Joining solid materials, whether similar or dissimilar, is typically carried out by two broad methods, which are fusion welding and pressure welding. In fusion welding, the edges of the material to be joined are melted to form a permanent joint. While this method is very useful in structural applications, it is not practical in joining metals to ceramics or other nonmetals. Furthermore, the welding process is carried out at extreme temperatures, which may affect the properties of the material in the weld area. Pressure welding is generally defined as the process of forming a joint

at temperatures below the melting point of the materials in the composite. There is no filler metal or solder being used in these processes, thus no weight is added to the material during joining. Diffusion bonding, also referred to as pressure joining, autovacuum welding, thermo-compression welding, solid-state welding, solid-phase welding, hot pressing, or sandwich pressing, is carried out in moderate temperatures and pressures, which result in materials with a longer service life. Diffusion bonding is the process of forming a joint by which atoms diffuse through the interface creating atomic bonds at the mating surfaces. The success of bond formed by diffusion bonding is affected mainly by three parameters: bonding temperature, bonding pressure, and hold time. Recommended operating parameters for bonding temperature is around 50% to 70% of the melting temperature of the highest fusible metal in the composition. This temperature range assists in the interdiffusion of atoms along the interfaces. The bonding pressure should be high enough so that a tight and firm contact is made between the mating surfaces. This will allow the voids to be filled in the weld area in addition to dispersing any oxide films from forming during heating. The hold time should be long enough to allow diffusion processes to take place but short enough to prevent any intermetallic phases from forming. Intermetallic phases that form from joining dissimilar materials are brittle layers that reduces the integrity of the bond.

There are several hypotheses that have been commonly accepted, which explain how solid-state diffusion bonding occurs. S.B. Ainbinder *et al.* proposed the Film Hypothesis that claims the integrity of the bond is attributed to the surface film characteristics. In this hypothesis, all metals and alloys are identical in terms of the ability to bond if properly clean surfaces are brought together in the range of interatomic forces. Another hypothesis, the Recrystallization Hypothesis, signifies the recrystallization process as the dominant factor in bonding. This theory suggests that atoms move from their lattice site to other sites as a result from deformation and subsequent strain hardening. Eventually, new grains start to grow at the grain boundaries and the bond is formed. In the Energy Hypothesis, the atoms of the metals or alloys to be joined must reach a threshold energy of adhesion in order for diffusion bonding to occur. At this energy, metallic bonds form at the interface, followed by annihilation of the interface. According to the Dislocation

Hypothesis, dislocations move to the surface as a result from plastic deformation. This causes present oxide films to decompose, producing consecutive interatomic steps. The result is bond formation from plasticity of the metal within the weld area. Finally, the most accepted theory, the Diffusion Hypothesis, relies on the interdiffusion of atoms into the bulk material. The surfaces of the materials have vacancies, which will accommodate diffusing atoms.

The general process of diffusion bonding follows a sequence of steps. First, it is assumed that the mating surfaces are as smooth as achievable by grinding and polishing the materials accordingly. The materials then come into contact, which is followed by the dispersion of surface oxide films. Plastic deformation occurs and the surface films are initiated. Finally, volumetric diffusion takes place and recrystallization follows leading to the formation of vacancies and interstitials [41].

## 2.3 Thick Film Coatings

There are two technical areas that are relevant to thick film coatings, which are wetting phenomena and dip coating, each with its own theoretical background. These areas govern the processes that occurs in dip coating and casting. The only difference between the dip coating and casting experiments is that dip coating involves removing the specimen in a delicate and precise manner, while casting remains in the molten pool during cooling. A brief theory of induction heating is included as it is the heating source to generate the molten metal.

It is well documented that for a ceramic to be infiltrated by liquid metal in such a way to facilitate proper adhesion, good wetting and low reactivity are required [41, 42, 43]. The distribution of liquid or molten metal on solids is known as wetting. In most cases, wetting is measured by the Sessile Drop Method, in which a drop of liquid is introduced to a solid flat surface. Based off the geometry of the droplet as it meets the substrate and the angle between the tangent of the drop's surface where it intersects the substrate (contact angle), it can be determined whether the material is wetted or not. As shown in Figure 2.2, if the contact angle, $\theta$, is less than $90^{\circ}$, the substrate is wetted, otherwise it is not [43].

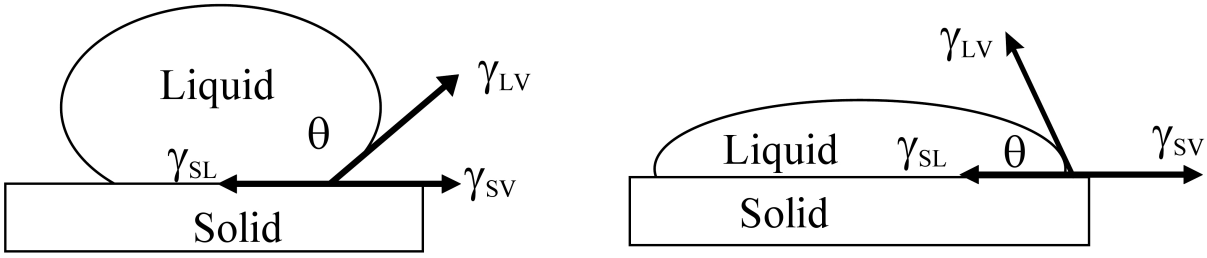


Figure 2.2: A Typical Sessile Drop Showing Poor Wetting (Left) and Good Wetting (Right), Obtained from [2]

The symbols $\gamma_{sl}$, $\gamma_{lv}$, and $\gamma_{sv}$ represent the surface tensions of solid/liquid, liquid/vapor, and solid vapor, respectively. In order for the solid to be wetted, the free energy of the solid must be lowered when in contact with the liquid so that it becomes covered by the liquid. On the other hand, the solid will not be wetted if the free energy increases as it comes in contact with the liquid.

The typical dip coating process for coatings solids with a liquid is comprised of five stages:

1. Immersion
2. Startup
3. Deposition
4. Drainage
5. Evaporation

In the immersion stage, the solid is inserted at a constant speed into the liquid pool in a steady and controlled manner. During the startup stage, the substrate has soaked in the liquid for some time and is ready for withdrawal. The substrate is removed at a constant speed during the deposition phase, in which a thin coating is applied onto the substrate. This stage is arguably the most crucial stage as the speed and steadiness is correlated to the thickness and quality of the coating. The rate of withdrawal should be adjusted based off the viscosity, surface tension, and gravity of the solution. Finally, during the drainage and evaporation stages, excess liquid is drained from the substrate and any solvents present evaporates from the liquid [44]. The thickness of the film, $h_s$,

generated by withdrawing a solid at constant speed from a pool of a nonevaporating, Newtonian fluid can be described by the Landau-Levich equation in Equation 2.7:

$$h_s = \frac{0.94\eta_s^{2/3}}{\gamma_s^{1/6}(\rho_s g)^{1/2}} u^{2/3} \tag{2.7}$$

where $\eta_s$, $\rho_s$, and $\gamma_s$ are the viscosity, density, and surface tension of the liquid, respectively. The speed of withdrawal and gravity are represented by symbols $u$ and $g$, respectively [45]. While these conditions may facilitate proper adhesion, the liquid may not adhere properly based off the wetting conditions of the materials in question.

### 2.3.1 Induction Heating

The method of heating materials that are electrically conductive, such as metals and semiconductors, is known as electromagnetic induction – i.e., induction. This process consists of electrical currents that are internally induced (eddy currents) into the material to be heated, referred to as the workpiece. The eddy currents generate heat on the workpiece by dissipating energy. Induction furnaces have three main components: the AC power supply, an induction coil, and the workpiece. An induction furnace made by RDO Induction is shown in Figure 2.3.


Figure 2.3: An Induction Heater

The coil, which is directly connected to the power supply, can be formed to different shapes and sizes based off the geometry of the workpiece. AC current generated from the power supply creates an alternating magnetic field that intercepts through the workpiece, thus inducing eddy currents. The distance between the coil and the workpiece is related to the magnitude of eddy currents. This allows for different applications that require different levels of heating such as surface heating and heat treatment or heat treated (HT). Due to the effect of heat transfer, nonuniform heat generation, and the geometry and material of the workpiece, mathematical analysis of induction heating can be very complex. There are quantitative solutions for the simplest cases such as round bars or rectangular slabs.

The phenomenon behind electromagnetic induction is analogous to the transformer effect. In a transformer, there are two coils slightly spaced apart. As a voltage is applied to one of the coils (commonly referred to as the "primary"), an AC voltage is induced onto the other coil ("sec-

ondary"). The induction coil in this example is the primary as it is actuated by the power supply, the workpiece is the secondary [46].The parameters that affect the rate of heating are the intensity and frequency of the induced current and the magnetic permeability, specific heat, and electrical resistance of the material. The sole heating mechanism that arises from induction heating is energy losses that occur from Joule heating of the workpiece [47].

## 2.4 Thin Film Deposition

Thin film applications span many categories including optical, electrical, magnetic, chemical, mechanical, and thermal. Some applications for thin film coatings in the mechanical category include tribological coatings, hardness, and adhesion. It is important to address the meaning and difference between thin and thick film coatings. Thin film technology involves the deposition of single molecules, whereas thick film technology is the deposition of particles. It must be noted that some applications of thin film deposition can result in thicker coatings then those deposited by thick film deposition [48]. Thin film deposition techniques are generally classified into three categories: physical vapor deposition (PVD), cathodic sputtering, and chemical deposition [49]. PVD is also considered a broad category as it encompasses many evaporation and sputtering methods to coat materials with thicknesses that vary from angstroms to millimeters. The scope of this work is limited to physical vapor deposition, in which the deposition of thin films is of the vapor phase originating from a solid source. Whether the process is evaporation by electron beam or resistive heating, or by sputtering such as magnetron sputtering, all processes follow the same sequential steps: processing of the source material, transport of the material, and deposition onto the substrate. Deposition processes that use solids and gasses as source materials are termed as PVD and CVD, respectively. The success of the transportation of the source material relies heavily on the uniformity of the supply rate. Many film properties are affected by the deposition rate as well as any contamination present on the material. In high-vacuum deposition systems, the molecules from the source travel to the substrate in straight lines, thus the uniformity of the supply rate is

dependent on the geometry of the source. The quality of deposition is determined by surface factors including energy input, substrate surface condition, and the reactivity of the arriving material [48]. The following sections cover the theory of plasma transport and evaporation associated with magnetron sputtering and electron beam evaporation, respectively.

### 2.4.1 Sputtering

Sputtering is the process of accelerating ionized atoms towards a surface (referred from here on out as the "target") that results in the ejection of atoms from the target. This phenomena is used in sputter deposition and sputter etching, in which the ejected atoms nucleate a thin film on the substrate (the former) or remove unwanted material from the substrate (the latter). In sputter deposition, an incident ion is accelerated onto the target's surface by an accelerating potential in the deposition chamber. This incident ion is usually $Ar^+$ since it is a low-cost, inert gas. Next, as the bombardment atom reaches the targets surface, atoms "sputter" off the surface and condenses onto the substrate to form a thin film. The potential drop between the target's surface and the ionized plasma gas is the source of the accelerating energy used to bombard the ions. This potential drop is known as "The Cathode Fall". The sputter yield, $Y$, a key metric in characterizing the sputtering process, is a measure of the number of atoms ejected from the target for each single bombardment ion, or in equation form [50]:

$$Y = \frac{\text{Number of Sputter Atoms Ejected}}{\text{Number of Sputtering Atoms Incident}} \tag{2.8}$$

Sputtering systems can be fitted with many features based off the complexity of the desired film. One advantage sputtering systems have is that multiple targets can be used simultaneously to deposit different materials at the same rate. The sputtering rate for most materials are withing one order of magnitude from lowest to highest [51]. The following contains a list of required and optional components of a typical sputtering deposition system [52]:

- Certified vacuum-tight mild/stainless steel chamber

- Pumping capacity of reaching at least $10^{-6}$ Torr
- Pressure gauges
- Mass flow controllers to raise pressure for sputter operation
- Sputter source(s)
- Power supply
- Substrate holder
- Substrate heater
- Power supply for bias sputtering
- Automation control system

Sputter deposition systems can be powered by DC or RF, with the latter having the capability of sputtering electrically insulated materials. RF plasmas also provide higher plasma densities since they are used with an impedance matcher hardware to tune the output impedance [48, 50]. Magnetic sputter sources, called magnetrons, have a permanent magnetic field of 50-500 Gauss parallel to the targets surface. This confines secondary electrons in the vicinity of the target's surface. This confinement of electrons causes a greater ionization of the gas, resulting in a denser plasma and enhanced deposition rates. This increased efficiency allows for lower operating voltages and pressures.

### 2.4.2 Evaporation

Evaporation is a PVD process, in which the source is thermally heated to a vapor phase by methods such as electron beam bombardment, resistive heating, flash evaporation, exploding wire, or induction heating [49]. Evaporation systems consist mainly of a source to heat the material (evaporation source), a substrate holder that is directly facing the evaporated source, and a vacuum chamber

capable of reaching levels of $10^{-5} - 10^{-8}$ Torr. It is critical to reach these vacuum levels in order to achieve a large mean free path (MFP) in the range of 5 x $10^2$ to $10^5$ cm [52]. The rate of free evaporation of atoms from a unit area in vacuum is determined by the Langmuir equation

$$m_e = 5.83 \text{ x } 10^{-2}\, p_e \sqrt{\frac{M}{T}} \tag{2.9}$$

where $p_e$ is the equilibrium vapor pressure of the material under saturated-vapor conditions at a temperature $T$. $M$ is the molecular weight of the vapor species [49]. In order to understand how the molecules evaporate from the condensed phase to the vapor phase, the molecular potential energy diagram for evaporation and condensation is needed. This is shown in Figure 2.4

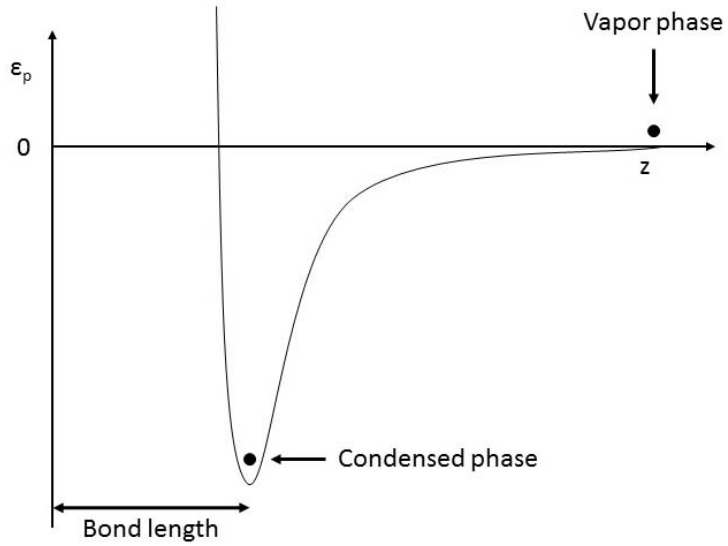


Figure 2.4: Molecular Potential-Energy Diagram for Evaporation and Condensation

At the bottom of the potential well ($z = 0$) exists a molecule that is in the condensed phase. During evaporation, the molecules move to $z = \infty$ by the breaking of bonds resulting in an increased potential energy, $\varepsilon_p$. This process of evaporation involves the change of heat and work and must therefore abide by the first law of thermodynamics, in which energy is conserved. This is expressed as

$$dU + dw = dq \tag{2.10}$$

The change in heat ($dq$) must result from either stored internal energy ($dU$) or from work output ($dw$) [48].

The method of thermal evaporation assisted by electron beam bombardment is a common method, in which the source is heated by an accelerating electron beam. In an electron beam evaporator, electrons are thermoionically emitted from a filament through an acceleration voltage. In most cases, an emission of 1 A is accelerated through a potential of 10 kV, resulting in 10 kW delivered to the source. The magnetic field then pulls the electron beam away from the filament and towards the source material. The total force on the electron in magnetic and electric fields is the Lorentz force and is

$$F = F_E + F_B = q_e E + q_e v \times B \tag{2.11}$$

where $F_B$ is the magnetic force obtained by the cross product of the electron velocity, $v$, and the magnetic field, $B$. $F_E$, $F$, $E$, and $q_e$ are the force on the electron, total force, electric field and charge, respectively. The magnetic force follows the right-hand rule, in this case the magnetic field is pointing out of the page and $v$ is pointing away from the electron as the charge, $q_e$ is negative [48]. This is pictured in Figure 2.5. The force that accelerates the electrons away from the filament is derived from the kinetic energy of the electron that travels through the electric field.

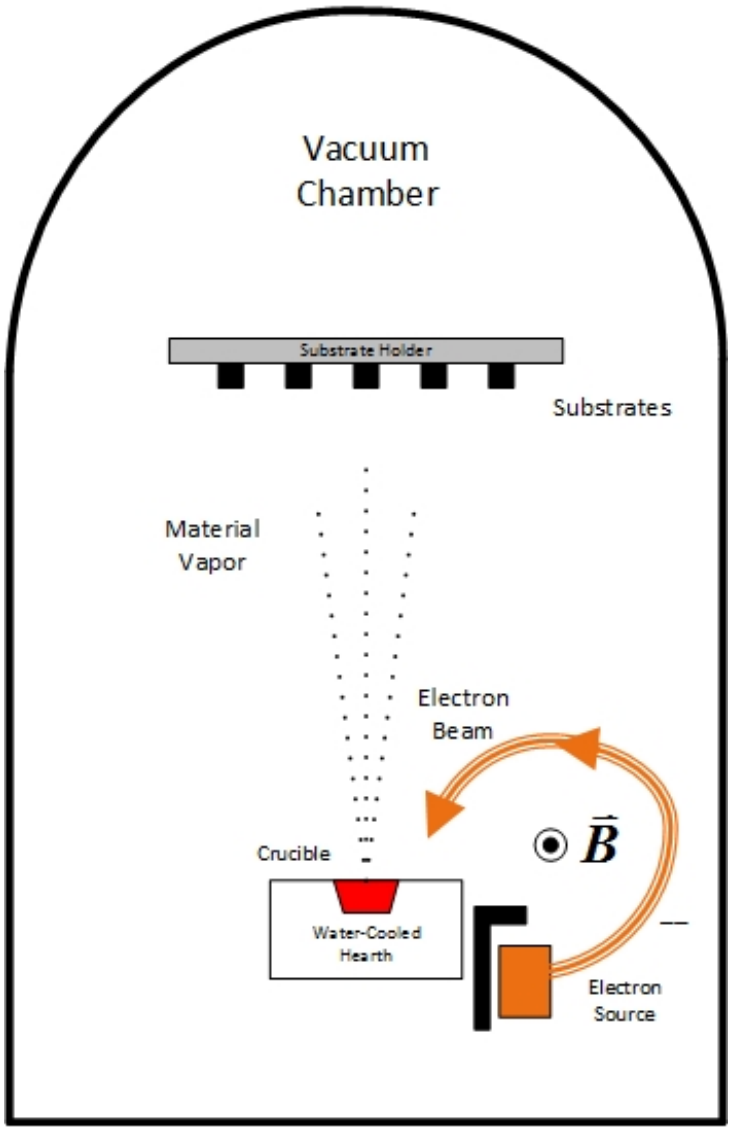


Figure 2.5: Schematic of an Electron Beam Thermal Evaporator

# Chapter 3

# Experimental Methods

## 3.1 Overview

This research investigates several methods of joining SiC to FeCrAl and SiC to aluminum as well as coating SiC in an effort to determine whether a hermetically sealed ATF clad for LWRs comprised of these materials is feasible. A hermetically sealed fuel clad would be impenetrable to gasses or liquids, which is critical for retaining fission products trapped in the fuel cladding. This work has been split up into three phases. In Phase I, outlined in Section 3.2, diffusion bonding of SiC to FeCrAl and SiC to aluminum using thin metallic inserts of FeCrAl and aluminum, respectively, was investigated. The purpose of this phase is to investigate if diffusion bonding can serve as a joining technology for SiC tubes. Here, the various combinations of temperature, hold time, and ramp rate were explored. Dip coating and casting of aluminum and FeCrAl onto SiC by induction heating was examined in Phase II, explained in Section 3.3. Dip coating and casting proves an economical solution of hermetically sealing SiC on a mass-production scale. Thin-film coatings deposited onto SiC by methods of magnetron sputtering and electron beam evaporation consisted of the first part of Phase III and is outlined in Section 3.4. In the second part of Phase III, the coated SiC specimens were then subjected to high-temperature diffusion bonding, as explained in Section 3.5. Optical microscopy, SEM, and EDS were used to qualitatively characterize the

experiments. The purpose of the coatings is twofold: first it provides hermetic sealing by saturating the porous SiC by thin films of dense alloys, second, it introduces compositional graded interlayers to reduce the CTE mismatch between SiC and FeCrAl in an effort to join the materials. Both SiC and FeCrAl have attractive properties for LWR applications such as high melting temperatures, high strength, high-temperature oxidation resistance, low thermal neutron absorption, and minimal hydrogen generation.

## 3.2 Phase I: Diffusion Studies

### 3.2.1 Motivation

Diffusion bonding is a proven method to bond ceramics with metallic alloys. In particular, SiC has been bonded to materials including titanium, molybdenum, and chromium by diffusion bonding techniques [27, 28, 29]. By optimizing the parameters: temperature, hold time, and applied pressure, a joint will be formed between the two materials.

### 3.2.2 Sample Preparation

For all experiments, the type of SiC used was Hexoloy SE SiC, a sintered SiC obtained from Saint-Gobain Ceramics. Properties of this type of SiC can be viewed in Table 1.1. The SiC is in the form of rods measuring six inches in length by 0.28 inches in diameter, shown in Figure 3.1.


Figure 3.1: Hexoloy SE SiC

In order to prepare flat, smooth specimens for diffusion bonding as recommended in Section 2.2, a comprehensive sample preparation procedure was performed. The first step was to section the SiC rods into discs with specified thickness. This was accomplished using a SYJ-160 low-speed diamond saw from MTI XL as shown in Figure 3.2.

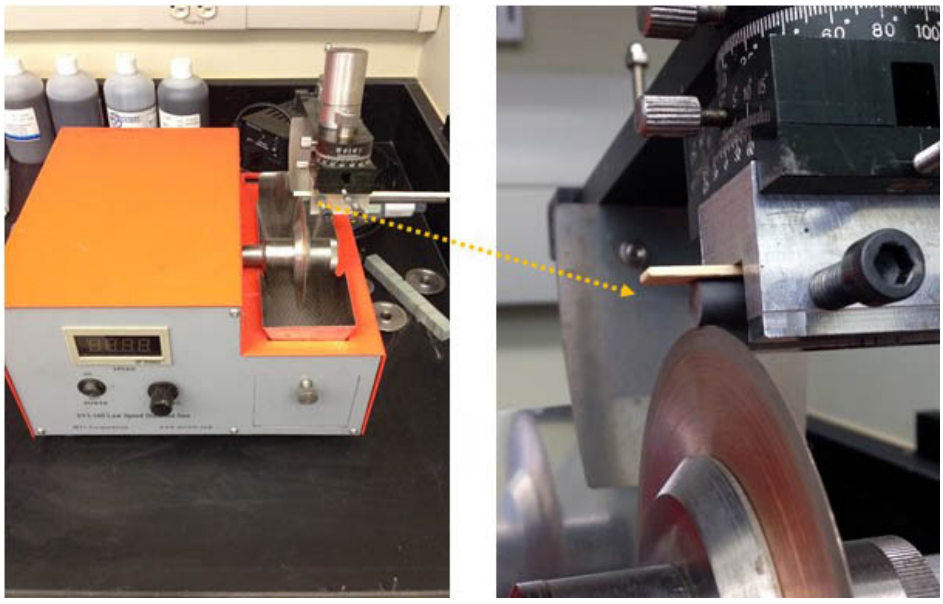

Figure 3.2: Sectioning SiC Using a Low-Speed Diamond Saw

The most crucial step in the sample preparation process was to obtain a flat and smooth surface.

This was done by grinding the sectioned specimens using flexible diamond grinding discs of 220, 600, and 1200 grit. To further polish the grinded specimens, lapping was performed using polycrystalline diamond suspension up to 0.25 $\mu m$. The final step consisted of cleaning the polished specimens by sonicating them in acetone for five minutes. At this point, the specimens were stored in a vial filled with acetone until it was ready to be used. This sample preparation procedure is used for all experiments in Phase I - Phase IV.

### 3.2.3 Methods

The preliminary diffusion bonding experiments consisted of sandwiching an interlayer (aluminum and/or FeCrAl) material between two pieces of SiC measuring 2-3 mm in thickness. A pressure capsule, shown in Figure 3.3 was used to compress the materials in the composite. Varying amounts of washers were used to control the pressure onto the samples. Lock washers were utilized to ensure that the screws do not back off during high temperatures. Stainless steel plates are used between the screw heads and the outer material to prevent any piercing or cracking to the material. The aluminum obtained from Sigma-Aldrich, is in the form of 0.25 mm thick foil with a purity of 99.999%. The FeCrAl tape was obtained by our partners at ORNL. The elemental composition for the FeCrAl tape is 14.980% Cr, 5.020% Al, 0.033% Y (Rest Fe).

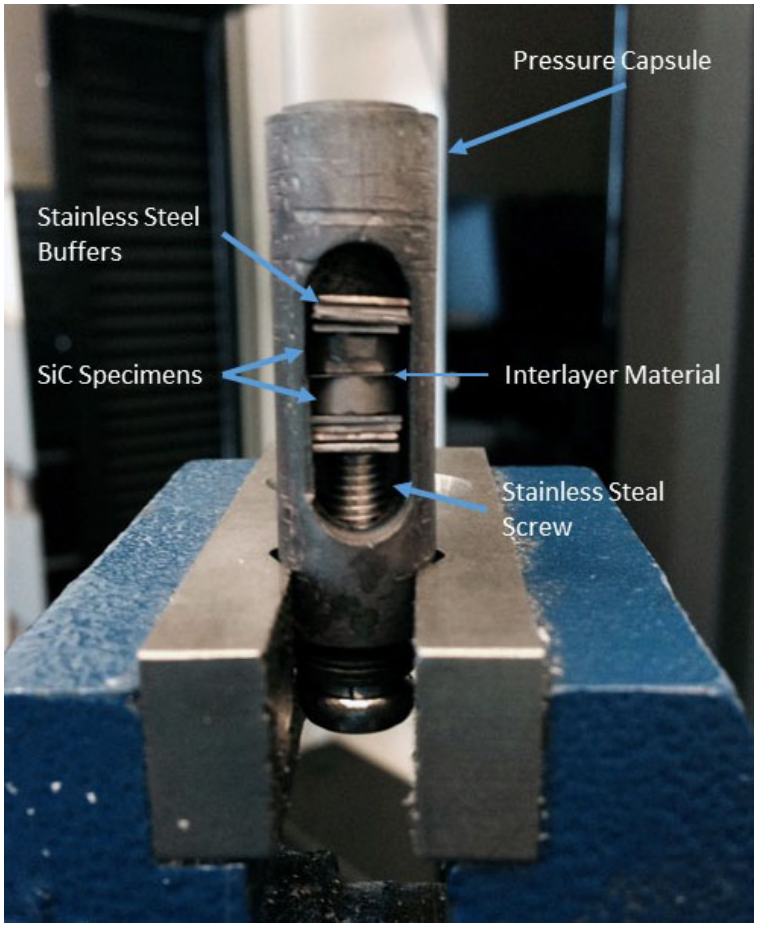


Figure 3.3: Pressure Capsule Jig for Compressing Samples

The experimental parameters in Table 3.1 indicate the materials used in the experiment, hold temperature, hold time, and ramp rate. Aluminum and FeCrAl were used as interlayers in these experiments. The melting temperatures of aluminum and FeCrAl are 660 and 1700°C, respectively.

### 3.2.4 Post Processing

To characterize the diffusion bonding experiments, it is necessary to visualize the diffusion layers or intermetallics that may or may not have formed during HT. This is done by analyzing the cross section of the specimen, which needs to be polished to a very small particle size. Characterization by SEM and EDS will require additional processing steps. The first step is to obtain a cross section of the specimen by using a low-speed diamond saw. This procedure is similar as in sample preparation, however the speed of the blade is critical to the integrity of the composite. Typically, a

Table 3.1: Operating Parameters for Diffusion Bonding Experiments

| Experiment | Sample Configuration | Furnace Temp (°C) | Hold Time (Hr) | Ramp Rate (°C/min) |
|---|---|---|---|---|
| 1 | SiC-Al-FeCrAl-SiC | 900 | 5 | 10 |
| 2 | SiC-Al-SiC | 400 | 6 | 1.82 |
| 3 | SiC-Al-SiC | 450 | 6 | 2.05 |
| 4 | SiC-FeCrAl-SiC | 1000 | 6 | 4.17 |
| 5 | SiC-Al-FeCrAl-Al-SiC | 500 | 6 | 2 |
| 6 | SiC-Al-FeCrAl-Al-SiC | 550 | 6 | 2 |
| 7 | SiC-Al-FeCrAl-Al-SiC | 600 | 6 | 2 |
| 8 | SiC-Al-FeCrAl-Al-SiC | 650 | 6 | 2 |
| 9 | SiC-Al-FeCrAl-SiC | 650 | 6 | 2 |
| 10 | SiC-Al-FeCrAl-SiC | 650 | 6 | 2 |
| 11 | SiC-Al-FeCrAl-SiC | 650 | 6 | 2 |
| 12 | SiC-Al-FeCrAl-Al-SiC | 600 | 10 | 2 |
| 13 | SiC-Al-FeCrAl-Al-SiC | 600 | 10 | 2 |
| 14 | SiC-Al-FeCrAl-Al-SiC | 550 | 10 | 2 |
| 15 | SiC-Al-FeCrAl-Al-SiC | 550 | 10 | 2 |

lower speed will reduce the shear stress during cutting. After the specimen is cut, it is ultrasonically cleaned in water for 15 minutes.

The next step is to polish the cross section of the specimen, while the specimen is mounted in a resin to firmly secure it during polishing. This is achieved by using either a glass-filled curing acrylic or a fast-curing hard epoxy. This procedure, referred to as mounting, involves placing the cross section of the specimen in a specimen mold where the resin will be poured into. As the resin cures, the bottom of the cap can be removed revealing a flat surface with the cross section exposed. The specimen is now ready to be polished. The general rule-of-thumb is to start with an abrasive sandpaper and progressively increase the grit number (or decrease the particle size). SiC sandpaper varying from 600-1200 grit is used to polish the composites despite the fact that these composites contain SiC (see Section 5 for clarification). Each step is performed for approximately 10 minutes or until a uniform surface is obtained. Finer polishing achieved by lapping is performed using

polycrystalline diamond suspension in stages from 6 $\mu m$ to 0.25 $\mu m$ particle size. The polished specimen is then cleaned with isopropyl alcohol and ultrasonically cleaned in water. For SEM and EDS characterization, the specimens must be electrically conductive from the specimen itself to the bottom of the resin where it is in contact with the SEM sample holder. This is achieved by depositing a thin layer of carbon on the top of the specimen by Joule heating sputtering. Copper tape bridges the top and bottom of the sample, making the entire specimen electrically conductive. This post processing procedure is used in Phases I-IV.

### 3.2.5 Results and Discussion

The experiments that were performed in Section 3.2 indicated that FeCrAl would not bond to SiC directly. Upon removing the sample composite from the tube furnace and then from the pressure capsule, the composite fell apart—i.e., the SiC and FeCrAl were not attached. As this was expected due to the mismatch in CTE as well as microstructural differences, aluminum was used as an interlayer to assist in bonding. The backscatter electron (BSE) SEM images in Figure 3.4 and Figure 3.5 are polished cross sections of samples 7 and 8 and show that FeCrAl bonds to aluminum at bonding temperatures of 600 and 650 °C, respectively.[1] It was concluded that at 600 °C, an intermetallic layer formed between FeCrAl and aluminum. While there was still bonding, the presence of an intermetallic layer is not desired since they are typically brittle and compromise the integrity of the bond. At 650°C, there is no visible intermetallic layer in the composite. In addition, the aluminum layer is smaller in thickness compared to at 600 °C. This was partially attributed to partial melting of the aluminum layer during bonding and slight variances in aluminum thicknesses during polishing. Based off the results from BSE SEM characterization, it was concluded that FeCrAl bonded to aluminum through diffusion bonding.

[1] The optical and SEM images for Phase I samples can be found in Section A

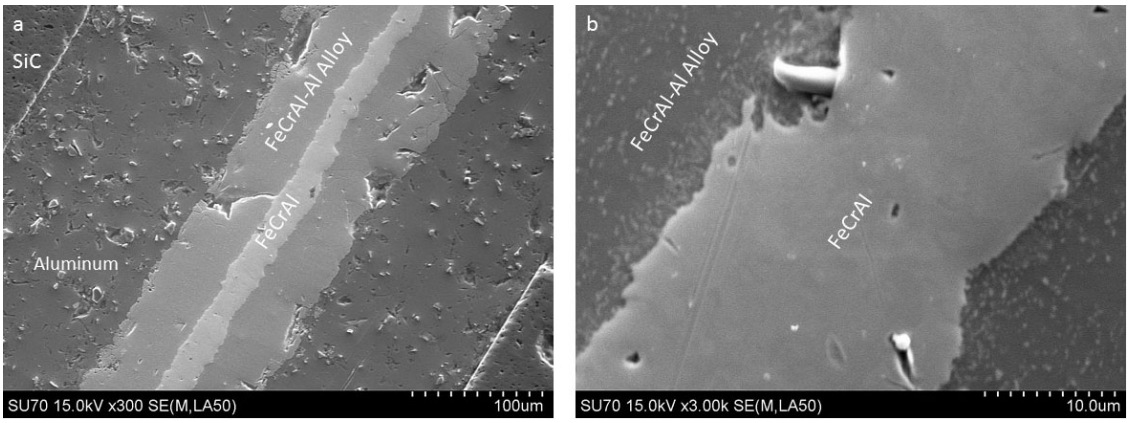


Figure 3.4: BSE SEM Images of (a) Diffusion Bonded Sample 7 and (b) Zoomed Region of FeCrAl-Al Interlayer

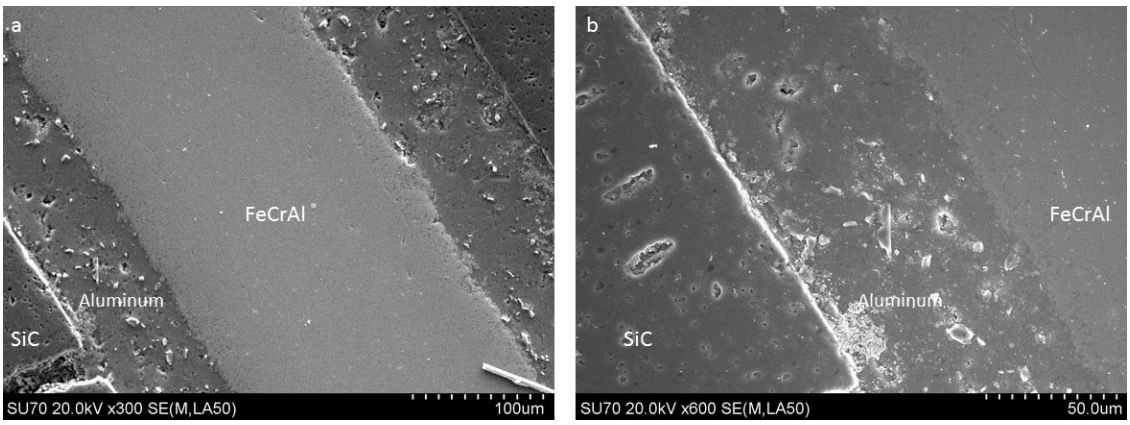


Figure 3.5: BSE SEM Images of (a) Diffusion Bonded Sample 8 and (b) Zoomed Region of FeCrAl-Al Interface

EDS characterization confirms the presence of a FeCrAl interlayer in sample 7. A point spectrum was obtained at the FeCrAl layer as well as the FeCrAl-Al layer. The increase in aluminum content in the interlayer verifies aluminum diffusion into FeCrAl. For reference, a point spectrum was also gathered for the aluminum layer and the SiC-Al interface. This is shown in Figure 3.6.

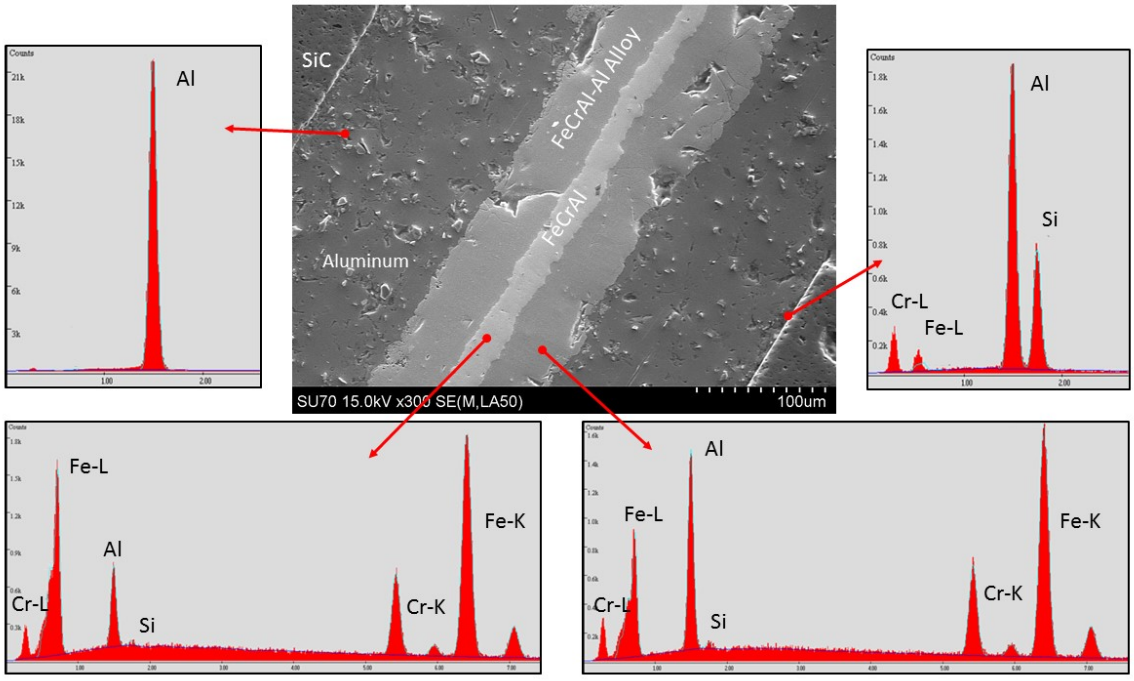


Figure 3.6: EDS Point Spectrum of Different Regions in Diffusion Bonded Sample 7

In addition to this, mapping was performed for sample 7 (see Figure 3.7), which shows the concentration of individual particles of the acquired SEM images. This tool is used to determine whether a certain element has diffused through an interface. In this analysis, mapping was conducted to determine where aluminum and FeCrAl diffused into each other. Lighter regions represent high concentration and darker regions represent lower concentration.

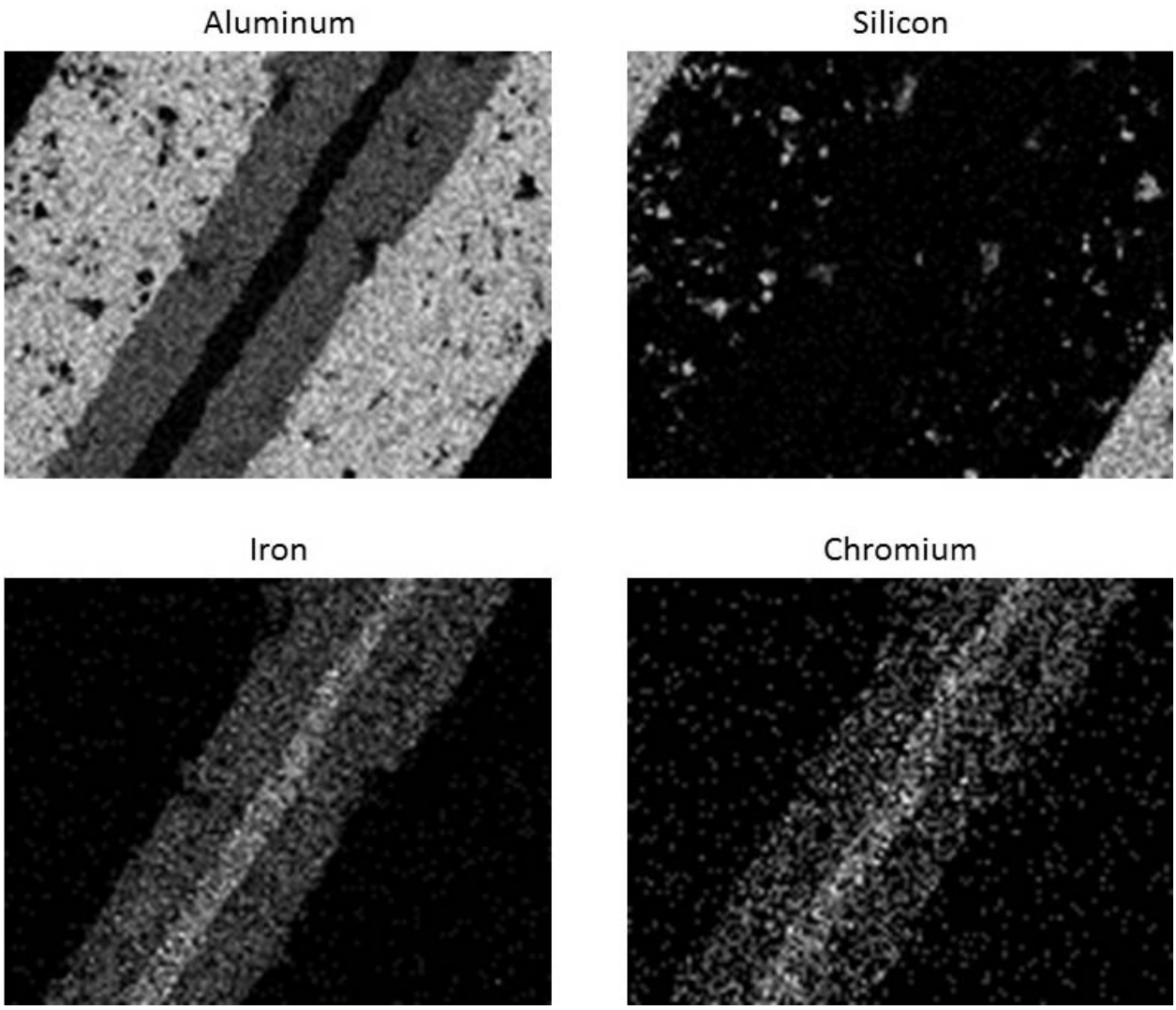


Figure 3.7: EDS Mapping of Different Regions in Diffusion Bonded Sample 7

The mapping shows that the FeCrAl-Al alloy contains more aluminum then the FeCrAl layer itself. Also the aluminum from FeCrAl layer diffused into the FeCrAl-Al layer.

## 3.3 Phase II: Thick Film Coatings

### 3.3.1 Motivation

As the preliminary diffusion bonding experiments were not successful in bonding SiC with FeCrAl or SiC with aluminum, a different method was considered. In thick film coatings, the adhesion of

aluminum and/or FeCrAl to SiC relies on the wetting criteria of the substrate. In theory, based on certain parameters such as temperature and hold time, the contact angle of the molten metal with the substrate will change. If the contact angle is less than 90°, the substrate will be wetted by the molten metal and thus a joint will be formed (See Section 2.3).

### 3.3.2 Methods

#### Aluminum

Two types of experiments were conducted, hot dip coating and casting. The aluminum used for melting was obtained from R.D. Mathis and exhibited a minimum purity of 99.98%. In the dip coating experiments, aluminum was heated in an induction furnace in an ambient atmosphere. As it melted, the SiC rod was submerged into the molten aluminum and removed. The casting experiments were similar with the exception of leaving the SiC rod in the crucible as it cools down and solidifies. The casting experiments were performed in a vacuum chamber back-filled with ultra high purity (UHP) argon gas at 50 Torr. An infrared thermometer was aimed through the viewport of the vacuum chamber to acquire a temperature reading of the crucible. Figure 3.8 shows the vacuum chamber along with a schematic of the vacuum chamber with the thermometer aimed through the rear viewport flange. The copper induction coil, connected via ceramic feedthroughs, sits in the center of the vacuum chamber and is connected to the induction furnace as shown in Figure 3.9. Other ports on the vacuum chamber include: a vacuum port to evacuate the chamber, a flow inlet port to fill the chamber with UHP argon, a purge valve to vent the chamber, and a convection gauge to measure the pressure level.

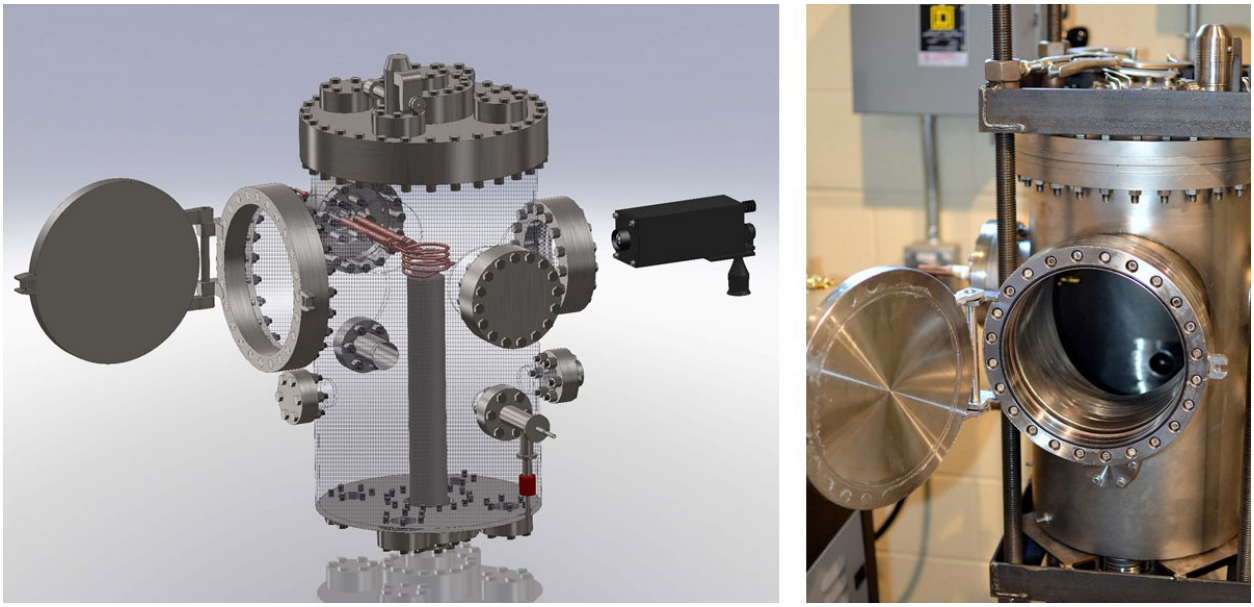

Figure 3.8: Vacuum Chamber

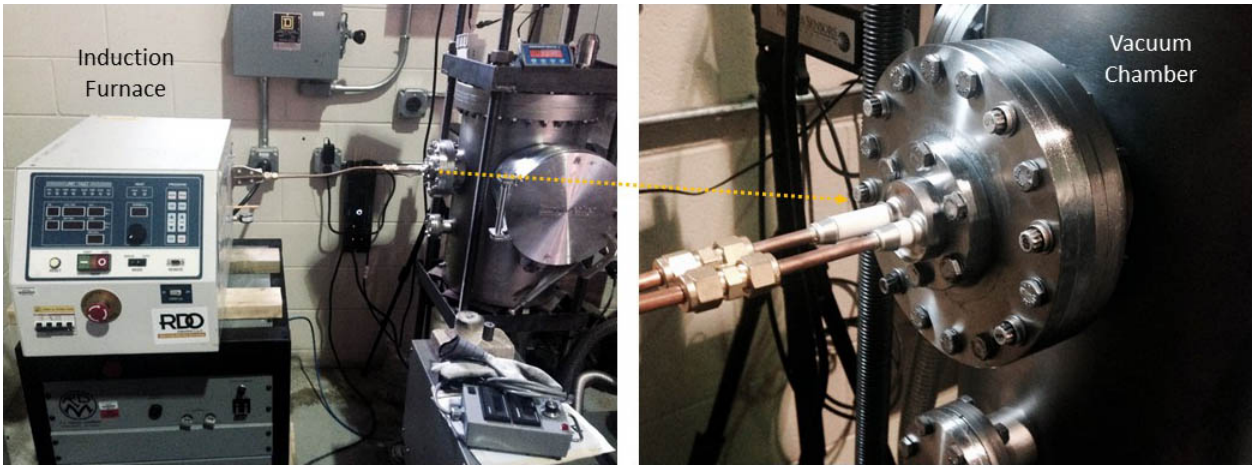


Figure 3.9: Induction Furnace Connected To Vacuum Chamber

The material used to form the crucible was 1215 alloy steel. It was assumed through heat conduction that the temperature of the crucible was similar to the temperature of the molten aluminum. Certain experiments were subjected to HT prior to sectioning. The experimental parameters used for Section 3.3.2 are shown in Table 3.2. The power output of the induction furnace was slowly ramped to 12%; at this point the aluminum became molten. The process of conducting the dip coating experiments is shown in Figure 3.10

Table 3.2: Operating Parameters for Al Dip Coating/Casting Experiments

| Experiment | Type | Temp (°C) | Soak Time at Max Temp (s) | HT Temp (°C) | HT Time (hr) | HT Ramp (°C/min) |
|---|---|---|---|---|---|---|
| 1 | Dip Coating | $T_m$ | 5 | 550 | 8 | 10 |
| 2 | Dip Coating | $T_m$ | 5 | 600 | 8 | 10 |
| 3 | Dip Coating | $T_m$ | 5 | 575 | 8 | 10 |
| 4 | Dip Coating | $T_m$ | 5 | 600 | 6 | 10 |
| 5 | Casting | 700 | 60 | - | - | - |
| 6 | Casting | 800 | 60 | - | - | - |
| 7 | Casting | 900 | 600 | 600 | 6 | 2 |
| 8 | Casting | 1000 | 600 | 600 | 6 | 2 |

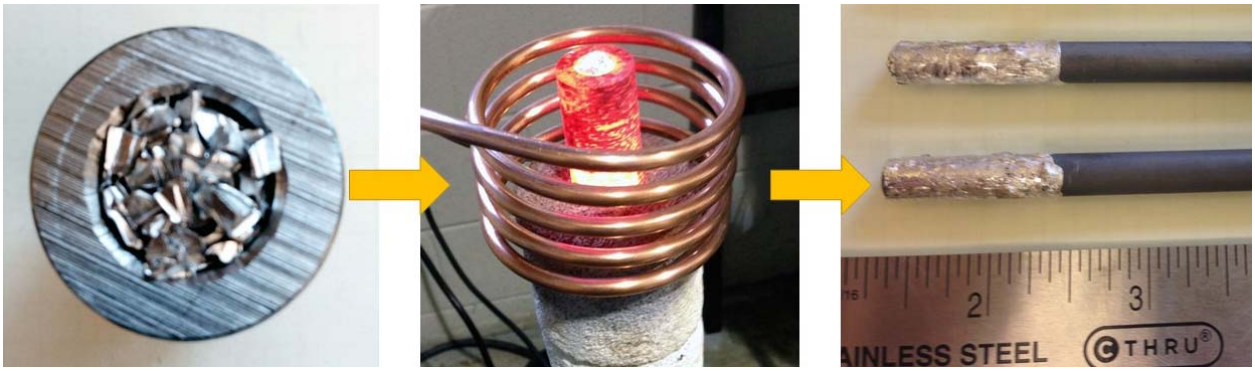


Figure 3.10: Dip Coating SiC in Aluminum

For the casting experiments, the SiC rod was inserted into the crucible prior to heating in such a way that the aluminum pellets would surround the SiC rod. The crucible had a small recess drilled at the bottom to secure the rod from moving as the aluminum melts, as seen in Figure 3.11. The crucible can then be turned down in a lathe, leaving the aluminum-coated SiC rod.

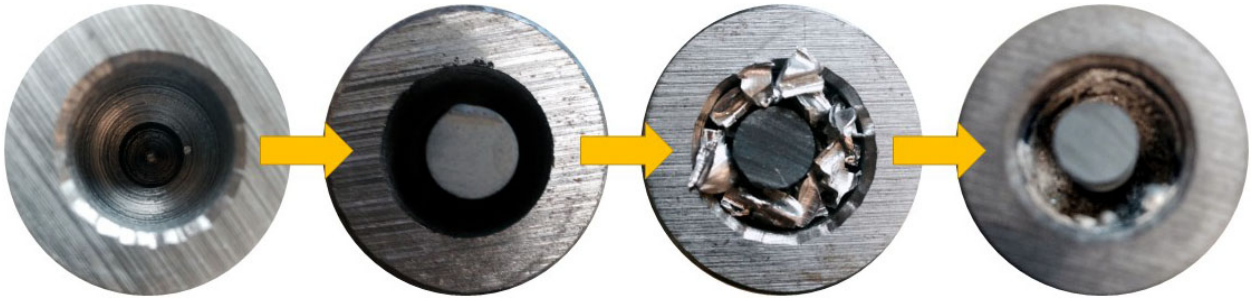

Figure 3.11: Casting Schematic

### FeCrAl

The FeCrAl casting experiments were similar to that of aluminum in terms of the experimental apparatus. The one exception was that a graphite crucible was used, as the melting point of FeCrAl is higher than the steel crucible used in the aluminum casting experiments. The FeCrAl was obtained from ORNL in the form of an ingot measuring 3" in diameter by 0.75" thick. The FeCrAl was machined into pieces measuring 1.5" by 0.75". As these pieces were still too large to fit in a crucible surrounding SiC, the FeCrAl was further machined into tiny slivers using a hand-held dremmel, shown in Figure 3.12. The elemental composition of this FeCrAl varied with the FeCrAl tape used in the diffusion bonding experiments. The elemental composition of the FeCrAl ingot and tape is 15.060% Cr, 3.930% Al, 0.120% Y (Rest Fe) and 14.980% Cr, 5.020% Al, 0.033% Y (Rest Fe), respectively. The FeCrAl ingot has significantly higher yttrium content, which studies have shown leads to reduced high-temperature oxidation in steels [53].


Figure 3.12: Machining FeCrAl

Two experiments were conducted, one under vacuum back-filled with UHP argon at 50 Torr and one under vacuum at 50 mTorr. Both experiments were heated to 1700 °C and held for three minutes.

### 3.3.3 Results and Discussion

#### Aluminum

The optical micrograph for sample 1 is shown in Figure 3.13.[2] It is clear that the aluminum did not bond to SiC. This is partially attributed to multiple factors, such as not having an automated withdrawal mechanism to eliminate any disturbances in the dip coating process, as well oxidation formation in an ambient atmosphere. In samples 2-4, the aluminum flaked off completely. To eliminate these potential negative causes, casting was pursued in an inert atmosphere.

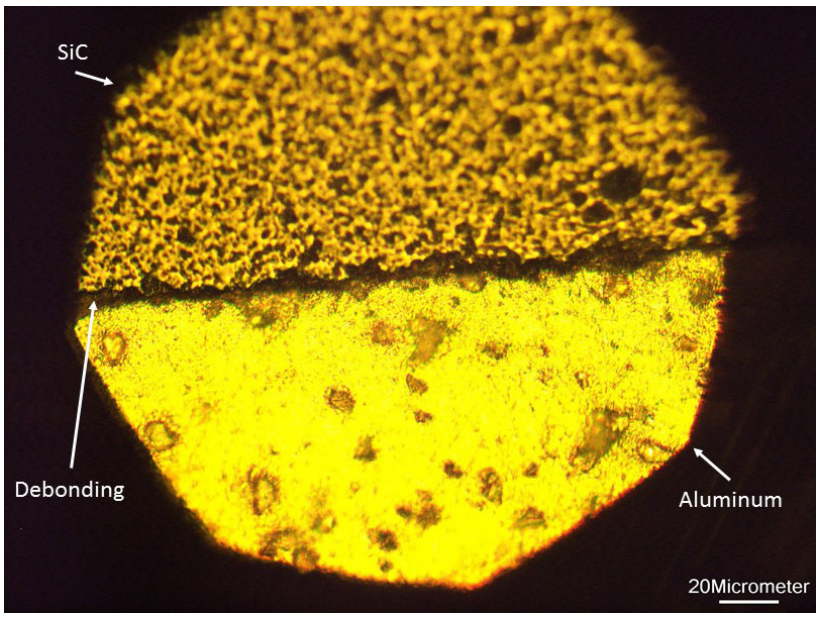


Figure 3.13: Optical Micrograph of Al-Dip Coated Sample 1

The temperatures and soak times for samples 5-8 were chosen based off of studies from [42, 54, 43] that would yield the lowest contact angle in order to achieve proper wetting. The relationship among contact angle, wetting, and adhesion is discussed in Section 2.3. Han *et al.* measured the contact angle of reaction-bonded SiC held in contact with 99.99% aluminum from 0-120 minutes at temperatures of 700, 780, 870, and 960 °C. It was concluded that temperatures of 870 and 960 °C yielded the lowest contact angle. It was also noted that the greatest decrease in contact angle occurred from 0-30 minutes. Another experiment compared the contact angle between SiC and

[2]The optical and SEM images for Phase II samples can be found in Section B

aluminum for reaction-bonded SiC and sintered SiC. The results indicated that sintered SiC had a significantly lower contact angle from 700-1000°C. Köhler reported that at temperatures between 900-1000°C, contact angle decreased. As mentioned in Section 3.2.2, the SiC used was a sintered type. The casted experiments were conducted at temperatures between 700-1000°C at various hold times. The SEM images for sample 5 is shown in Figure 3.14

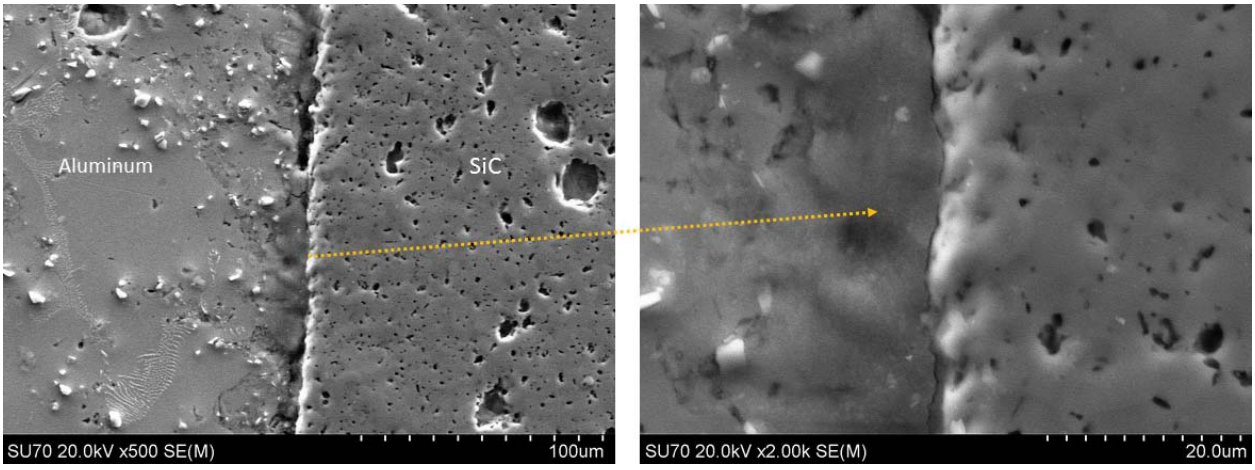


Figure 3.14: SEM Image of Al-Casted Sample 5

The SEM image for sample 5 shows that aluminum appeared to have bonded with SiC. To confirm whether the two materials adhered to one another, EDS mapping was performed for this specimen, shown in Figure 3.15

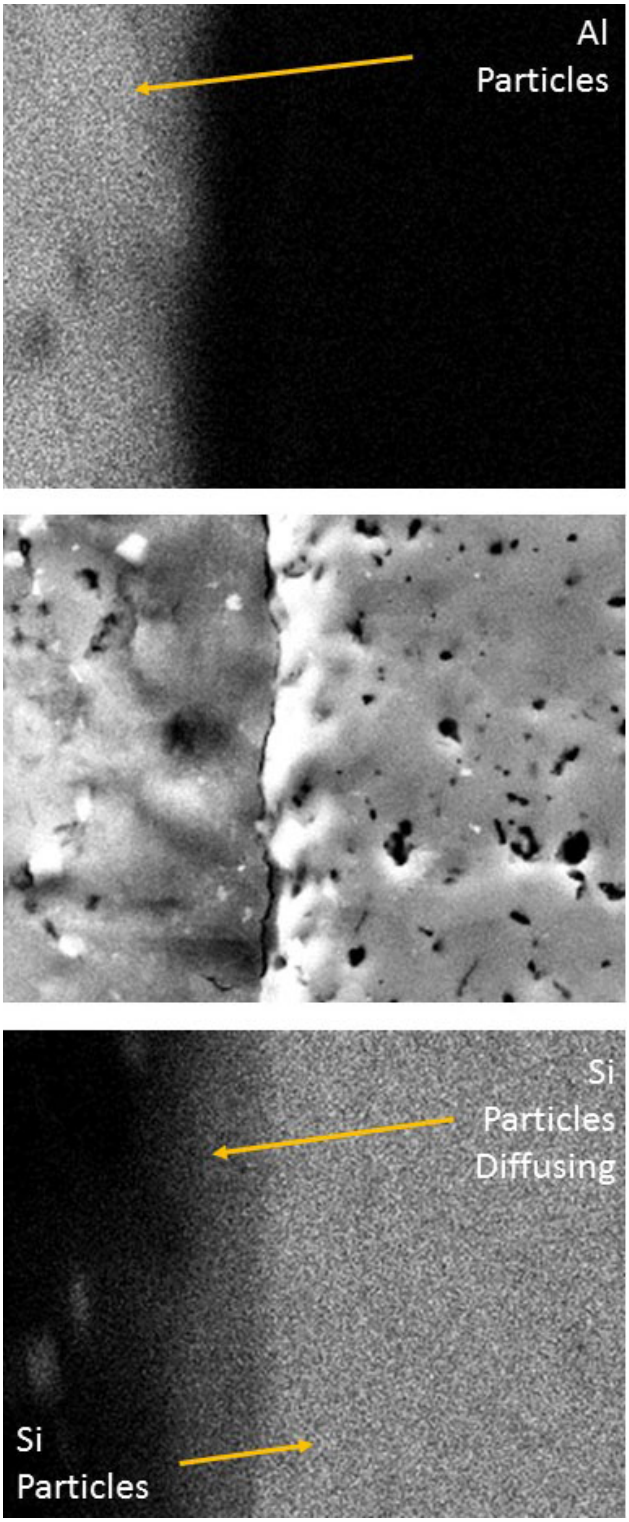


Figure 3.15: EDS Mapping of Al-Casted Sample 5

The mapping shows that silicon particles diffused through the Al-SiC interface, which justified

bonding. However, this procedure for bonding SiC to Al is not recommended as most of the experiments were not successful. In sample 8, in an attempt to bond SiC to Al, it was discovered that iron (from the crucible) adhered to SiC rather than the aluminum. It was later realized that the cross section used was towards the bottom of the sample where the SiC rod was in contact with the crucible in the recess to hold the SiC rod (see Figure 3.11). While EDS mapping confirmed that no diffusion occurred through the interface, the SEM image in Figure 3.16 shows different layers of iron as it comes in contact with SiC.

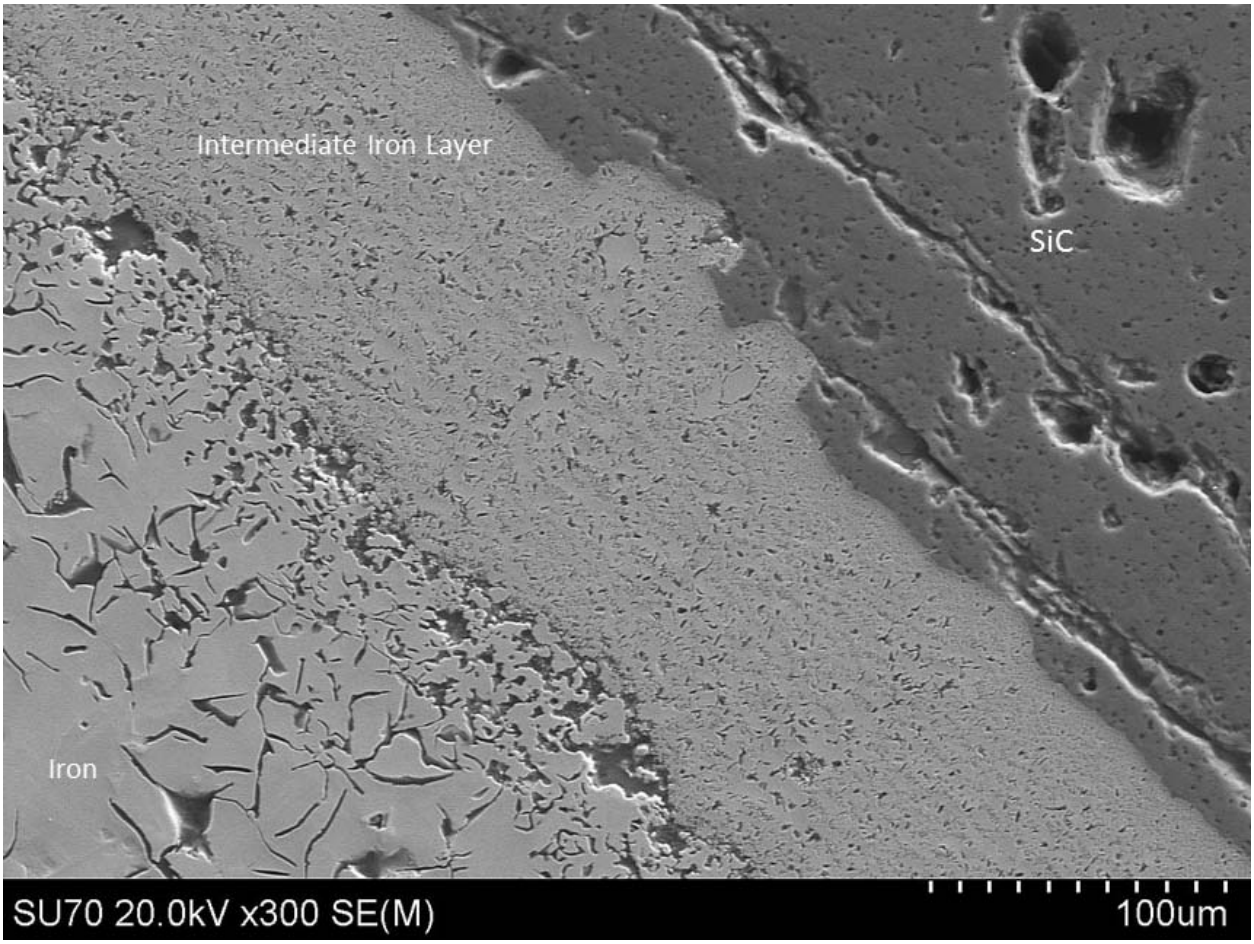


Figure 3.16: SEM image of Al-Casted Sample 8

**FeCrAl**

Upon visual inspection of the specimen cross section, the SiC appeared to have been consumed by FeCrAl. The diameter of the SiC rod decreased almost half its original diameter. The comparison

of SiC casted in aluminum and FeCrAl is shown in Figure 3.17.

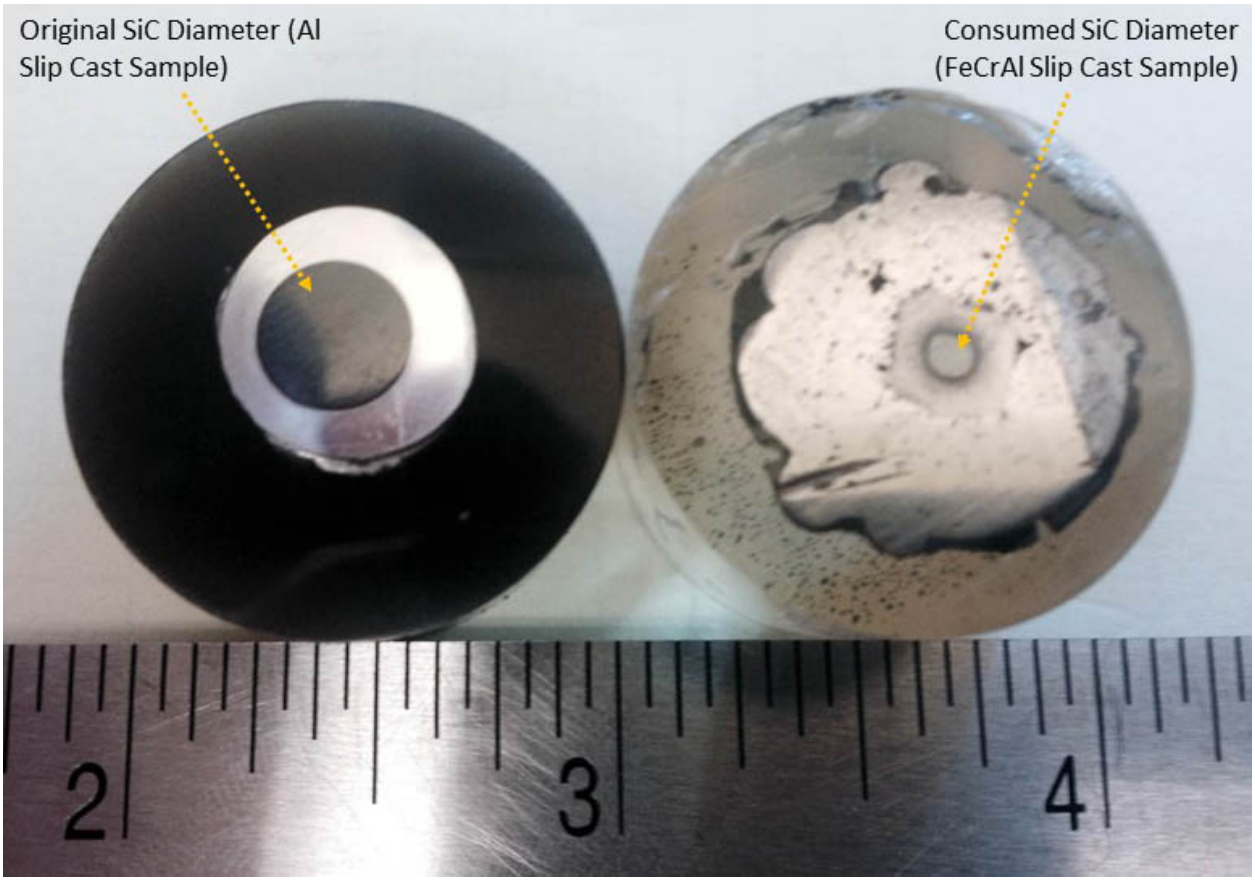


Figure 3.17: Polished Cross Sections of Al-SiC and FeCrAl-SiC Casted Samples

A SEM image of one of the samples is shown in Figure 3.18. The iron region shows areas of broken pieces; in other words, it lacks a homogeneous, continuous layer. This is attributed to the polishing procedure of the cross section mounted in epoxy. This has been a concern for polishing specimens of highly dissimilar materials and is addressed in Section 5. Still, the issue of SiC being infiltrated by FeCrAl is a problem and prevents this as being a viable method of hermetically sealing SiC.

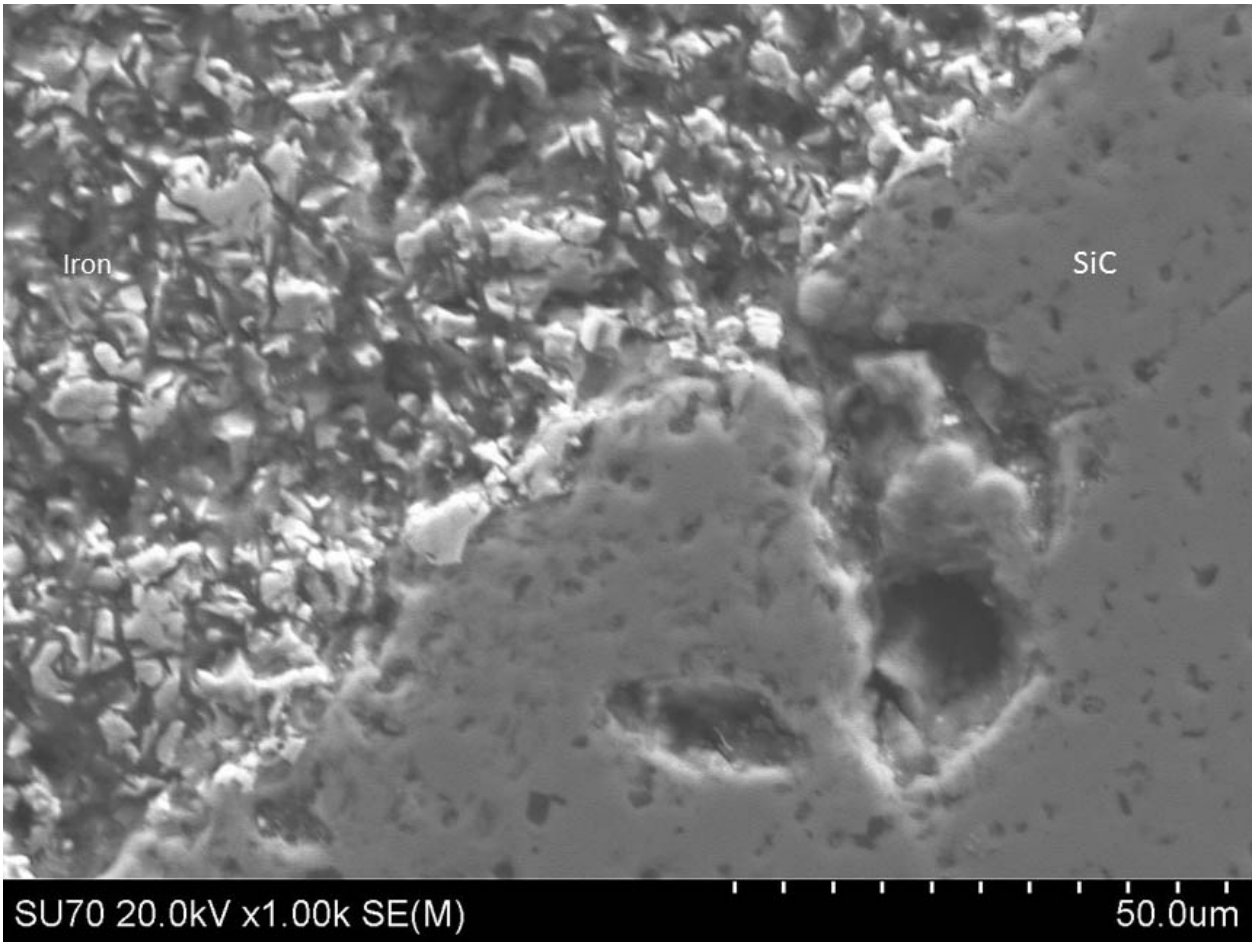


Figure 3.18: SEM Image of FeCrAl-Casted Sample 4

## 3.4 Phase III-I: Thin Film Coating Techniques

### 3.4.1 Motivation

Based on the results of the thick film coating experiments, a different method of bonding SiC to FeCrAl was recommended. While there were some success in bonding aluminum to SiC, consistent, repeatable results were not obtained. Going back to the diffusion bonding experiments, the obstacle that hindered the joining of two largely dissimilar materials is the significant CTE mismatch between SiC and FeCrAl. Solving this issue requires achieving compositionally graded interfaces between the two dissimilar materials assisted by thin film deposition. Thin coatings of iron, chromium, and aluminum from PVD processes of magnetron sputtering and electron beam

evaporation will create compositionally graded interfaces in an effort to join these materials by high-temperature diffusion bonding. In addition to joining SiC, thin film coatings can also be used to hermetically seal SiC. Since SiC is highly porous, thin coatings of metallic, dense materials can provide a hermetic seal to prevent fission products of diffusing through SiC.

### 3.4.2 Methods

The SiC specimens used for magnetron sputtering and electron beam evaporation are prepared in the same manner as that in Section 3.2.2.

#### Magnetron Sputtering

The experimental apparatus used for magnetron sputtering was a fully automated RF magnetron sputtering system available at the Wright Virginia Microelectronics Center. This system is capable of achieving ultra-high vacuum ($\sim 10^{-8}$ Torr) and uses research grade argon that exhibits a purity of 99.9997%. A picture of the magnetron sputtering system is shown in Figure 3.19

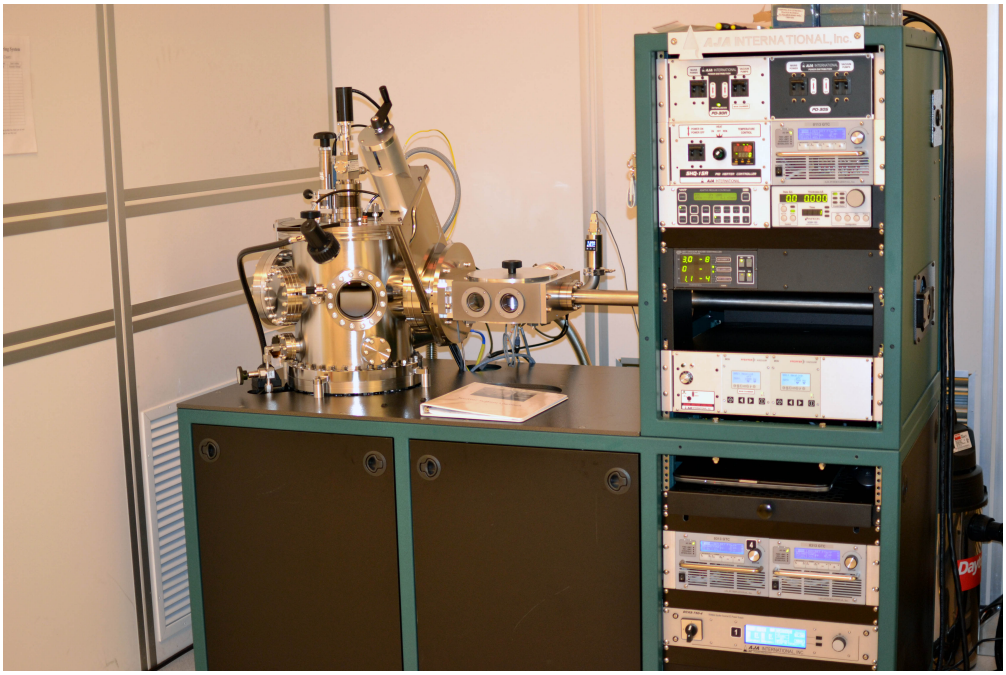

Figure 3.19: Magnetron Sputtering System at the Wright Virginia Microelectronics Center

Magnetron sputtering was used to deposit aluminum onto SiC substrates. The aluminum target was a 2" disc that measured $0.125''$ thick. The operating parameters for the experiments are shown in Table 3.3

Table 3.3: Operating Parameters for Magnetron Sputtering

| Experiment | Operating Pressure (mTorr) | Power (Watts) | Sputter Time (Hr) | Additional Coatings (#, Hr) | Total Coat Time (Hr) | HT |
|---|---|---|---|---|---|---|
| 1 | 1 | 200 | 2 | - | 2 | No |
| 2 | 1 | 200 | 2 | (1, 2) | 4 | Yes |
| 3 | 1 | 200 | 4 | (2, 4) | 12 | Yes |
| 4 | 1 | 200 | 4 | (2, 4) | 12 | Yes |

### Electron Beam Evaporation

An electron beam evaporator was used to deposit thin films of aluminum, iron, and chromium with varying amounts. The apparatus used was an automated system equipped with a deposition controller and a quartz crystal to measure the thickness of the film deposited. This machine was capable of reaching vacuum levels up to $\sim 10^{-6}$ Torr, which was sufficient in achieving an acceptable MFP. This equipment was also available at the Virginia Wright Microelectronics Center and is shown in Figure 3.20.

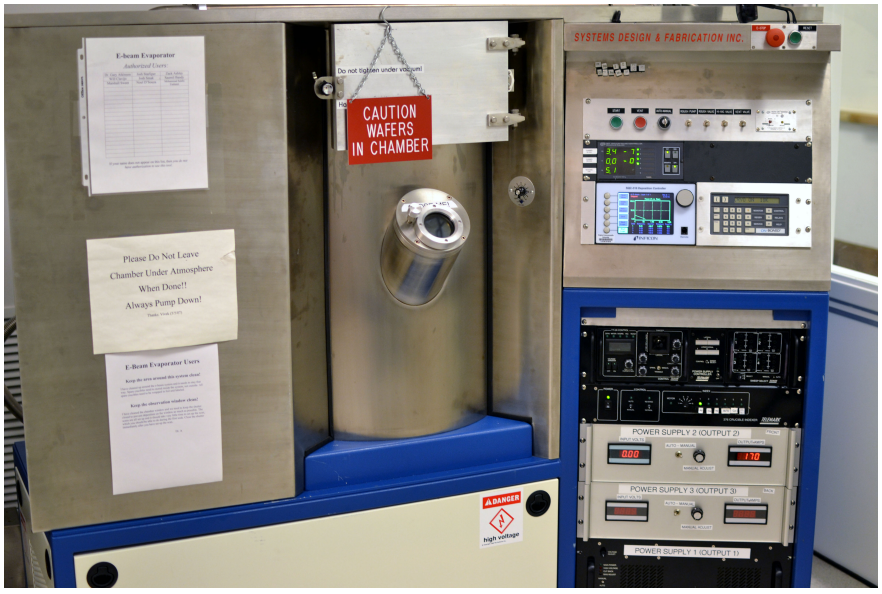


Figure 3.20: Electron Beam Evaporator at the Wright Virginia Microelectronics Center

The deposition controller can be used to vary parameters relevant to the material and film properties. Some of the parameters that can be adjusted include:

- Material density
- Material Z factor
- Deposition rate
- Final deposition thickness
- Feedback parameters (PID)
- Max/Min power limits
- Ramp/Soak conditions
- Shutter Delay

In addition to adjusting the deposition settings, the electron beam sweep can be adjusted to precisely aim the beam at the crucible, as well as the frequency and amplitude. The system is fitted with a crucible indexer, which allows the user to deposit another material without having to vent the chamber and risk any oxidation between coatings. The substrate holder is fixed to a rotating platform that ensures samples are all coated evenly, and this is shown in Figure 3.21.


Figure 3.21: Inside the Electron Beam Evaporator

The coatings were deposited at a low deposition rate to ensure a consistent coating by keeping the supplied power low. The deposition rate used for iron, chromium, and aluminum were 1, 2.5, and 3 Å/s, respectively. Many problems occurred from depositing iron, mainly macroparticle-spitting. This problem happens when a narrow, intense beam evaporates a nodule of a present contaminant whose vapor pressure is higher than the material being evaporated. This pressure burst causes small particles to spit from the material towards the substrate, which is highly undesired. This spitting problem has been associated with source materials that have gas trapped within the material, which is usually the case for sintered materials rather than melted materials. Using high purity source materials, this problem can be minimized [48]. The source material for iron and aluminum is in the form of pellets measuring $0.25'' \times 0.25'' \times 0.5''$. The chromium was in the form of irregular pieces that varied in size. All materials were acquired from R. D. Mathis and exhibited a purity of 99.95% or higher. As shown in Table 3.4, different combinations of the materials were deposited for characterization. In samples 10 and 11, the amount of material deposited for iron, chromium, and aluminum was calculated based off the elemental composition of the FeCrAl tape that will be used to join these coated specimens. The three coating applications of iron, chromium, and aluminum in samples 10 and 11 were intended to be repeated three more times, which would

result in a total film thickness of 1 $\mu m$; however, many problems occurred while depositing iron, which resulted in costly damages to the crystal and crucible.

Table 3.4: Operating Parameters for Electron Beam Evaporation

| Experiment | Material Used | Thickness* (nm) | Total Number of Coatings (#) | Final Thickness* (nm) | HT |
|---|---|---|---|---|---|
| 1 | Fe | 400 | 1 | 400 | Yes |
| 2 | Cr | 400 | 1 | 400 | Yes |
| 3 | Cr | 400 | 1 | 400 | No |
| 4 | Cr/Fe/Cr/Al/Cr | 133/400/133/400/133 | 5 | 1200 | Yes |
| 5 | Cr/Fe/Cr/Al/Cr | 133/400/133/400/133 | 5 | 1200 | No |
| 6 | Cr/Fe/Cr | 200/400/200 | 3 | 800 | Yes |
| 7 | Cr/Fe/Cr | 200/400/200 | 3 | 800 | No |
| 8 | Cr/Al/Cr | 200/400/200 | 3 | 800 | Yes |
| 9 | Cr/Al/Cr | 200/400/200 | 3 | 800 | No |
| 10 | Cr/Fe/Al | 37.45/200/12.55 | 3 | 250 | Yes |
| 11 | Cr/Fe/Al | 37.45/200/12.55 | 3 | 250 | No |

* Thickness Measured By Quartz Crystal

### 3.4.3 Results and Discussion

dark field (DF) optical images of the polished cross sections for the magnetron sputtered and the electron beam evaporated coatings were obtained from a Nikon Eclipse LV100 optical microscope with focused imaging capabilities.[3] The indirect lighting from DF imaging allows the coating to be more visible.

#### Magnetron Sputtered Coatings

Magnetron sputtering was used to deposit aluminum onto SiC for various times. The coatings from specimens 1 and 2 were very thin to the point where they were not visible from microscopy. Samples 3 and 4 were heat treated two times, one after the first coating and the other after the second coating. HT was performed at 550 °C for 3 hours at a ramp rate of 2 °C/min. A third

[3]The optical and SEM images for Phase III samples can be found in Section C

and final coating was applied before the specimens were cut and polished. The SEM images for samples 3 and 4 are shown in Figure 3.22.

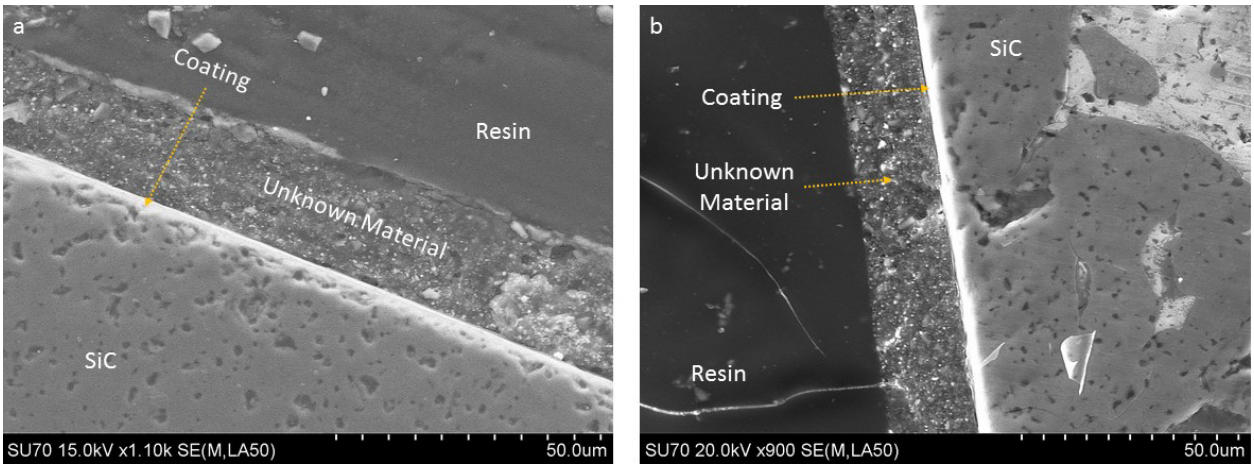


Figure 3.22: BSE SEM Images of (a) Al Sputtered Sample 3 and (b) Al Sputtered Sample 4

The aluminum suffered severe damage during the polishing process. While polishing, the abrasion of SiC particles destroyed the weak aluminum layer, which caused significant tearing to the material. Multiple attempts involving different polishing procedures have been used to reduce this problem; however, there has not been a consistent method in preventing this. This problem is attributed to the large contrast of material hardness of these dissimilar materials and is addressed in Section 5.

**Electron Beam Evaporated Coatings**

A total of 6 different coating experiments by electron beam evaporation were conducted. In each experiment, the SiC specimens were cut in half prior to coating. This was done so that one specimen was available for HT and the other was not for comparison. However, this was not done for iron, as the coating did not adhere well. This resulted in 11 different specimens (6 original and 5 heat treated). The heat treated specimens were heated in an argon containing atmosphere to 450 $^{\circ}$C for 1 hour at 2$^{\circ}$C/min. Despite the inert atmosphere, the heat treated samples exhibited surface oxidation, which may hinder diffusion bonding. As a result, the coated specimens used for high-temperature diffusion bonding in Section 3.5 were ones that were not heat treated. The DF optical

micrograph for samples 2 and 3 are shown in Figure 3.23.

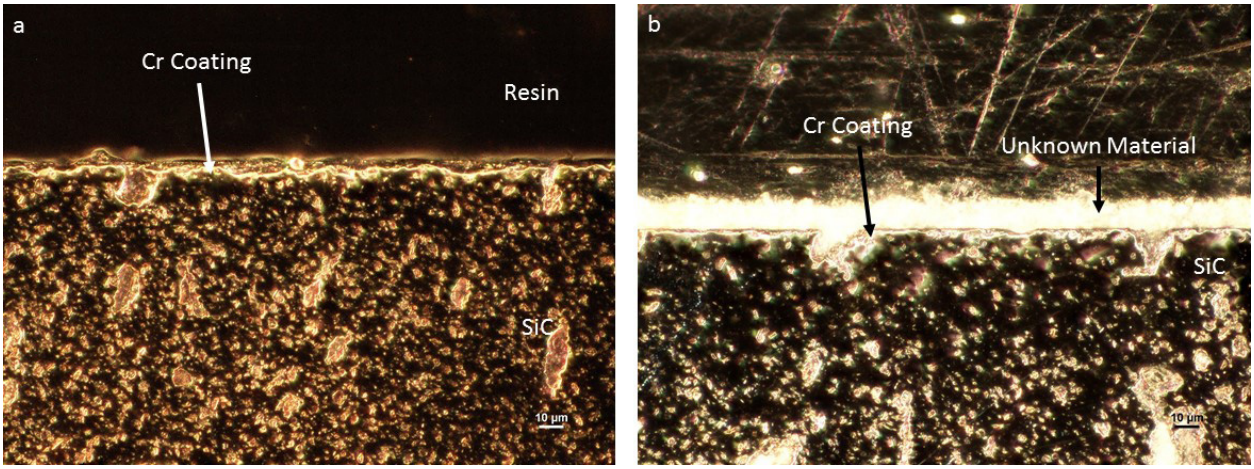


Figure 3.23: DF Optical Micrographs of (a) Cr Evaporated Sample 2 and (b) Cr Evaporated Sample 3

As shown in Figure 3.23, the coating on the heat treated sample has slightly diffused though the SiC, whereas a visible layer remains on top of the SiC on the other sample (not heat treated). It was determined that the sample that was not heat treated would be a better candidate for high-temperature diffusion bonding to FeCrAl since the coating thickness is larger and there is no surface oxidation. Despite having a conductive carbon layer sputtered on the specimen mounts, SEM characterization of the coated specimens was highly problematic due to the resin-coating interface. The acrylic resin used to mount the specimens for SEM would become charged, causing the resin to cover up the coating (see Figure 3.24). This problem occurred at acceleration voltages $\geq 10$ kV at a magnification of $\geq 1,000$x. It was later realized that mounting the specimens in epoxy slightly reduced this problem, which was performed for the specimens in Section 3.5.

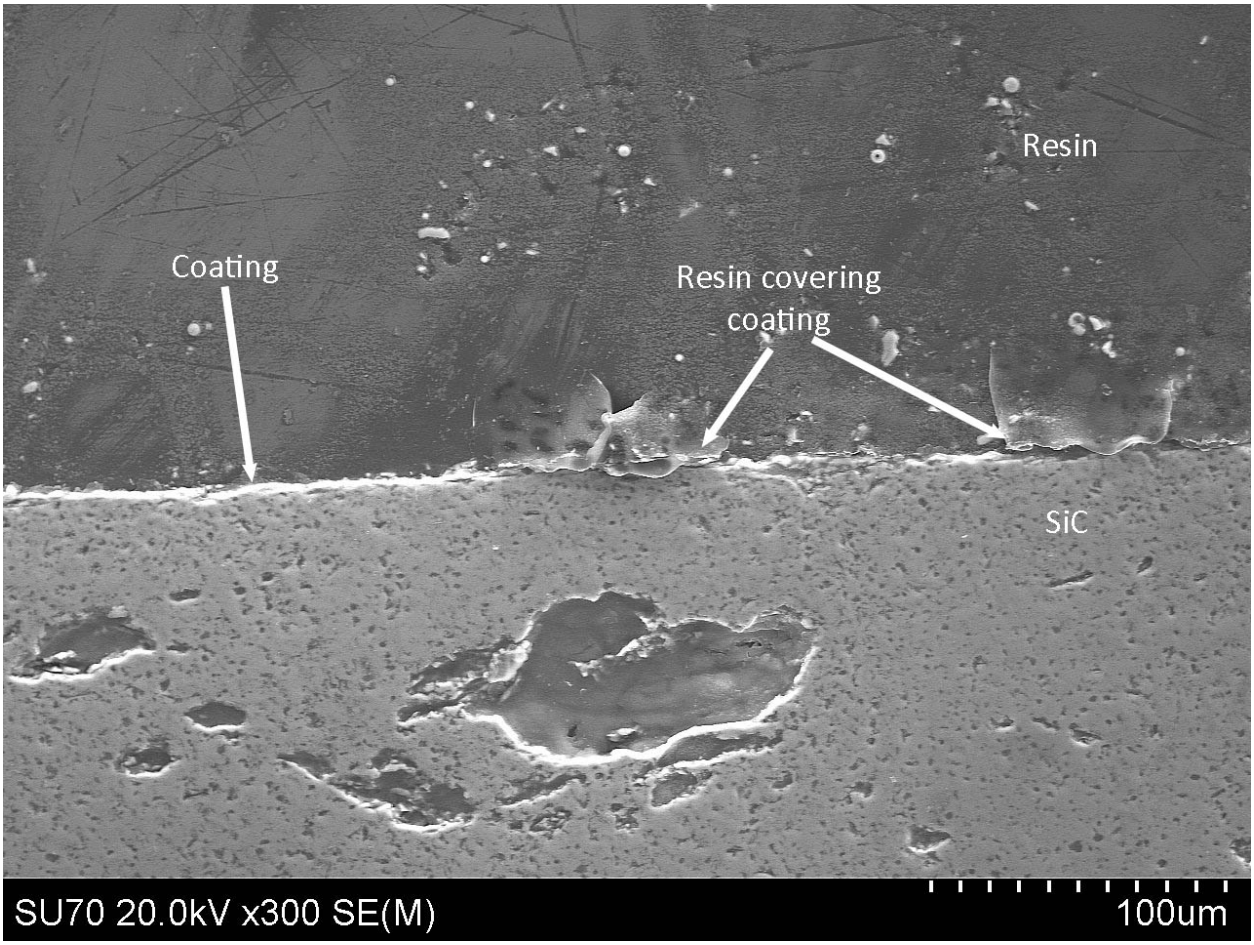


Figure 3.24: BSE SEM Image Showing Resin Behavior During Imaging

The Fe, Cr, and Al coatings in samples 10 and 11 are shown in Figure 3.25 and Figure 3.26, respectively. In both samples, the coatings diffused into SiC while still leaving a top layer. However, the HT sample (sample 10) has a larger top coat layer than that of the non-HT sample (sample 11). The electron beam evaporated coatings are significantly thicker than that measured by the crystal. This is partially attributed to many factors during experimentation such as macro-particle spitting (discussed in Section 3.4.2), crystal contamination, and feedback loop settings for deposition. These factors are all related to each other. For example, when macro-particle spitting occurs, not only does the specimen get affected by these undesired particles, but so does the crystal. As the crystal gets contaminated, erroneous deposition rates are measured, which in turn causes the feedback loop to go haywire by cycling through large power transients. Finally, it is this rapid

cycling of power that can give inconsistent film deposition along with the macro-particle spitting.

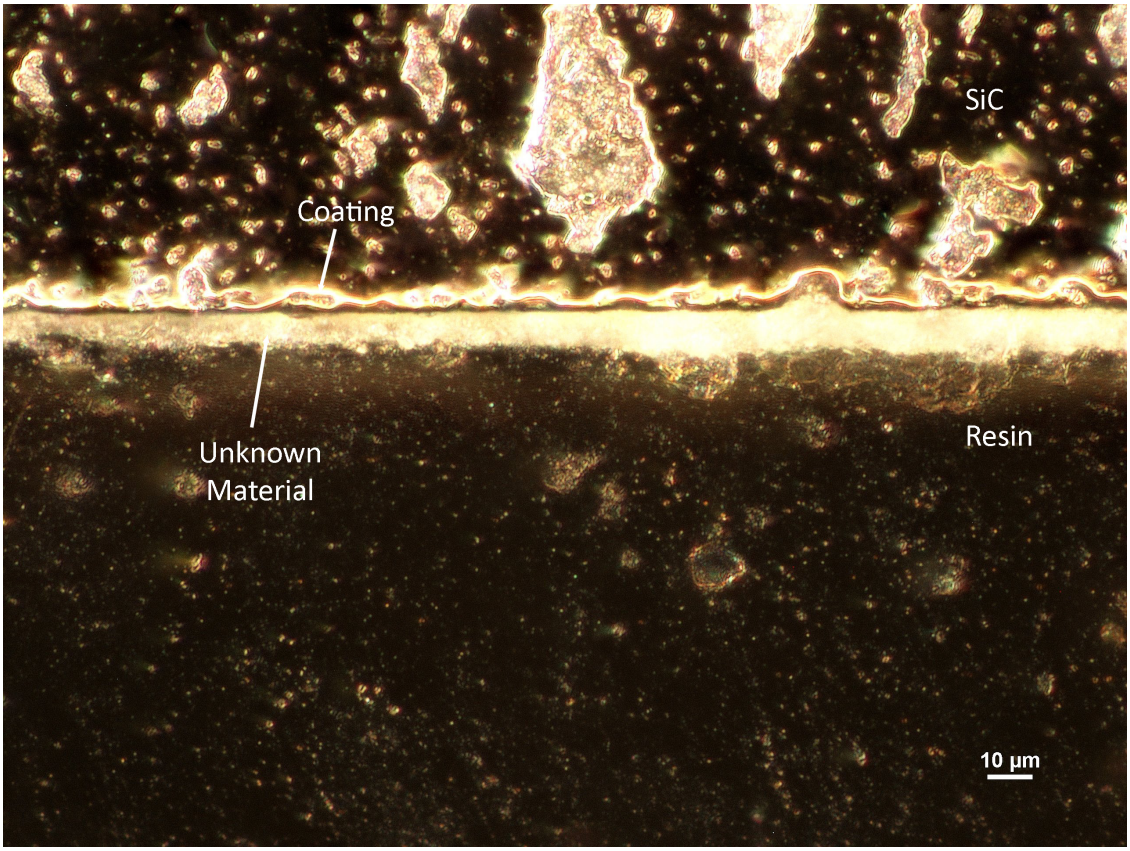


Figure 3.25: DF Optical Micrograph of HT Cr/Fe/Al Evaporated Sample 10

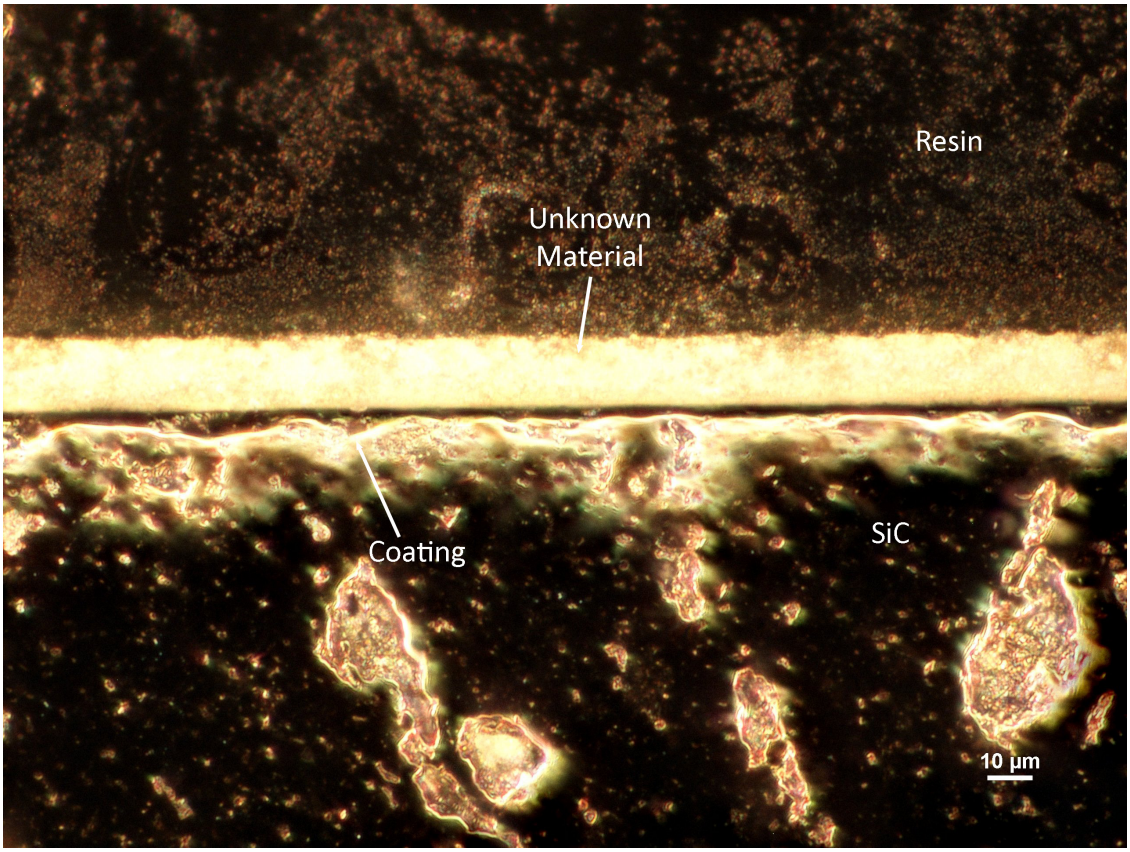


Figure 3.26: DF Optical Micrograph of Non-HT Cr/Fe/Al Evaporated Sample 11

## 3.5 Phase III-II: High-Temperature Diffusion Bonding

### 3.5.1 Motivation

The final set of experiments in this research consisted of high-temperature diffusion bonding of the coated specimens from Section 3.4 to FeCrAl. However, unlike the earlier diffusion studies from Section 3.2, diffusion bonding was assisted by induction heating in high vacuum, similar to the experimental setup used for casting. Pressure was maintained by compressing the samples in a graphite die with a weight stack on top, this is pictured in Figure 3.27. With a quantifiable, consistent pressure and higher temperatures, the coated specimens were expected to undergo diffusion with the FeCrAl interlayer.

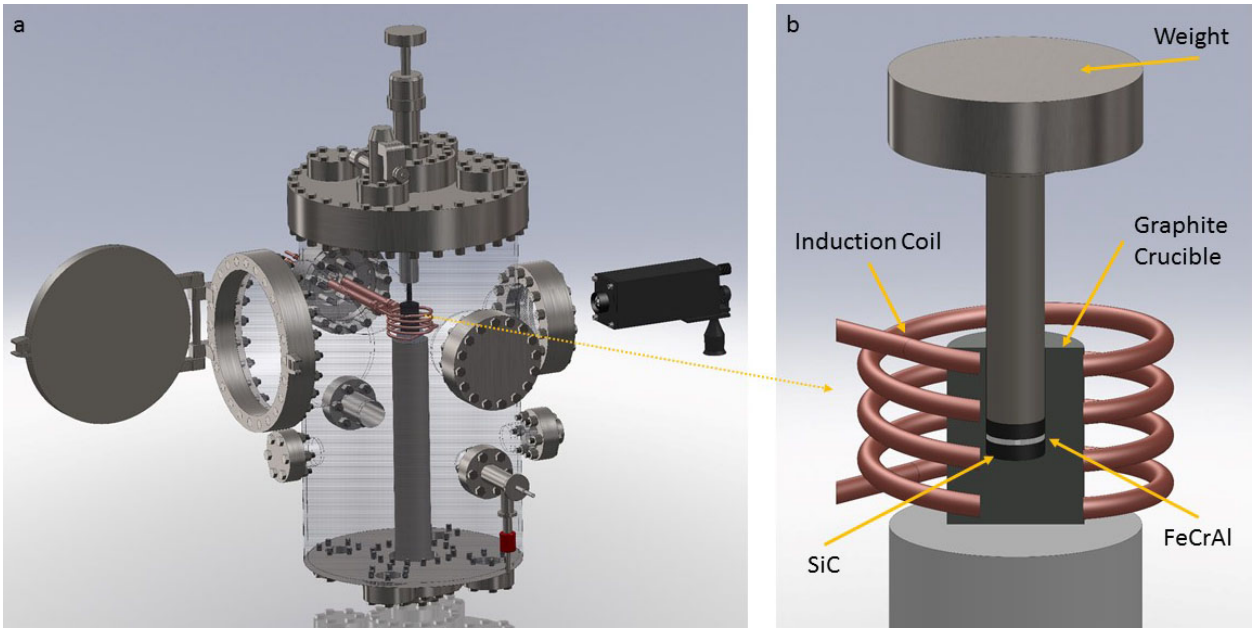


Figure 3.27: High-Temperature Graphite Die Hot Press

### 3.5.2 Methods

The Fe, Cr, and Al coated specimens were subjected to high-temperature diffusion bonding by induction heating assisted hot pressing. The graphite crucible contains a FeCrAl interlayer sandwiched between two coated SiC specimens. A graphite push-rod is used to compress the sample composite between the alumina rods. Pressure is applied by adding weight plates to a push/pull feed-through mechanism, which is connected to the alumina rod inside the chamber. Using the equations for area and pressure,

$$A = \pi r^2 \qquad (3.1) \qquad\qquad P = \frac{F}{A} \qquad (3.2)$$

an applied pressure of 870 psi (6 MPa) was obtained by using a force of 54 lbs for a specimen radius of 0.140". $A$, $r$, $P$, and $F$ are the area, radius, pressure, and force, respectively. The experimental setup is shown in Figure 3.28


Figure 3.28: High-Temperature Diffusion Experimental Setup

In addition to bonding the coated specimens, uncoated SiC was subjected to high-temperature diffusion bonding to compare with previous experiments that were conducted in Section 3.2. The operating parameters for the experiments are shown in Table 3.5. The experiments were conducted under a vacuum of $\sim$ 10 mTorr rather than using argon, and a constant pressure of 6 MPa was maintained.

Table 3.5: Operating Parameters for High-Temperature Diffusion Bonding Experiments

| Experiment | Coated Specimen Used (Sample # From Coating Section) | Temperature (°C) | Hold Time (Hr) |
|---|---|---|---|
| 1 | Fe/Cr/Al Coating (Sample 11 from Table 3.4) | 1300 | 1 |
| 2 | Fe/Cr/Al Coating (Sample 11 from Table 3.4) | 1200 | 1 |
| 3 | Al Coating (Sample 4 from Table 3.3) | 600 | 1 |
| 4 | Fe Coating (Sample 1 from Table 3.4) | 1250 | 1 |
| 5 | Cr Coating (Sample 3 from Table 3.4) | 1250 | 1 |
| 6 | No Coating | 1250 | 1 |

### 3.5.3 Results and Discussion

All samples, except sample 3, bonded. Unlike the unsuccessful diffusion bonding experiments in Section 3.2, the SiC and FeCrAl bonded into one sandwiched piece. Polished cross sections were obtained for SEM and EDS characterization, as shown in Figure 3.29.

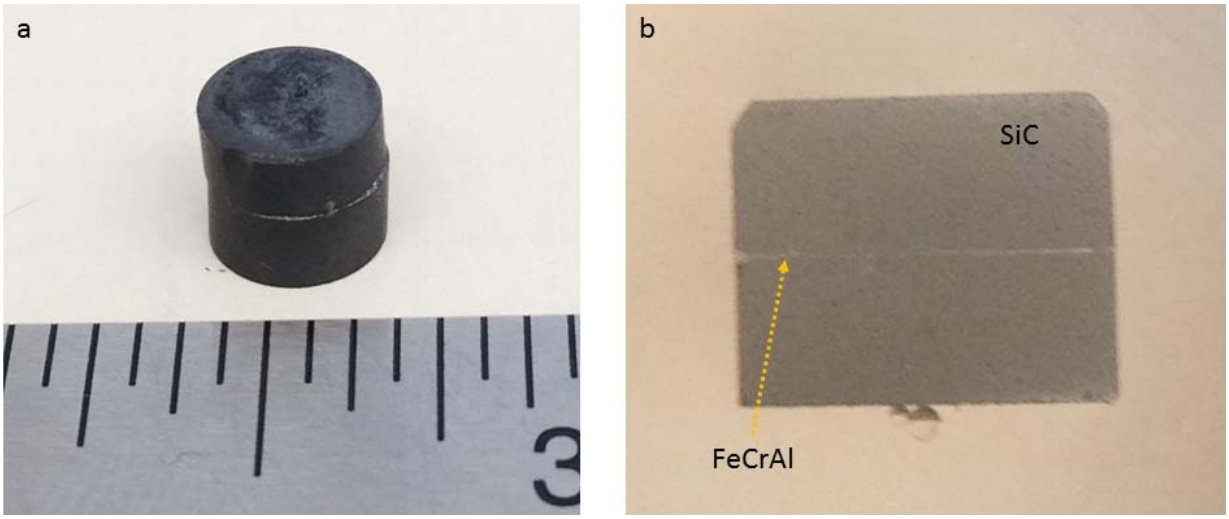


Figure 3.29: (a) Sandwiched Composite (b) Polished Cross Section Showing FeCrAl Interlayer

Figure 3.30 shows the SEM image and point spectrum of the FeCrAl layer as well as the FeCrAl-SiC interface in sample 1.[4] The high silicon content in the FeCrAl layer indicates that Si atoms diffused into the FeCrAl layer. There is also evidence of aluminum diffusing away from the FeCrAl layer as the content of aluminum is significantly higher near the FeCrAl-SiC interface.

[4]The optical and SEM images for Phase IV samples can be found in Section D

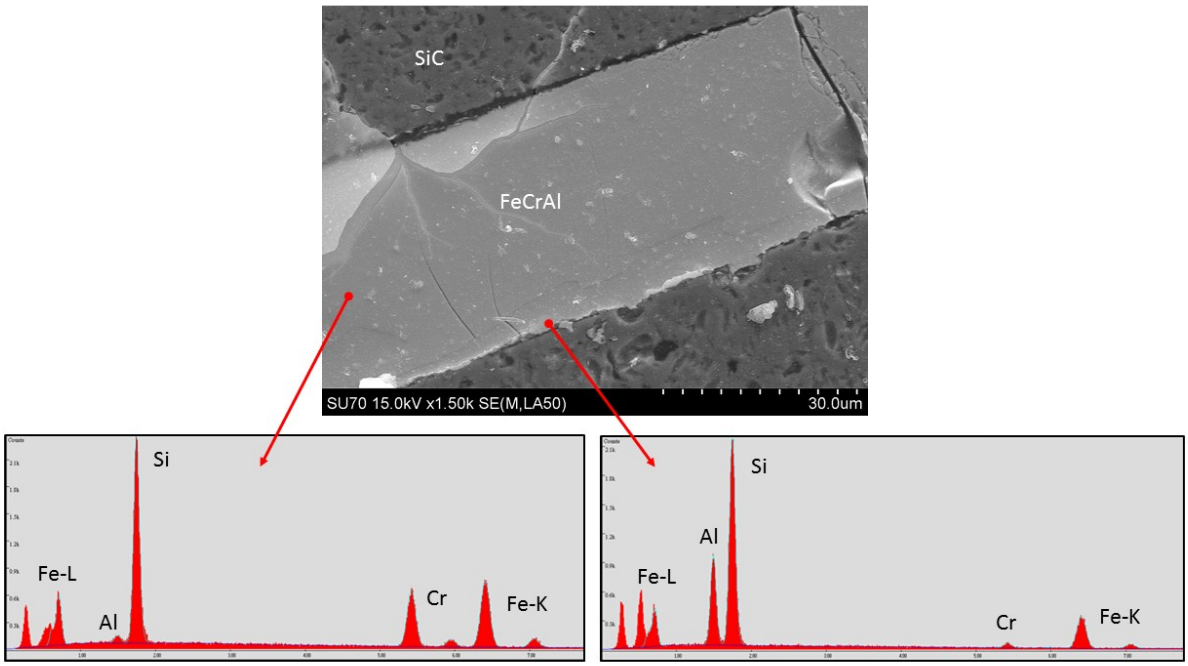


Figure 3.30: EDS Point Spectrum of HT-Diffusion Bonded Sample 1

EDS mapping was also conducted for this sample and it verified the silicon diffusion into the FeCrAl layer, as well as the localized aluminum presence along the interface. The mapping region of the silicon atoms show that there is a presence in the FeCrAl layer, which is indicated by the dark central region. Although it is dark, there is a contrast difference between the central region and the background. This confirms diffusion of SiC to FeCrAl. The mapping of silicon and FeCrAl is shown in Figure 3.31.

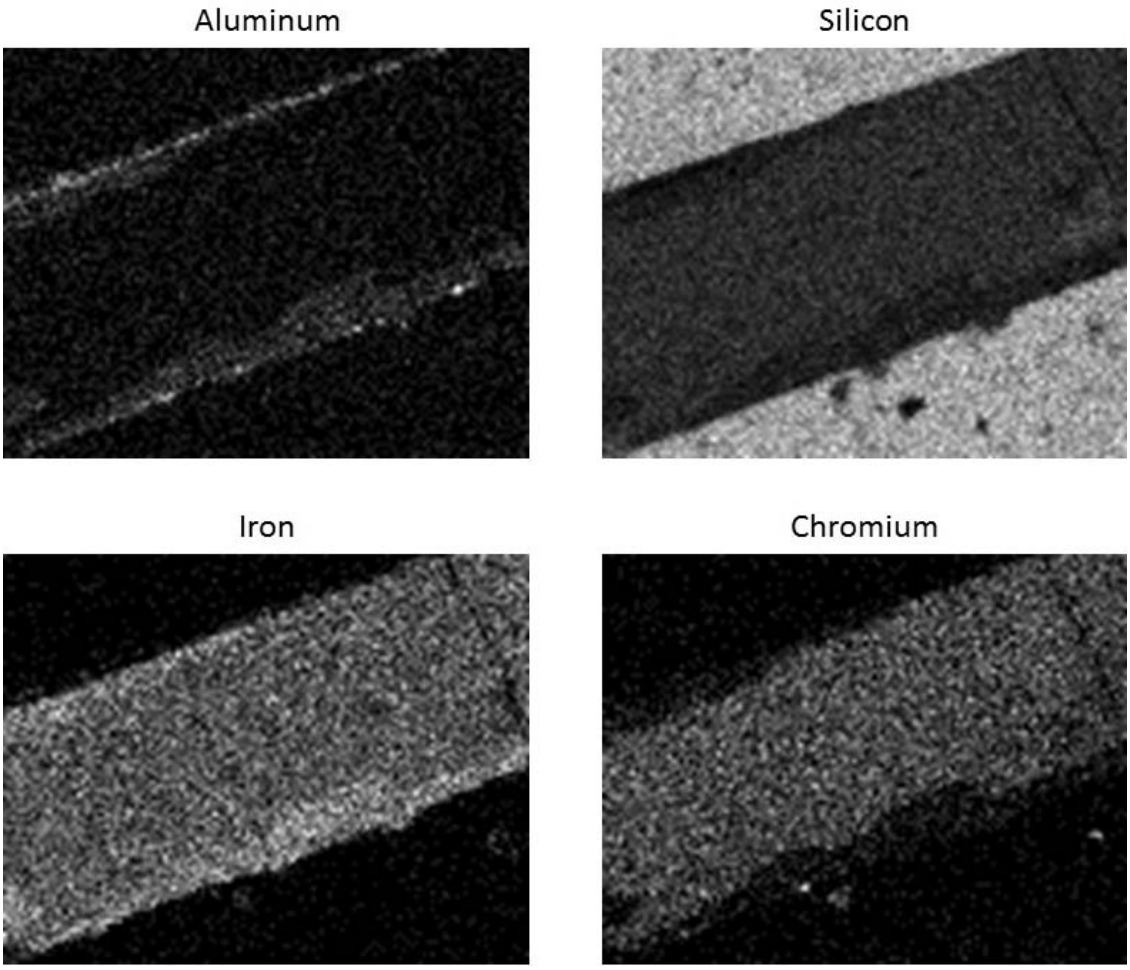


Figure 3.31: EDS Mapping of Different Regions in HT-Diffusion Bonded Sample 1

Sample 3, which was coated with aluminum via magnetron sputtering, did not bond to FeCrAl. When the sample was removed from the graphite crucible, the composite fell apart. This was expected as the sample was heated to 600 °C due to the low melting point of aluminum (660 °C). 1250 °C was found to be an ideal temperature for all the specimens, except for those coated with aluminum, due to the fact that the interdiffusion rates of SiC are high at those temperatures. The probability of forming carbide and silicide compounds in the weld region are high at temperatures exceeding 1200 °C [28]. Nonetheless, the aluminum coating adhered onto the SiC by confirmation of EDS mapping. The SEM images and region mapping for sample 3 are shown in Figure 3.32 and Figure 3.33, respectively.

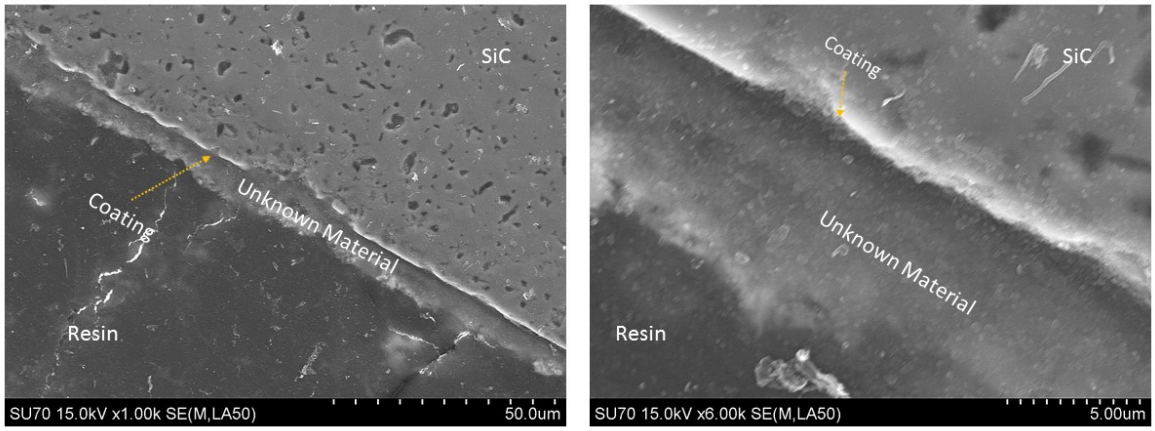


Figure 3.32: SEM Images of HT-Diffusion Bonded Sample 3

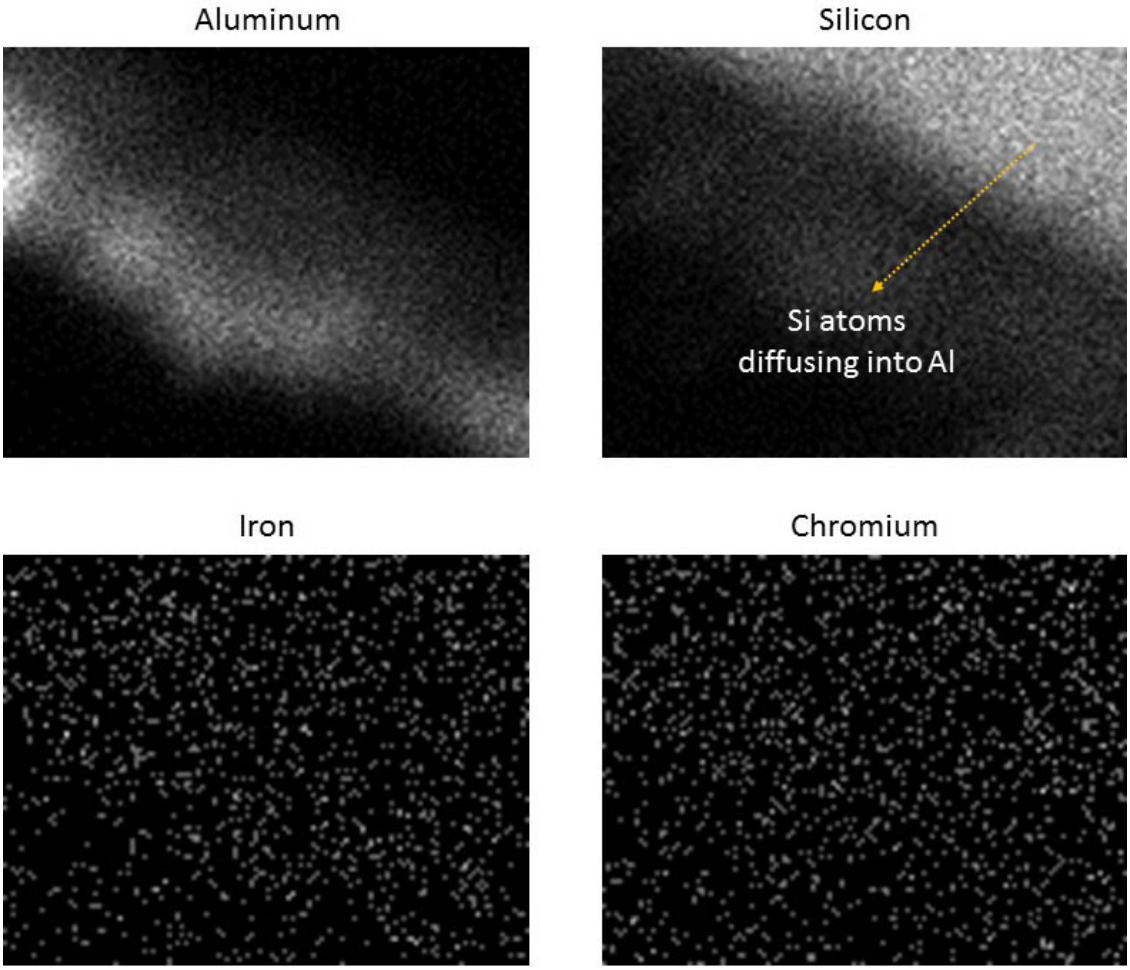


Figure 3.33: EDS Mapping of Different Regions in HT-Diffusion Bonded Sample 3

The mapping regions of chromium and iron show some counts, however those are considered "noise" and are not related to any particles that might have diffused from the FeCrAl tape.

Samples 2, 4, and 6 underwent damage during the polishing process, similar to that of the thin coatings in Section 3.4.3. As the SiC polishes, the residue from abrasion severely damages the thin and less hard FeCrAl layer in the composite. This problem is addressed in Section 5 and discusses other possible approaches to overcome this problem. This also occurred in samples 1 and 5, however, there were a couple of spots that were left unscathed. Although the SEM images show this, EDS point scans confirm that the pieces have consistent contents of silicon and FeCrAl as with samples 1 and 5. To illustrate this problem, the SEM images for samples 2 and 4 are shown in Figure 3.34.

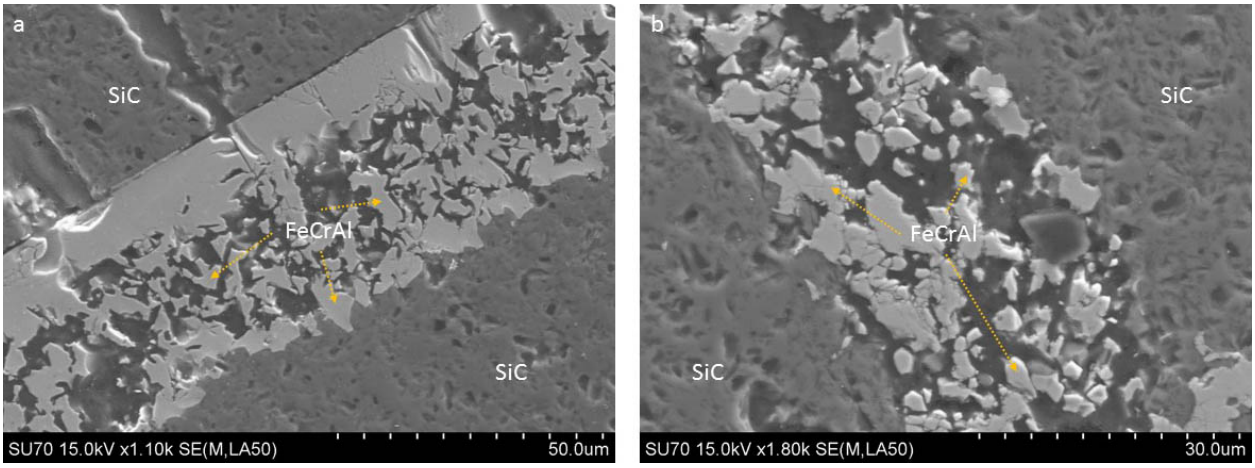


Figure 3.34: SEM Images of HT-Diffusion Bonded Samples (a) 2 and (b) 4

The point scan of sample 2 shows rich areas of silicon and FeCrAl, which are represented by the bright regions. The dark regions show high carbon content. Since all specimens are carbon coated for SEM imaging purposes, carbon has been excluded in most EDS scans as it will throw off the atomic and weight percentages. The EDS point scans for sample 2 are shown in Figure 3.35.

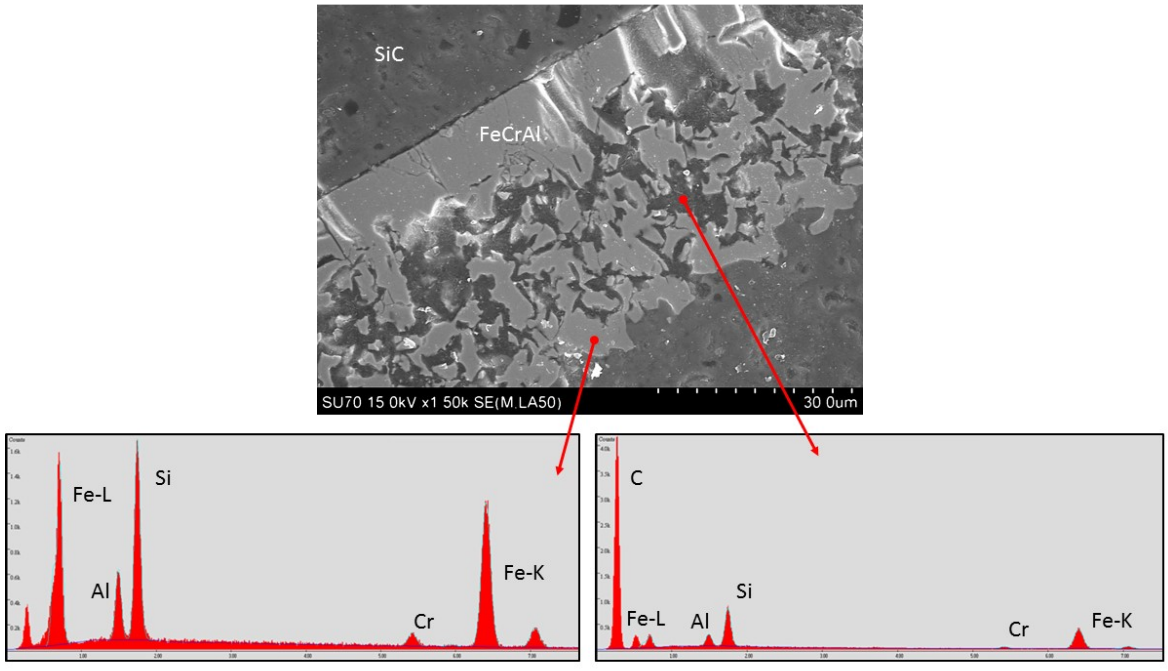


Figure 3.35: EDS Point Spectrum of HT-Diffusion Bonded Sample 2

While most of the samples exhibited similar characteristics, sample 5 showed a small diffusion

layer between SiC and FeCrAl. This is shown in Figure 3.36.

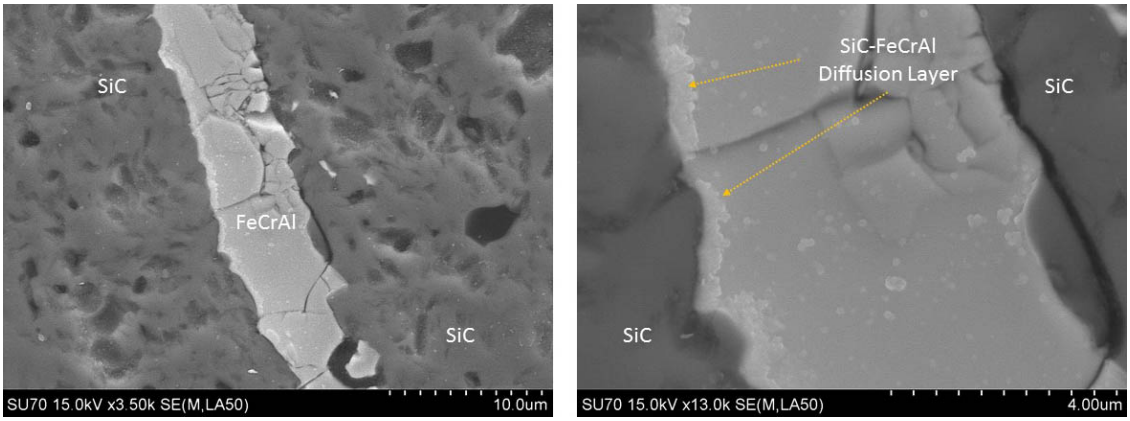


Figure 3.36: SEM Images of HT-Diffusion Bonded Sample 5

The SEM and EDS results clearly show that SiC bonded to FeCrAl through high-temperature diffusion at temperatures between 1200 to 1300 °C at an applied pressure of 6 MPa for one hour. Further adhesion characterization can be performed by shear adhesion testing, which is briefly discussed in Section 5.

# Chapter 4

# Conclusions

Different methods have been investigated to join and hermetically seal SiC in an effort to develop a viable ATF clad for LWR applications. Preliminary diffusion bonding experiments revealed that FeCrAl bonded to aluminum. However, SiC did not bond to FeCrAl due to a large mismatch in CTE, as well as pressure and temperature limitations. Adding an aluminum interlayer between SiC and FeCrAl facilitated bonding in these experiments. Thick film coatings of aluminum and FeCrAl to SiC were not successful in hermetically sealing SiC, which was partially attributed to the wetting capability of SiC in contact with the molten material. With the case of FeCrAl, the SiC was consumed or infiltrated by FeCrAl. This is due to the high melting temperature of FeCrAl approaching the sublimation temperature of sintered SiC.

Thin film deposition of Fe, Cr, and Al onto SiC was conducted in an effort to hermetically seal and join SiC. Dense metallic coatings deposited onto porous SiC was investigated for hermetic sealing. However, further characterization is necessary to evaluate the sealing capability of such coatings. In addition to providing hermetic sealing, thin film coatings were used as compositional interlayers to bond SiC to FeCrAl to ultimately join SiC specimens. It was concluded that compositional graded layers were necessary to reduce the large CTE mismatch between these two largely dissimilar materials. This was accomplished by thin film deposition of Fe, Cr, and Al layers assisted by electron beam evaporation and magnetron sputtering. High-temperature diffusion

bonding of the coated SiC to FeCrAl resulted in bonding between the two materials as qualitatively characterized by SEM and EDS. Further characterization, such as adhesion testing, is necessary to compare the integrity of the joints among the different coated specimens as well as the non-coated specimens.

# Chapter 5

# Recommendations

An alternative metallographic preparation technique must be used during post-processing. The current method of orbital grinding/polishing is detrimental to the finish for composites consisting of materials that have a large difference in hardness. Polishing a composite that contains hard SiC and relatively softer FeCrAl is rather complicated since the materials are largely dissimilar in hardness. Other polishing procedures, such as vibratory polishing, should be considered to overcome this problem.

Other characterization techniques, such as adhesion and corrosion testing, should be explored to determine the quality and durability of the coatings and bonded joints. These techniques can more accurately distinguish the affects of the different coatings. Furthermore, characterization by nanoindentation can also be performed to determine the hardness and other mechanical properties of the coatings.

Methods, such as plasma spray and laser beam scanning, should be considered for commercialization coating applications. These methods, which do not require high vacuum environments, have been explored for coating zirconium-based clads. This can be an economic solution for coating long rods, where a vacuum chamber could not accommodate.

# Bibliography


[1] D. G. Cacuci, *Handbook of Nuclear Engineering*, Springer, 1st edition ed., 2010.

[2] T. Rajan, R. Pillai, and B. Pai, "Reinforcement coatings and interfaces in aluminum metal matrix composites," *Journal of Materials Science* **33**(14), p. 3491, 1998.

[3] M. M. Abu-Khader, "Recent advances in nuclear power: A review," *Progress in Nuclear Energy* **51**, pp. 225–235, 3 2009.

[4] S. J. Zinkle and G. S. Was, "Materials challenges in nuclear energy," *Acta Materialia* **61**, pp. 735–758, 2 2013.

[5] T. Alam, M. K. Khan, M. Pathak, K. Ravi, R. Singh, and S. K. Gupta, "A review on the clad failure studies," *Nuclear Engineering and Design* **241**(9), pp. 3658–77, 2011.

[6] H. M. Chung and G. R. Thomas, "Zircaloy-oxidation and hydrogen-generation rates in degraded-core accident situations," Tech. Rep. Contract W-31-109-ENG-38, Argonne National Laboratory, 02 1983.

[7] A. L. Camp, J. C. Cummings, M. P. Sherman, C. F. Kupiec, R. J. Healy, J. S. Caplan, J. R. Sandhop, and J. H. Saunders, "Light water reactor hydrogen manual," Tech. Rep. M1: NUREG/CR–2726, Sandia National Laboratories, 1983.

[8] N. E. Agency, "Nuclear fuel safey criteria technical review," Tech. Rep. NEA Report No. 7072, OECD, 2012.

[9] S. J. Zinkle, K. A. Terrani, J. C. Gehin, L. J. Ott, and L. L. Snead, "Accident tolerant fuels for lwrs: A perspective," *Journal of Nuclear Materials* **448**(13), pp. 374–379, 2014.

[10] D. A. Powers and R. O. Meyer, "Cladding swelling and rupture models for loca analysis technical report," Tech. Rep. NRC Report NUREG-0630, Nuclear Regulatory Commission, 1980.

[11] K. A. Terrani, S. J. Zinkle, and L. L. Snead, "Advanced oxidation-resistant iron-based alloys for lwr fuel cladding," *Journal of Nuclear Materials* **448**, pp. 420–435, 5 2014.

[12] L. O. Jernkvist and A. R. Massih, "Nuclear fuel behaviour under reactivity-initiated accident (ria) conditions," Tech. Rep. NEA Report No. 6847, Nuclear Energy Agency, OECD, 2010.

[13] I. N. S. A. Group, "Insag-7: The chernobyl accident - updating of insag-1," Tech. Rep. IAEA Safety Series Report 75-INSAG-7, International Atomic Energy Agency, 1992.

[14] K. Yueh, D. Carpenter, and H. Feinroth, "Clad in clay," 2010.

[15] H. Feinroth, "Silicon carbide triplex nuclear fuel cladding: An alternative to zircaloy that avoids severe core damage during accidents," in *Presentation to the Israel Nuclear Societies*, 2012.

[16] S. Bragg-Sitton, "Development of advanced accident-tolerant fuels for commercial lwrs," 2014.

[17] T. Cheng, J. R. Keiser, M. P. Brady, K. A. Terrani, and B. A. Pint, "Oxidation of fuel cladding candidate materials in steam environments at high temperature and pressure," *Journal of Nuclear Materials* **427**, pp. 396–400, 8 2012.

[18] J. P. Dobisesky, J. G. Richard, E. E. Pilat, and M. S. Kazimi, "High burnup pwr core design with silicon carbide cladding," *Transactions of the American Nuclear Society* **104**, pp. 727–8, 2011.

[19] J. P. Dobisesky, D. Carpenter, E. Pilat, and M. S. Kazimi, "Pwr cores with silicon carbide cladding," in *International Conference on the Physics of Reactors 2012: Advances in Reactor Physics, PHYSOR 2012, April 15, 2012 - April 20*, **2**, pp. 1435–1451, American Nuclear Society, (Knoxville, TN, United states), 2012.

[20] L. Hallstadius, S. Johnson, and E. Lahoda, "Cladding for high performance fuel," *Progress in Nuclear Energy* **57**, pp. 71–76, 5 2012.

[21] L. L. Snead, T. Nozawa, Y. Katoh, T.-S. Byun, S. Kondo, and D. A. Petti, "Handbook of sic properties for fuel performance modeling," *Journal of Nuclear Materials* **371**(1-3), pp. 329–77, 2007.

[22] B. Matović and T. Yano, *Chapter 3.1 - Silicon Carbide and Other Carbides: From Stars to the Advanced Ceramics*, pp. 225–244. Handbook of Advanced Ceramics (Second Edition), Academic Press, Oxford, 2013.

[23] Y. Katoh, L. L. Snead, C. H. H. J., T. Hinoki, M. Ferraris, and S. T. Gonczy, "Joining silicon carbide for advanced lwr fuel cladding," in *2012 Winter Meeting*, **107**, pp. 405–6, Oak Ridge Nat. Lab., Oak Ridge, TN, United States, American Nuclear Society, (USA), 11-15 Nov. 2012 2012.

[24] Y. Katoh, N. Hashimoto, S. Kondo, L. L. Snead, and A. Kohyama, "Microstructural development in cubic silicon carbide during irradiation at elevated temperatures," *Journal of Nuclear Materials* **351**, pp. 228–240, 6/1 2006.

[25] J. M. Fernndez, A. Muoz, A. R. de Arellano Lpez, F. M. V. Feria, A. Domnguez-Rodrguez, and M. Singh, "Microstructuremechanical properties correlation in siliconized silicon carbide ceramics," *Acta Materialia* **51**, pp. 3259–3275, 6/27 2003.

[26] P. Colombo, B. Riccardi, A. Donato, and G. Scarinci, "Joining of sic/sicf ceramic matrix composites for fusion reactor blanket applications," *Journal of Nuclear Materials* **278**, pp. 127–135, 4 2000.

[27] Y.-I. Jung, S.-H. Kim, H.-G. Kim, J.-Y. Park, and W.-J. Kim, "Microstructures of diffusion bonded sic ceramics using ti and mo interlayers," *Journal of Nuclear Materials* **441**(1-3), pp. 510–513, 2013.

[28] B. V. Cockeram, "Flexural strength and shear strength of silicon carbide to silicon carbide joints fabricated by a molybdenum diffusion bonding technique," *Journal of the American Ceramic Society* **88**(7), pp. 1892–1899, 2005.

[29] S. Morozumi, M. Endo, M. Kikuchi, and K. Hamajima, "Bonding mechanism between silicon carbide and thin foils of reactive metals," *Journal of Materials Science* **20**, pp. 3976–82, 11 1985.

[30] J. D. Stempien, D. M. Carpenter, G. Kohse, and M. S. Kazimi, "Characteristics of composite silicon carbide fuel cladding after irradiation under simulated pwr conditions," *Nuclear Technology* **183**(1), pp. 13–29, 2013.

[31] T. Cheng and P. F. Tortorelli, "Silicon carbide oxidation in high-pressure steam," *Journal of the American Ceramic Society* **96**(7), pp. 2330–2337, 2013.

[32] N. S. Jacobson, A. J. Eckel, A. K. Misra, and D. L. Humphrey, "Ractions of sic with h2/h2o/ar mixtures at 1300c," *Journal of the American Ceramic Society* **73**(8), pp. 2330–2332, 1990.

[33] D. S. Fox, E. J. Opila, and R. E. Hann, "Paralinear oxidation of cvd sic in simulated fuel-rich combustion," *Journal of the American Ceramic Society* **83**(7), pp. 1761–1767, 2000.

[34] J.-Y. Park, I.-H. Kim, Y.-I. Jung, H.-G. Kim, D.-J. Park, and W.-J. Kim, "Long-term corrosion behavior of cvd sic in 360 °c water and 400 °c steam," *Journal of Nuclear Materials* **443**, pp. 603–607, 11 2013.

[35] R. J. Borg and G. J. Dienes, *An Introduction to Solid State DIffusion*, Academic Press, San Diego, 1988.

[36] E. A. Brandes and G. B. Brook, *Smithells Metals Reference Book*, Butterworth-Heinemann Ltd., Oxford, 7th ed., 1992.

[37] H. S. Carslaw and J. C. Jaeger, *Conduction of Heat in Solids*, Oxford University Press, Oxford, 2nd ed., 1986.

[38] J. Crank, *The Mathematics of Diffusion*, Oxford University Press, Oxford, 2nd ed., 1980.

[39] M. Glicksman, *Diffusion in Solids*, John Wiley & Sons, New York, 2000.

[40] P. G. Shewmon, *Diffusion in Solids*, McGraw-Hill Book Company, New York, 1963.

[41] N. F. Kazakov, *Diffusion Bonding of Materials*, Pergamon Press ; Mir Publishers, Oxford [Oxfordshire]; New York; Moscow, 1985.

[42] D.-S. Han and J.-K. Yoon, "The wettability of silicon carbide by liquid pure aluminum and aluminum alloys," in *1994 SAE International Congress and Exposition, February 28, 1994 - March 3*, Hyundai Motor Co., Korea, Republic of, SAE International, (Detroit, MI, United states), 1994 1994.

[43] M. Pech-Canul, R. N. Katz, and M. M. Makhlouf, "Optimum parameters for wetting silicon carbide by aluminum alloys," *Metallurgical and Materials Transactions A (Physical Metallurgy and Materials Science)* **31A**, pp. 565–73, 02 2000.

[44] M. Rahaman, *Ceramic Processing*, CRC Press, Florida, 1 ed., 2007.

[45] M. Faustini, B. Louis, P. A. Albouy, M. Kuemmel, and D. Grosso, "Preparation of sol-gel films by dip-coating in extreme conditions," *Journal of Physical Chemistry* **114**(17), pp. 7637–7645, 2010.

[46] S. Zinn, *Theory of Induction Heating*, p. 9. Elements of Induction Heating: Design, Control, and Applications, ASM International, Ohio, 1988.

[47] R. E. Haimbaugh, "Practical induction heat treating," Tech. Rep. 06098G, ASM International, 2001.

[48] D. L. Smith, *Thin-film deposition : principles and practice*, McGraw-Hill, New York, 1995.

[49] K. L. C. 1933, *Thin Film Phenomena*, McGraw-Hill, New York, 1969.

[50] K. Seshan, *Handbook of thin film deposition techniques, processes, and technologies*, Elsevier, Waltham, Mass, 3rd edition ed., 2012.

[51] J. E. Mahan, *Physical Vapor Deposition of Thin Films*, Wiley-Interscience, New York, 1st edition ed., 2000.

[52] W. Kern, *Thin Film Processes II*, Elsevier Science, Burlington, 1991.

[53] F. Riffard, H. Buscail, E. Caudron, R. Cueff, C. Issartel, and S. Perrier, "Yttrium implantation effect on 304l stainless steel high temperature oxidation at 1000 °c," *Journal of Materials Science* **37**(18), pp. 3925–3933, 2002.

[54] T. Choh and T. Oki, "Wettability of sic to aluminium and aluminium alloys," *Materials Science and Technology* **3**, pp. 378–85, 05 1987.

# Appendices

# List of Figures in Appendicies

# Appendix A

# Diffusion Bonding Results

The operating parameters for the preliminary diffusion bonding experiments are shown in Table 3.1. Bonding is qualitatively characterized by optical and/or SEM.

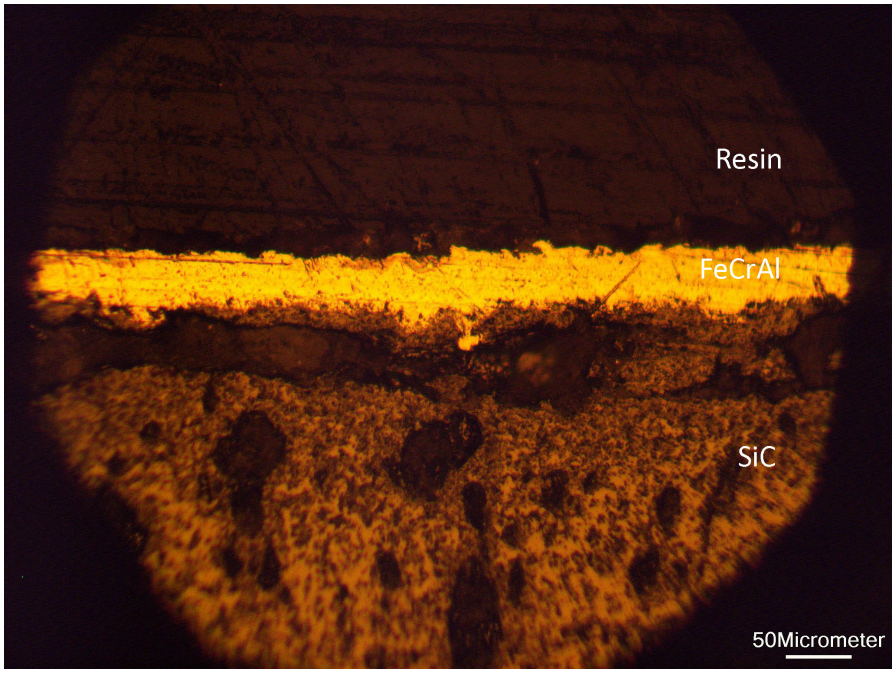


Figure A.1: Optical Micrograph of Diffusion Bonded Sample 1

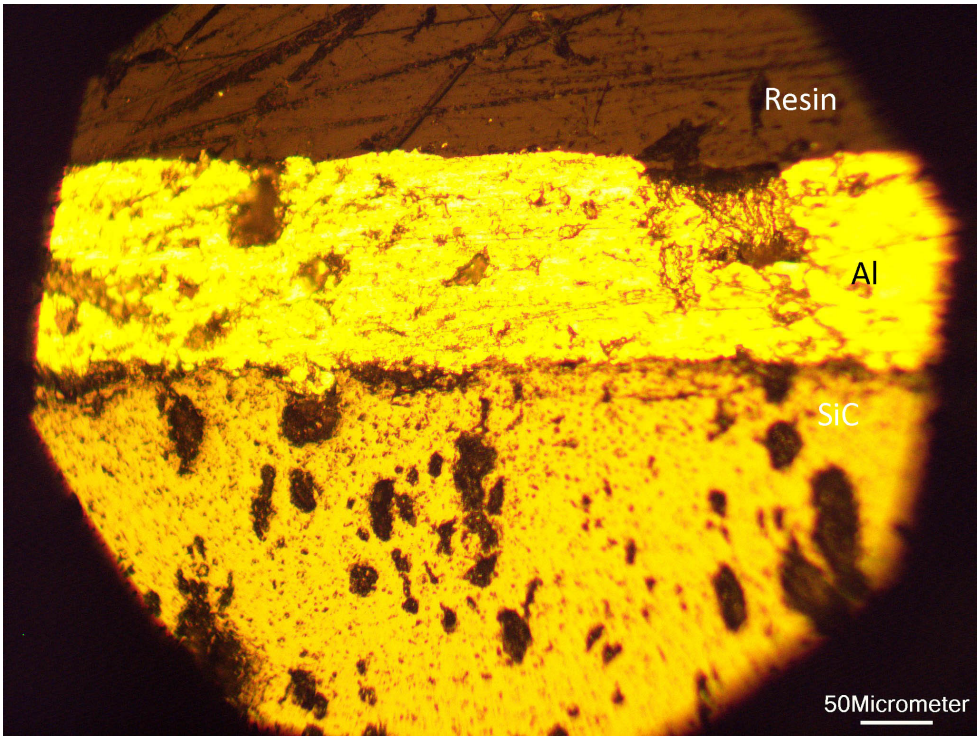


Figure A.2: Optical Micrograph of Diffusion Bonded Sample 2

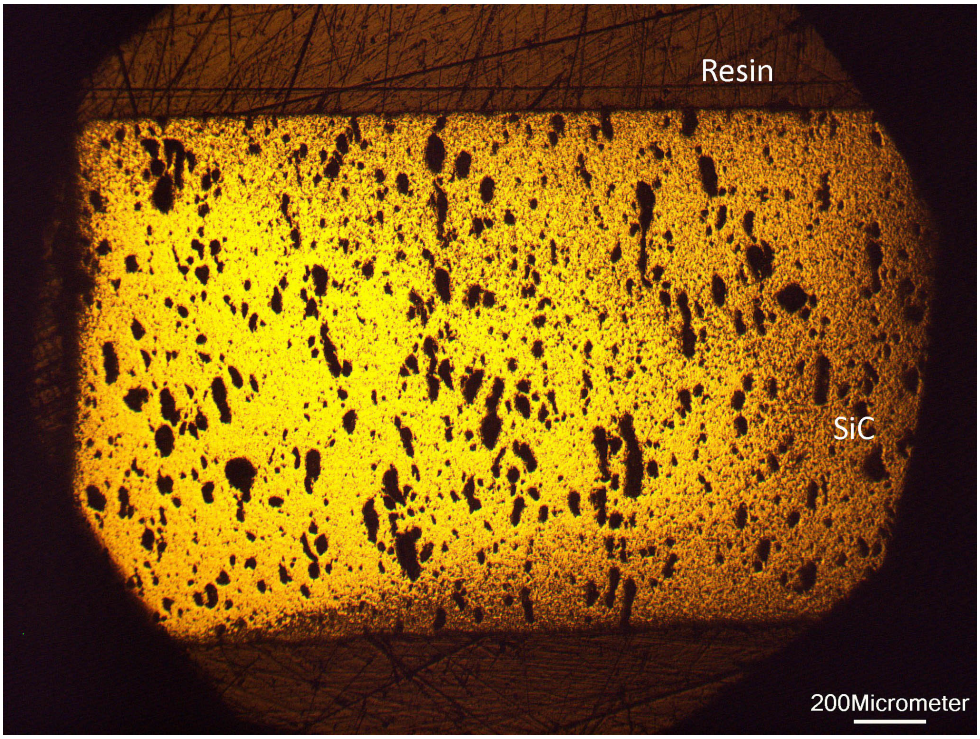


Figure A.3: Optical Micrograph of Diffusion Bonded Sample 3

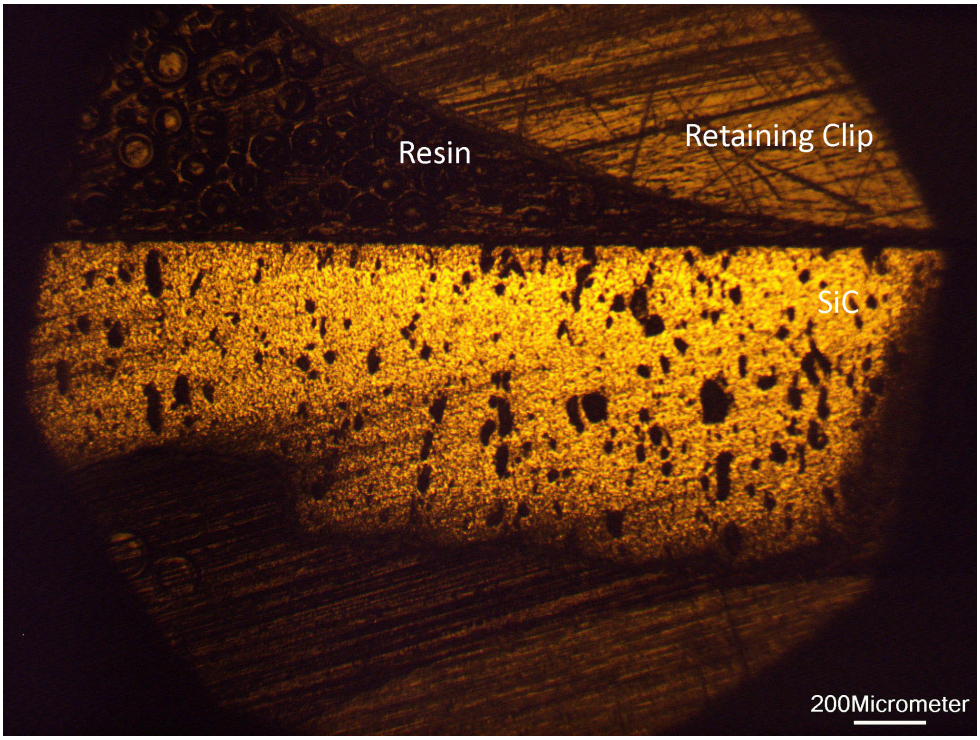


Figure A.4: Optical Micrograph of Diffusion Bonded Sample 4

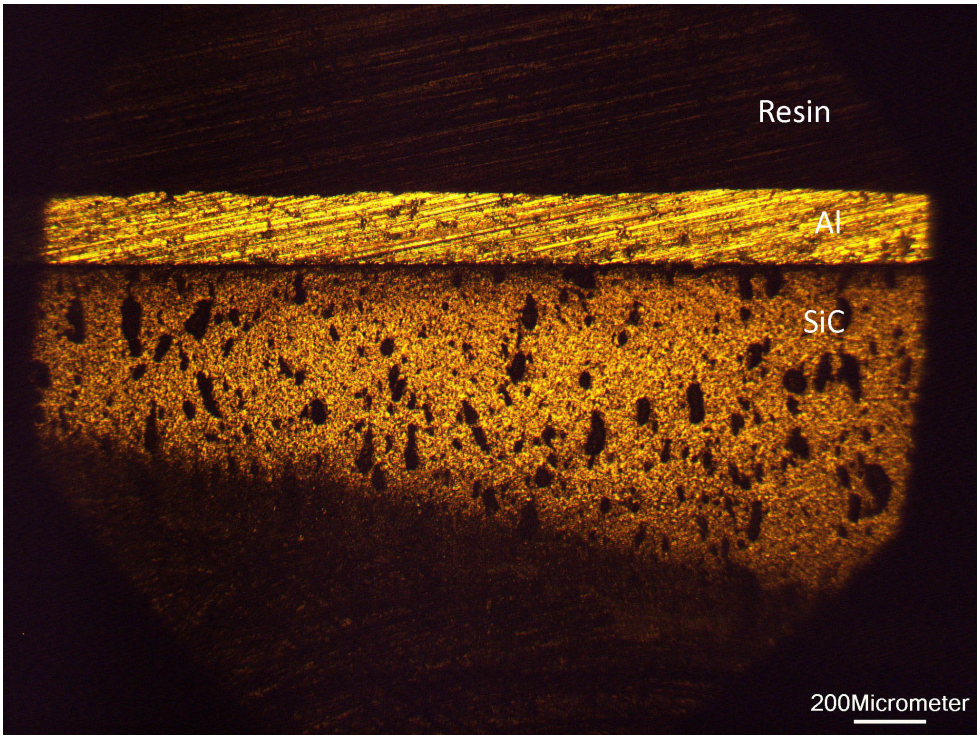


Figure A.5: Optical Micrograph of Diffusion Bonded Sample 5

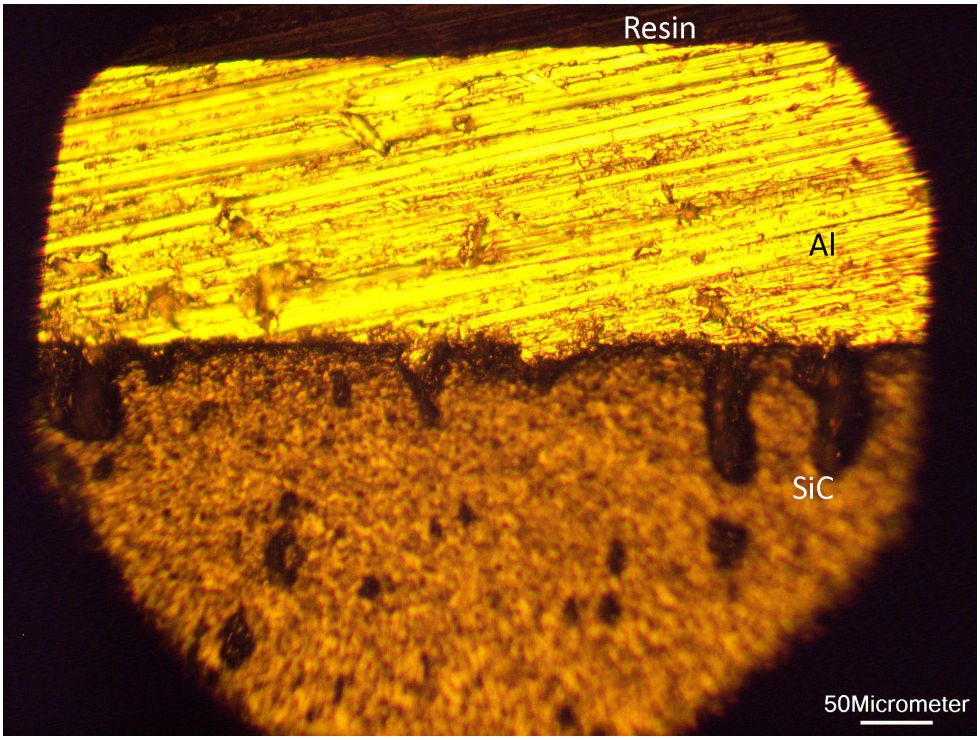


Figure A.6: Optical Micrograph of Diffusion Bonded Sample 5

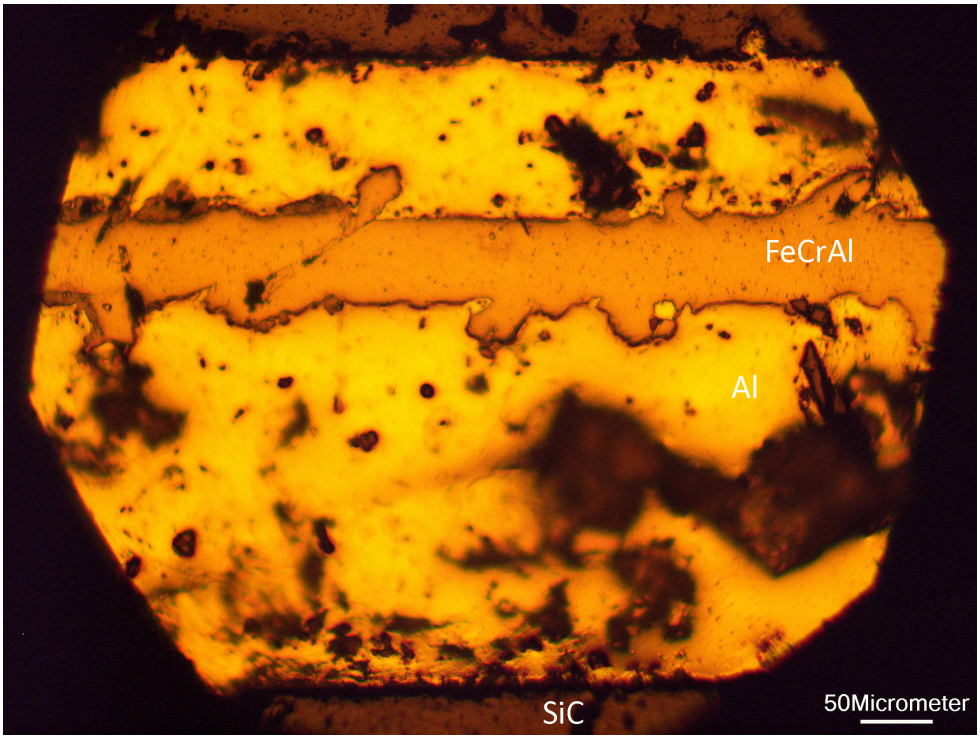


Figure A.7: Optical Micrograph of Diffusion Bonded Sample 6

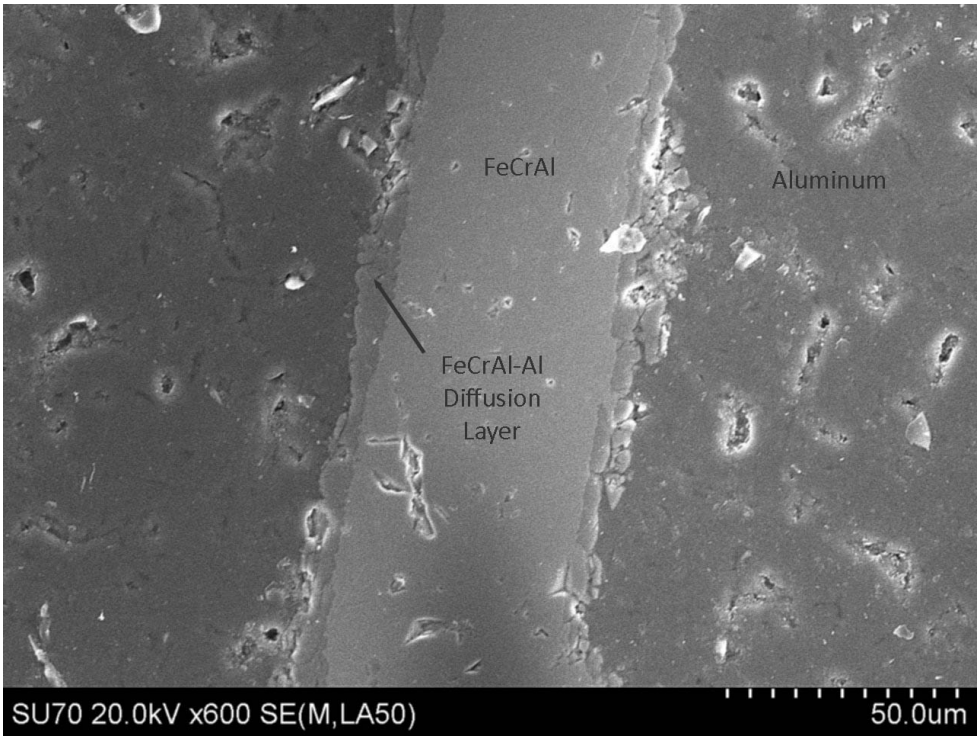


Figure A.8: SEM Image of Diffusion Bonded Sample 6

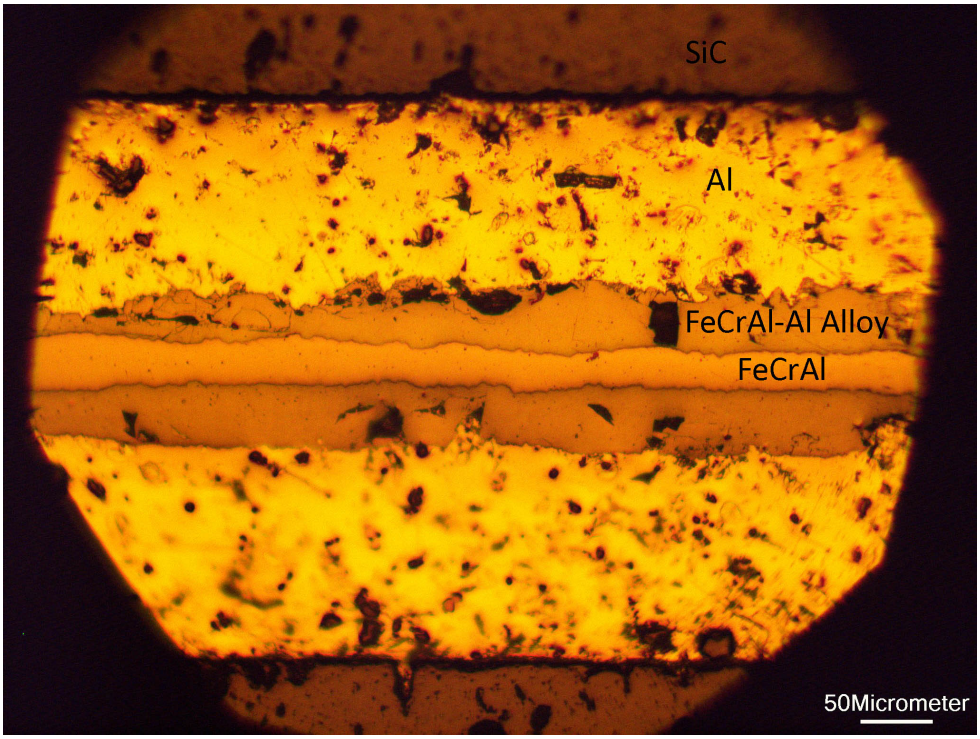


Figure A.9: Optical Micrograph of Diffusion Bonded Sample 7

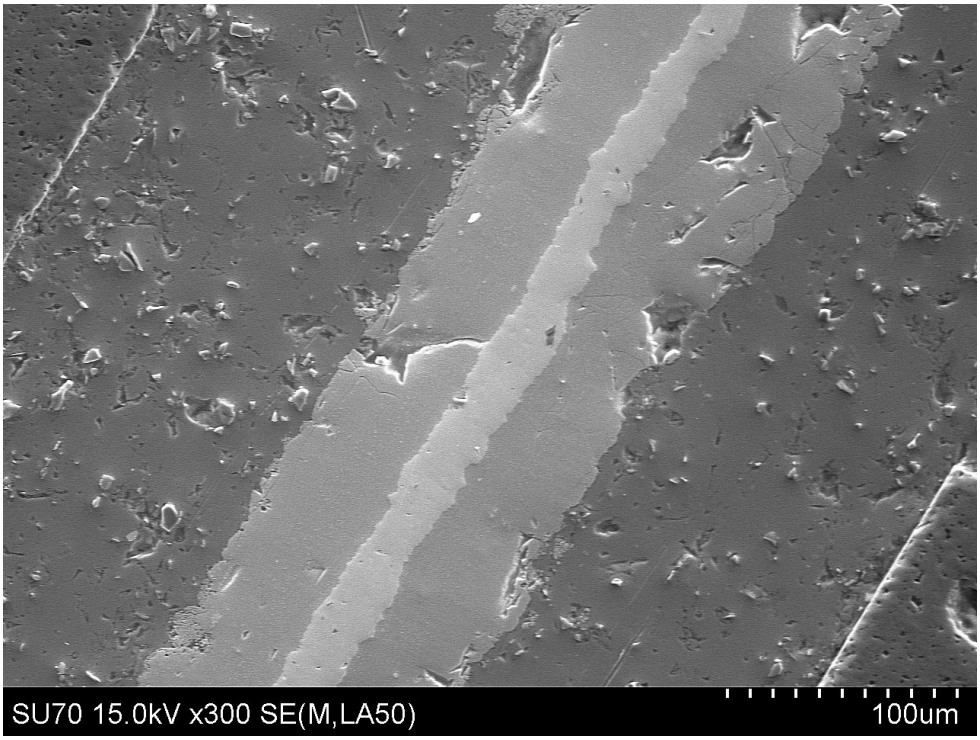


Figure A.10: SEM Image of Diffusion Bonded Sample 7

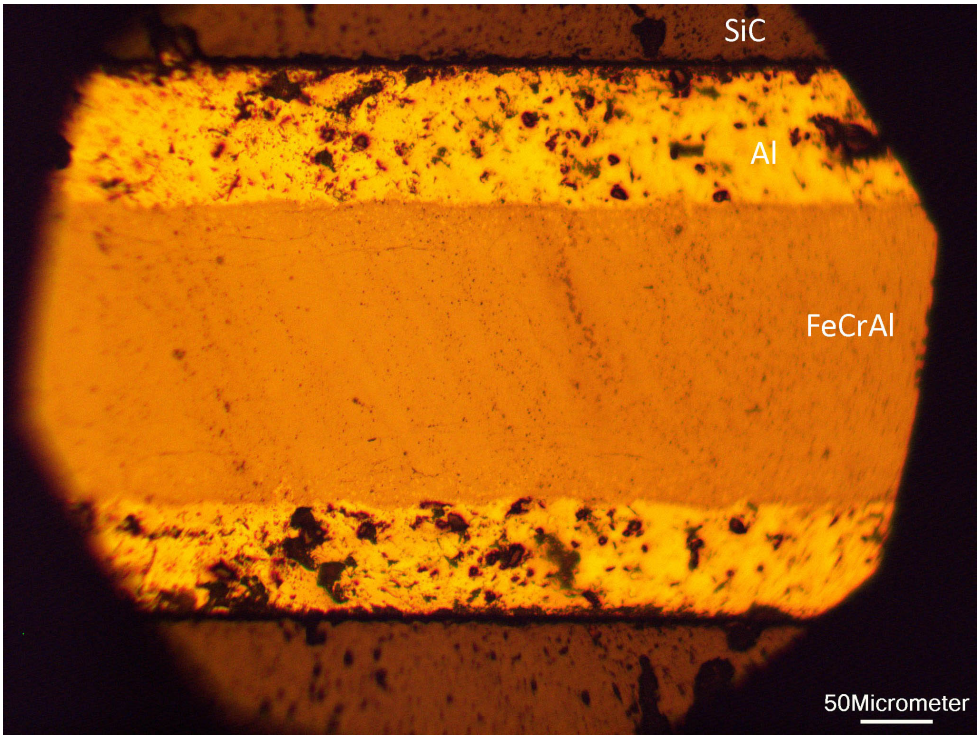


Figure A.11: Optical Micrograph of Diffusion Bonded Sample 8

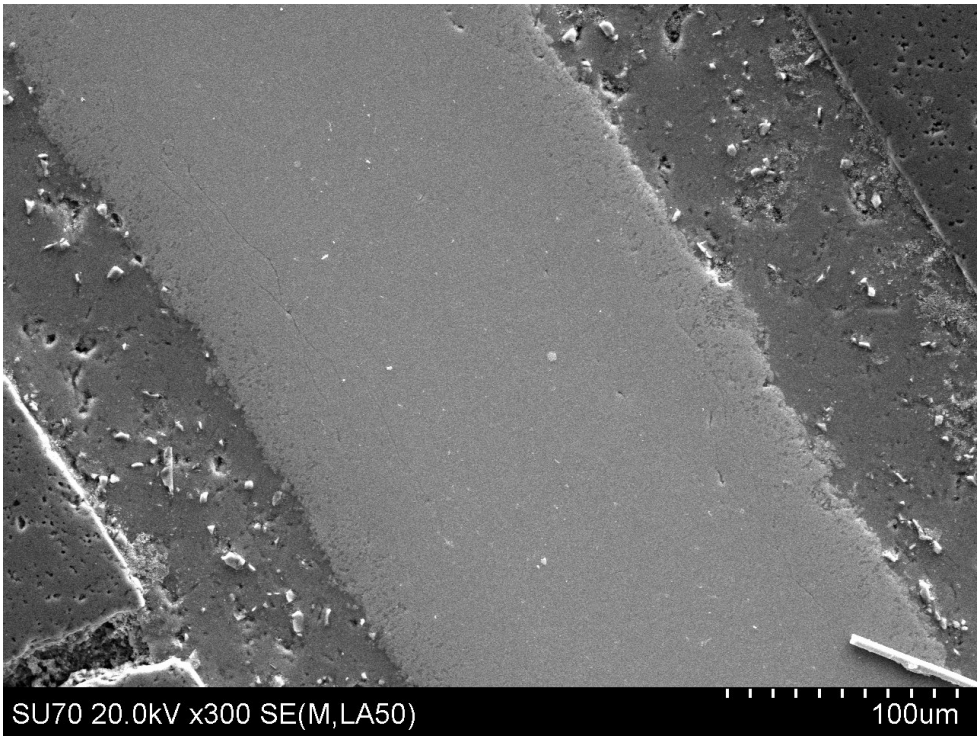


Figure A.12: SEM Image of Diffusion Bonded Sample 8

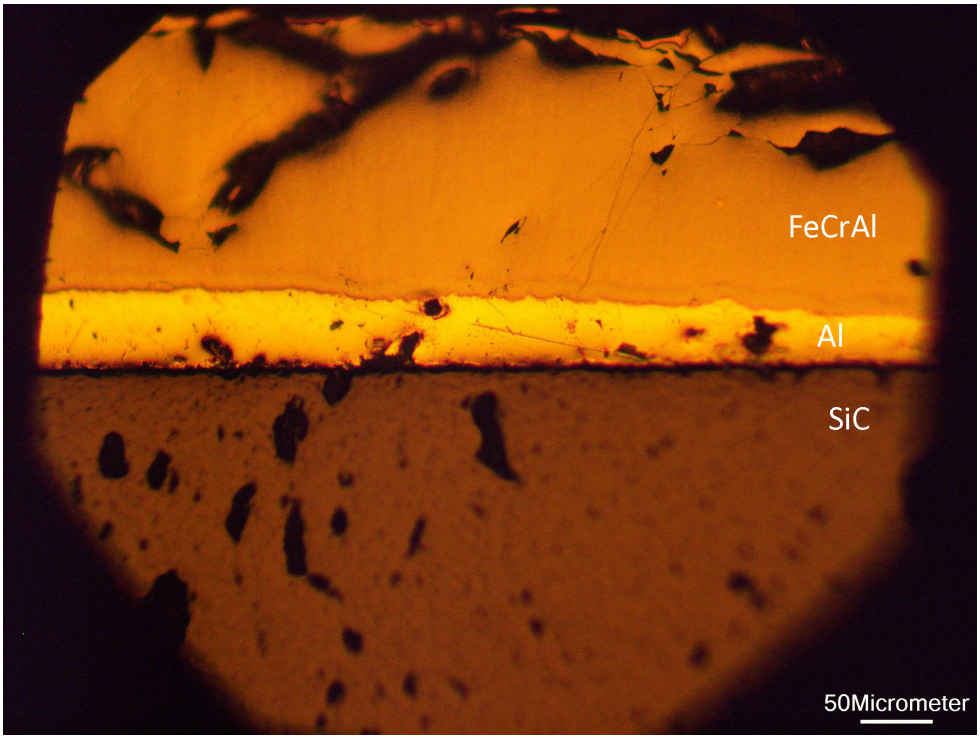


Figure A.13: Optical Micrograph of Diffusion Bonded Sample 9

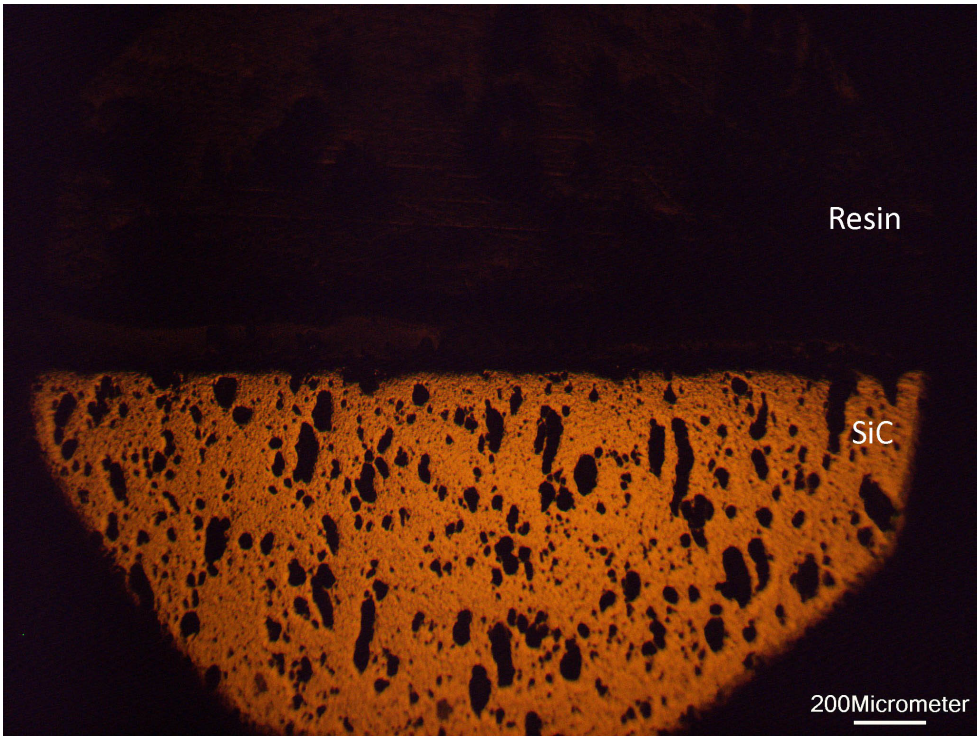


Figure A.14: Optical Micrograph of Diffusion Bonded Sample 10

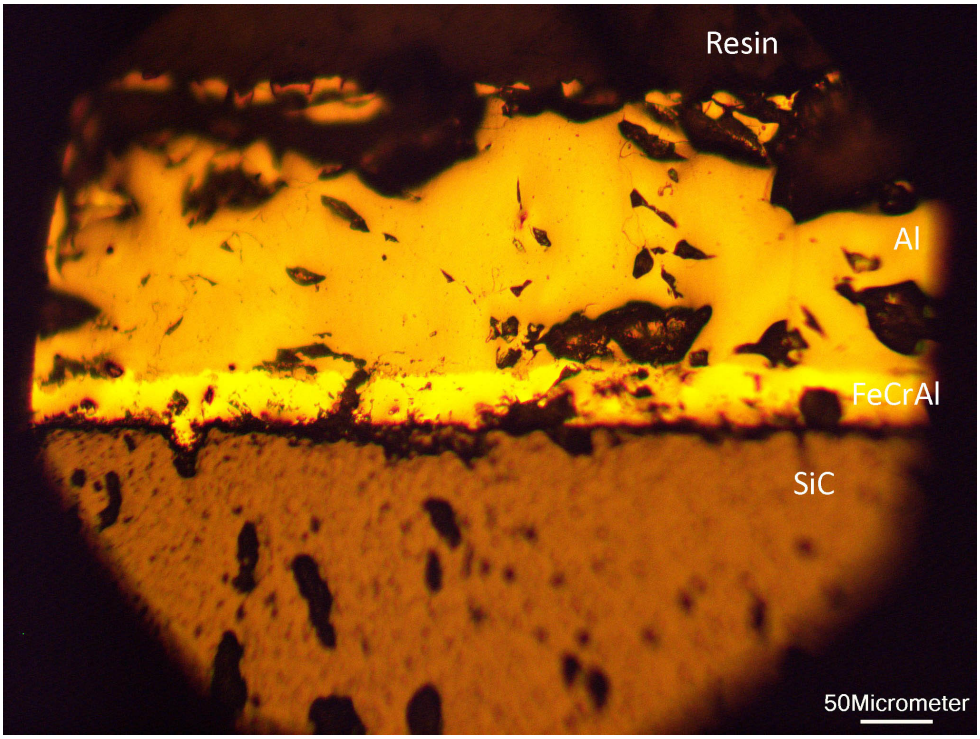


Figure A.15: Optical Micrograph of Diffusion Bonded Sample 11

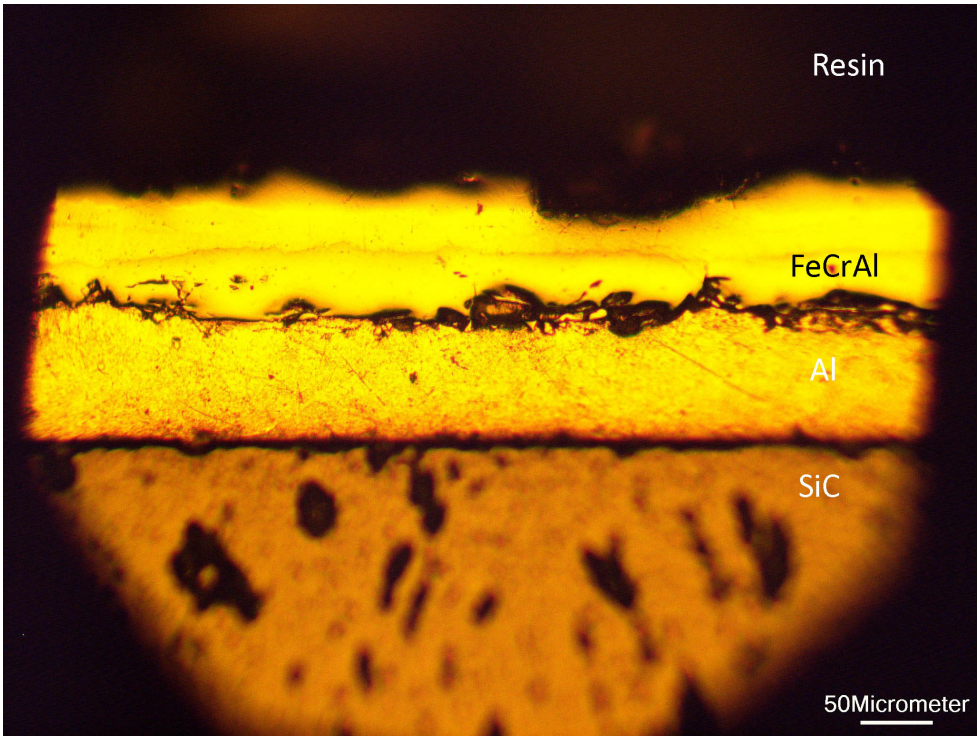


Figure A.16: Optical Micrograph of Diffusion Bonded Sample 12

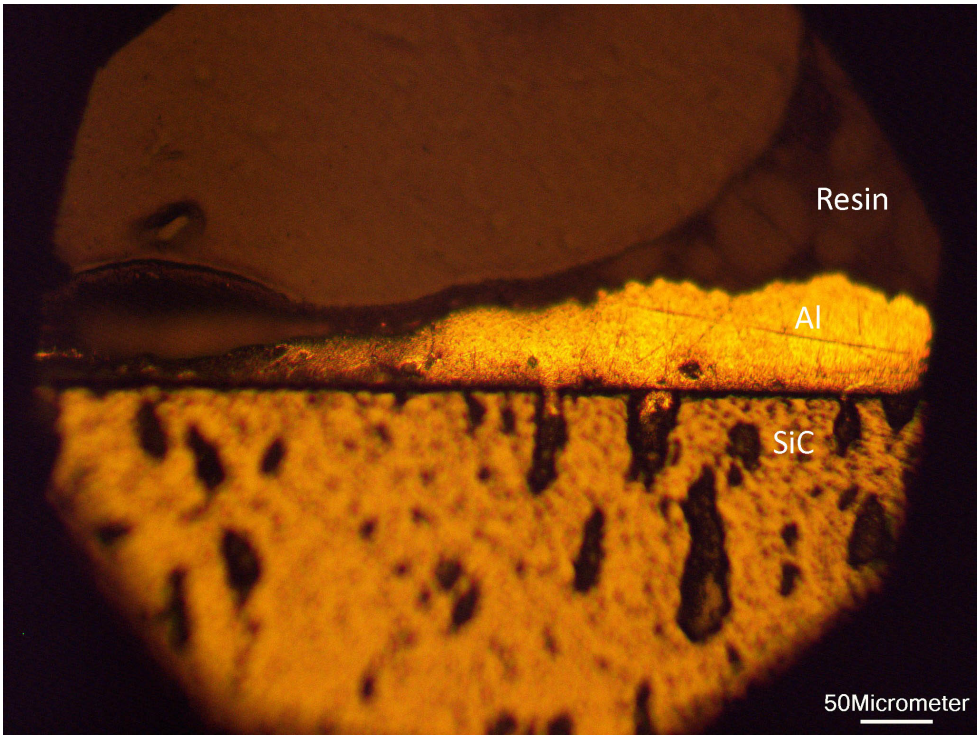


Figure A.17: Optical Micrograph of Diffusion Bonded Sample 13

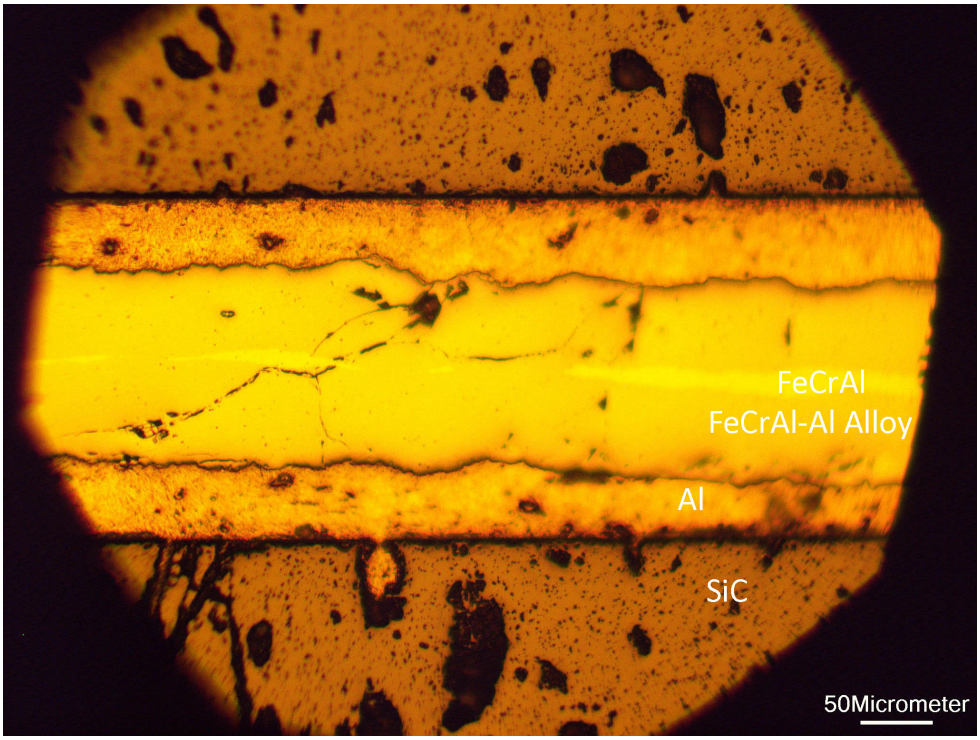


Figure A.18: Optical Micrograph of Diffusion Bonded Sample 14

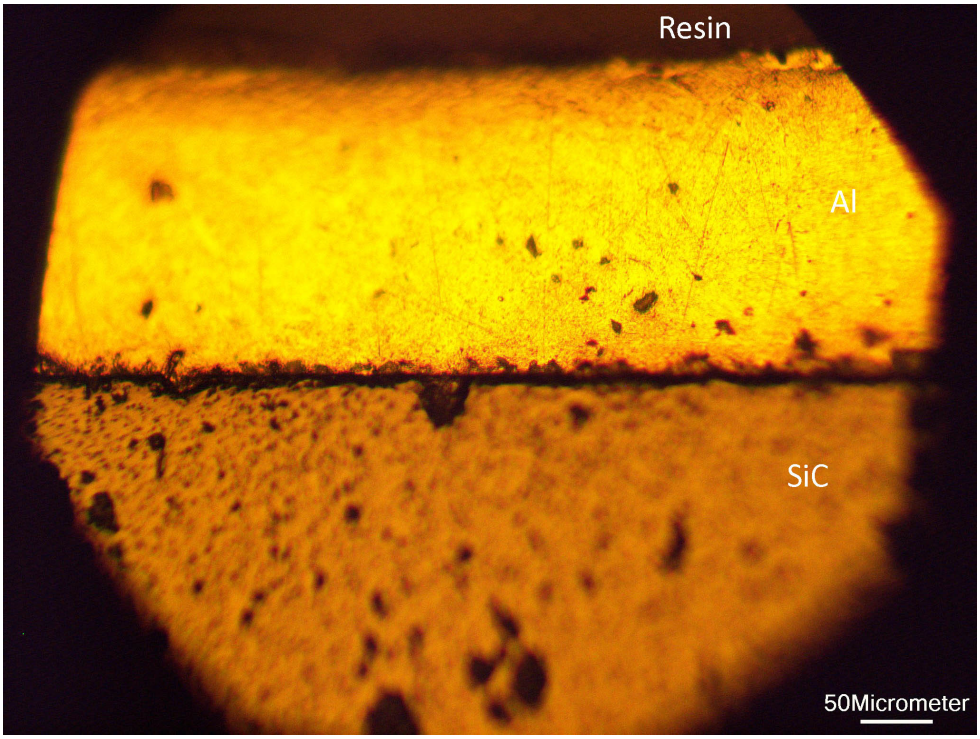


Figure A.19: Optical Micrograph of Diffusion Bonded Sample 15

# Appendix B

# Thick Film Coating Results

The operating parameters for the aluminum dip coating and casting experiments are shown in Table 3.2. Bonding is characterized by optical and/or SEM microscopy.

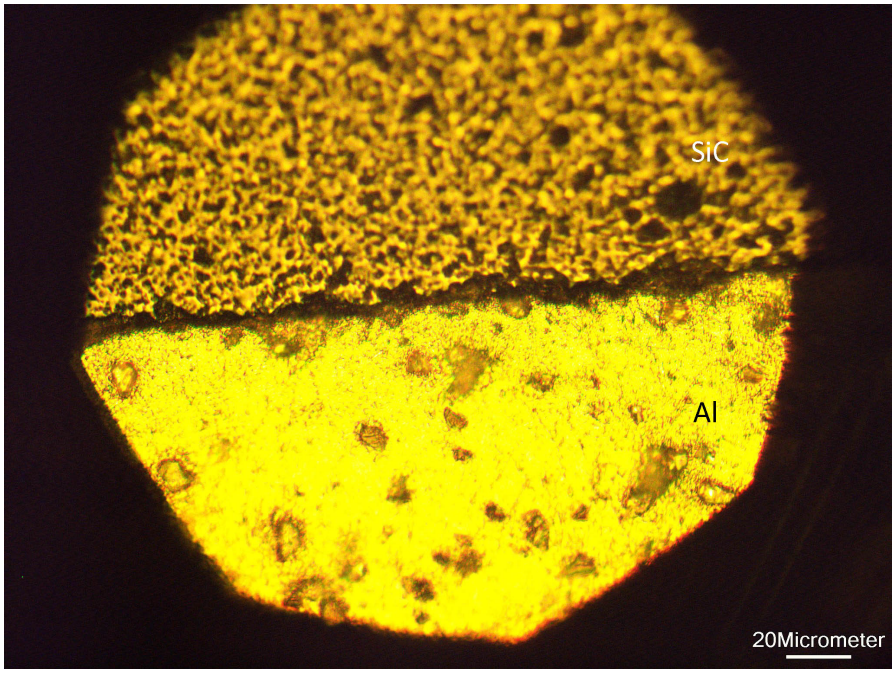


Figure B.1: Optical Micrograph of Al-Dip Coated Sample 1

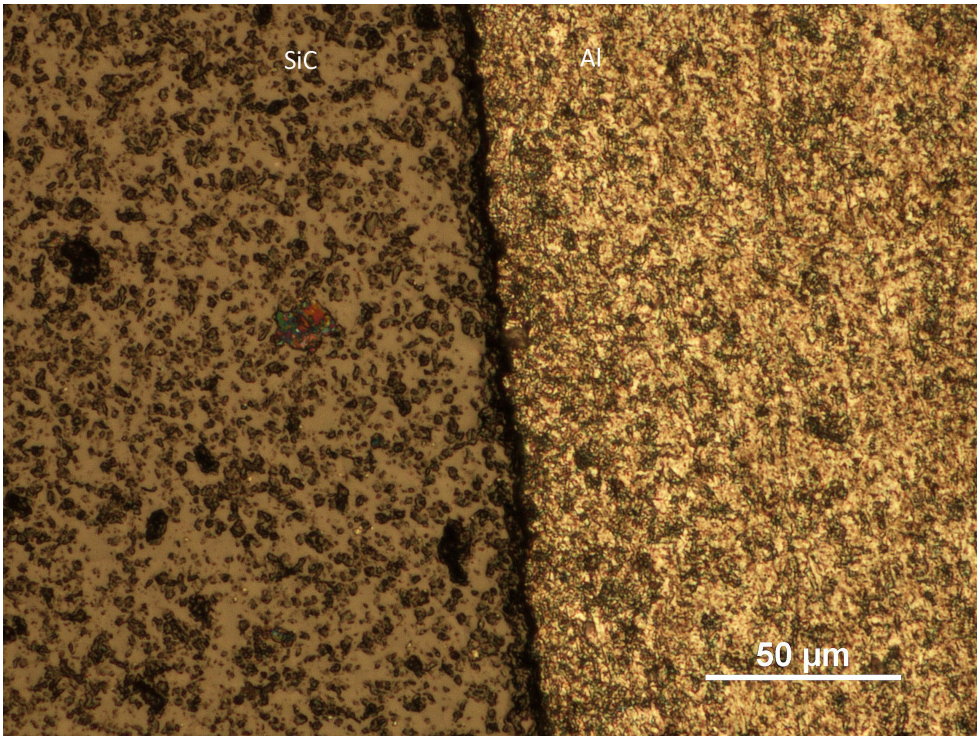


Figure B.2: Optical Micrograph of Al-Casted Sample 5

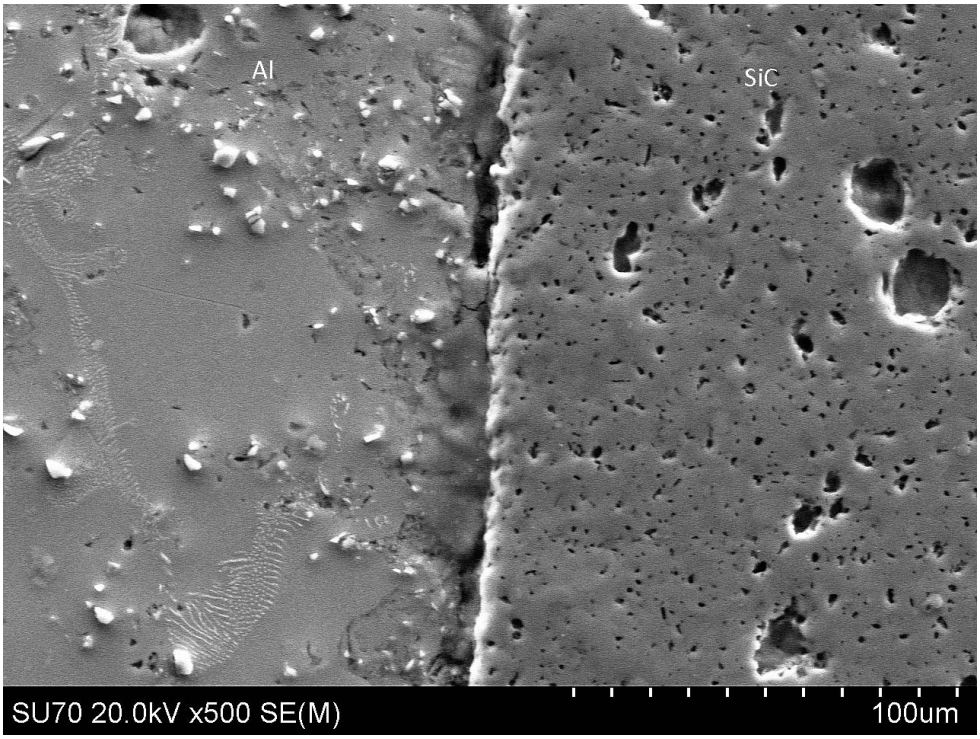


Figure B.3: SEM Image of Al-Casted Sample 5

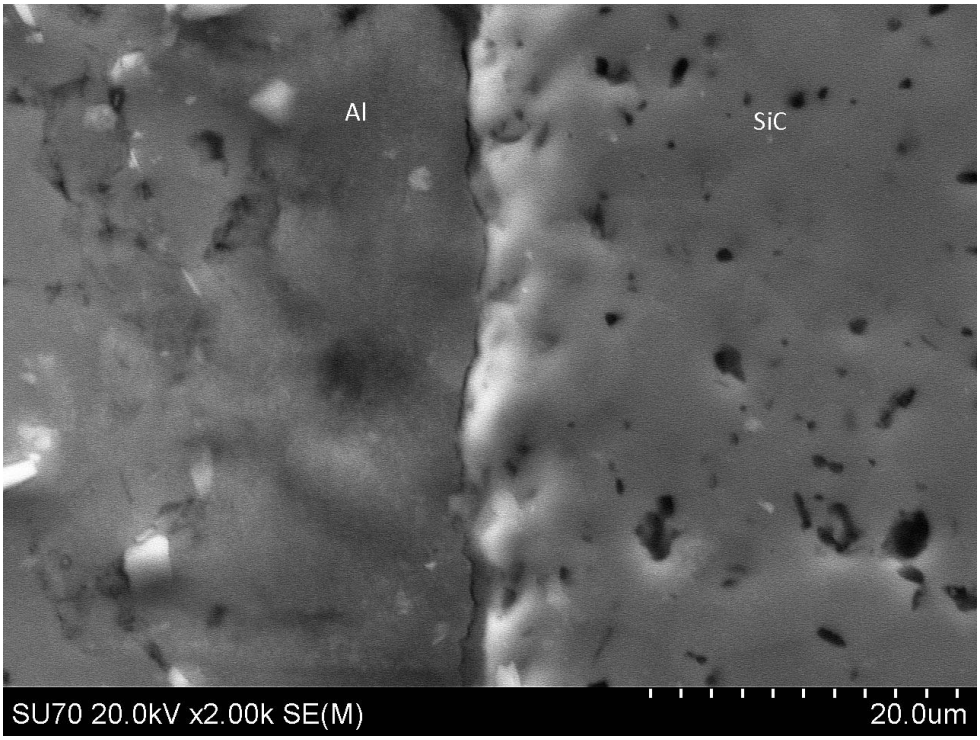


Figure B.4: SEM Image of Al-Casted Sample 5

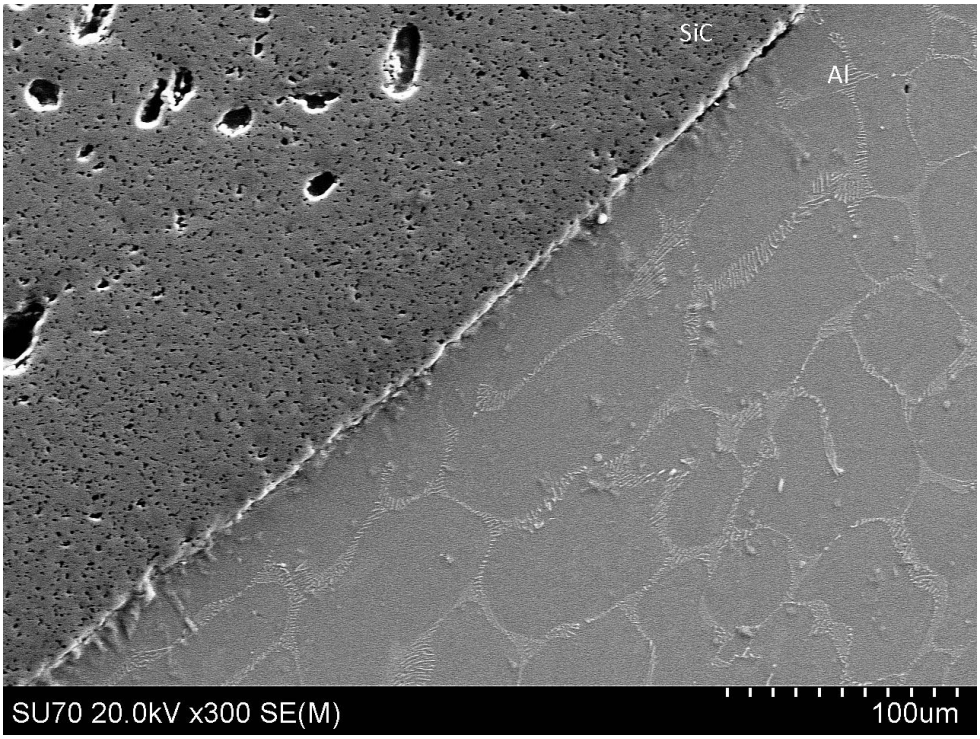


Figure B.5: SEM Image of Al-Casted Sample 6

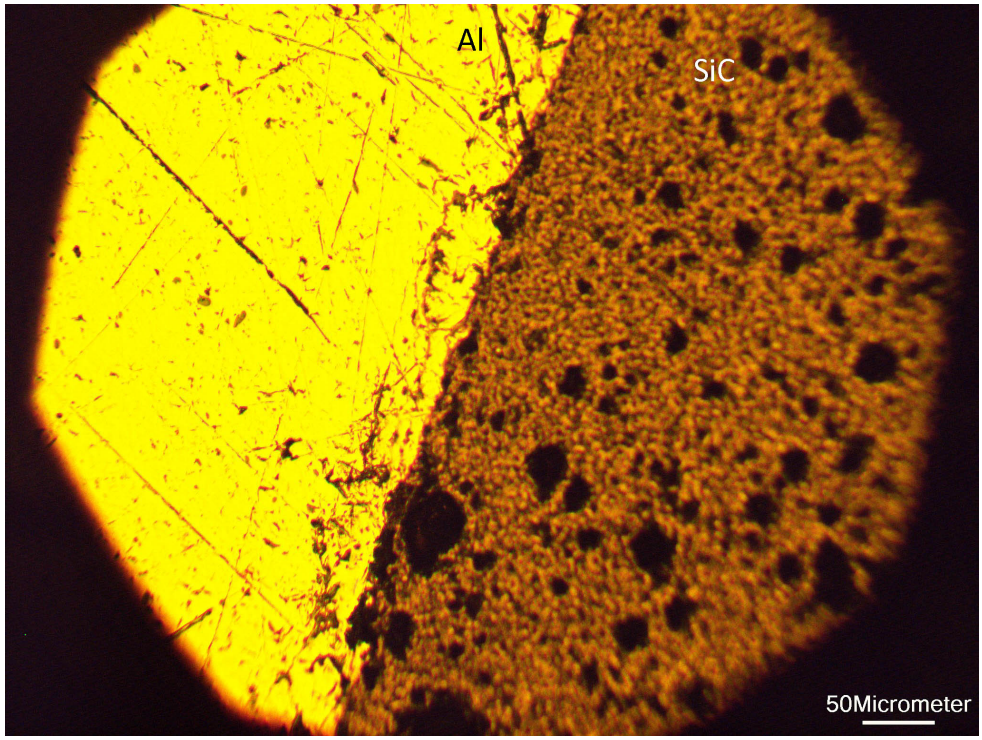


Figure B.6: Optical Micrograph of Al-Casted Sample 7

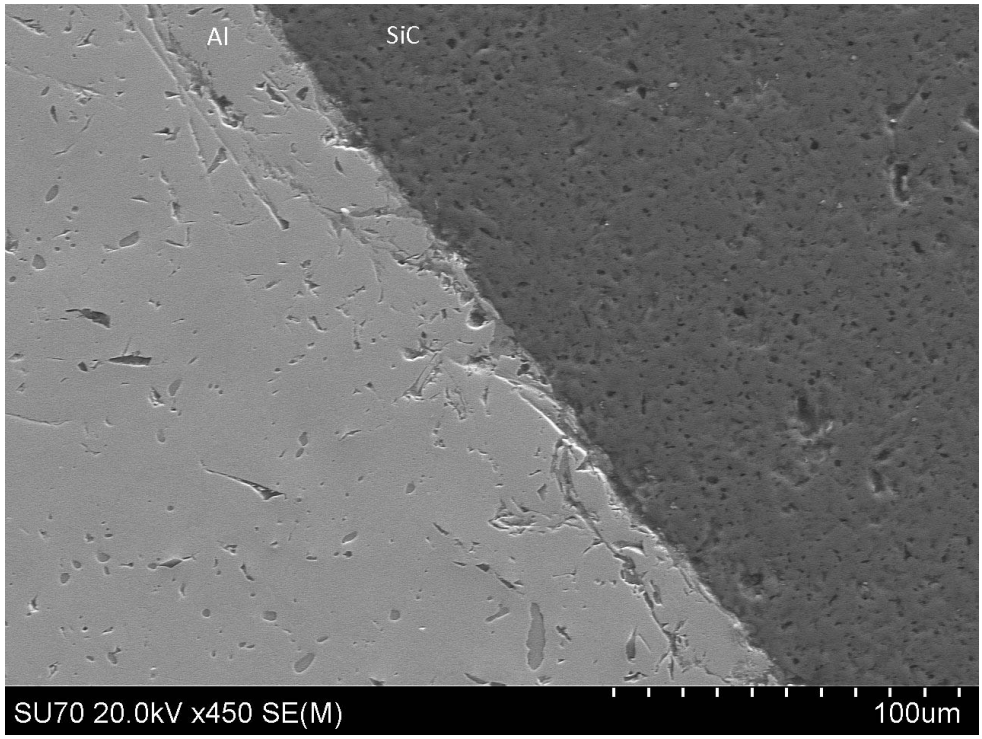


Figure B.7: SEM Image of Al-Casted Sample 7

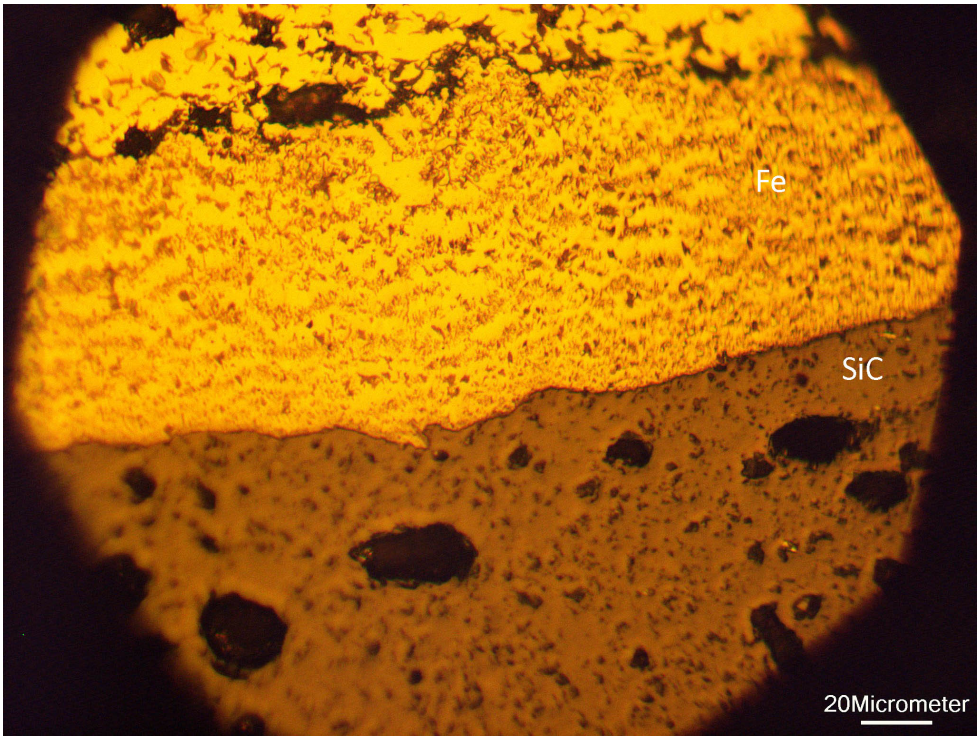


Figure B.8: Optical Micrograph of Al-Casted Sample 8

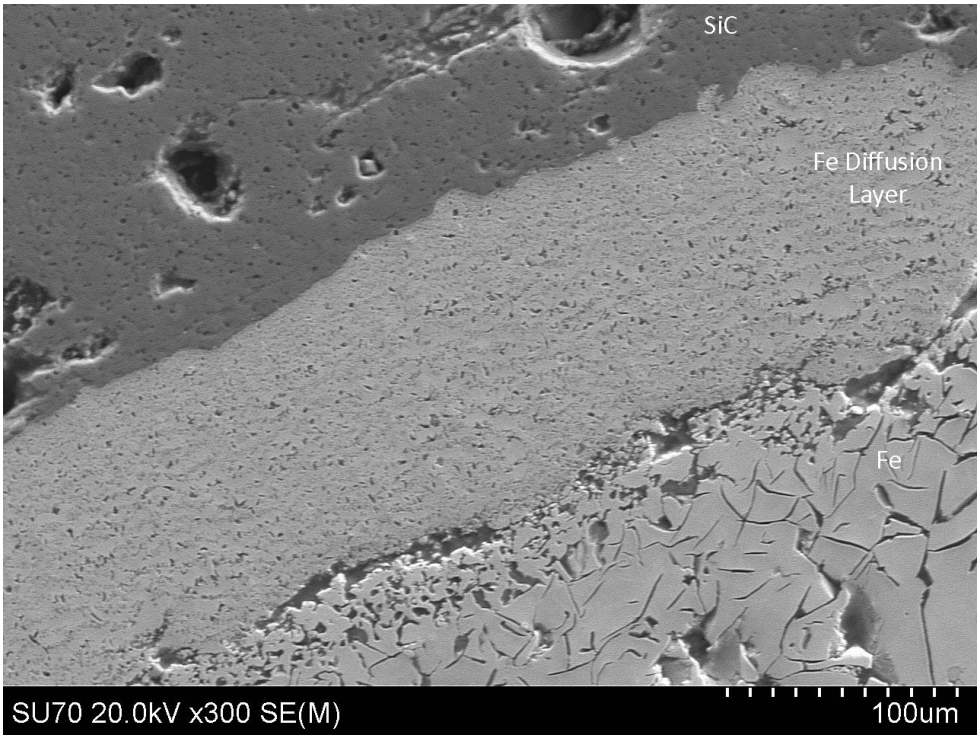


Figure B.9: SEM Image of Al-Casted Sample 8

# Appendix C

# Thin Film Coatings Results

The operating parameters for thin film deposition by methods of magnetron sputtering and electron beam evaporation are shown in Table 3.3 and Table 3.4, respectively. Bonding is characterized by optical and/or SEM microscopy.

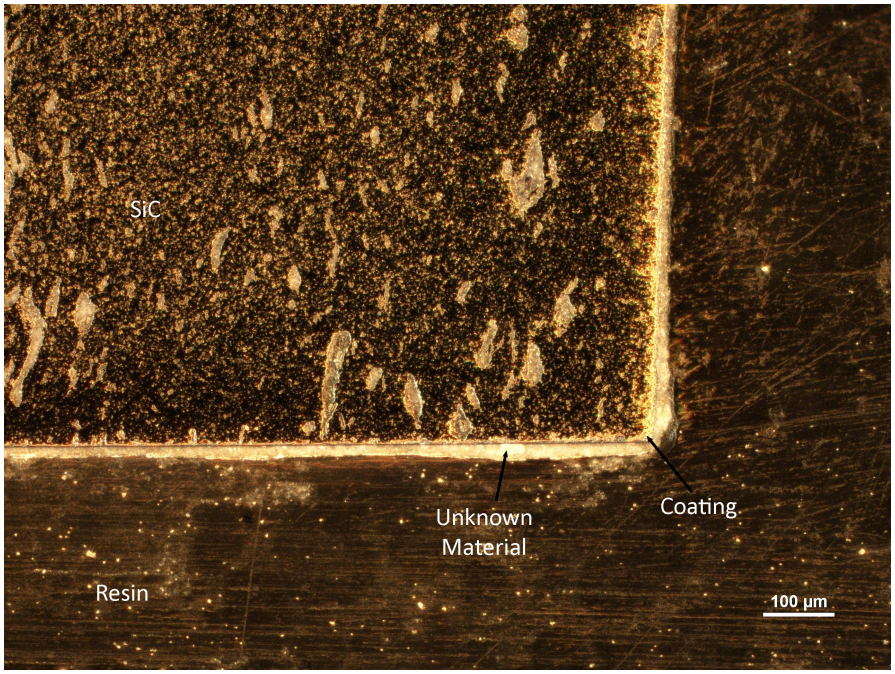


Figure C.1: DF Optical Micrograph of Al Sputtered Sample 3

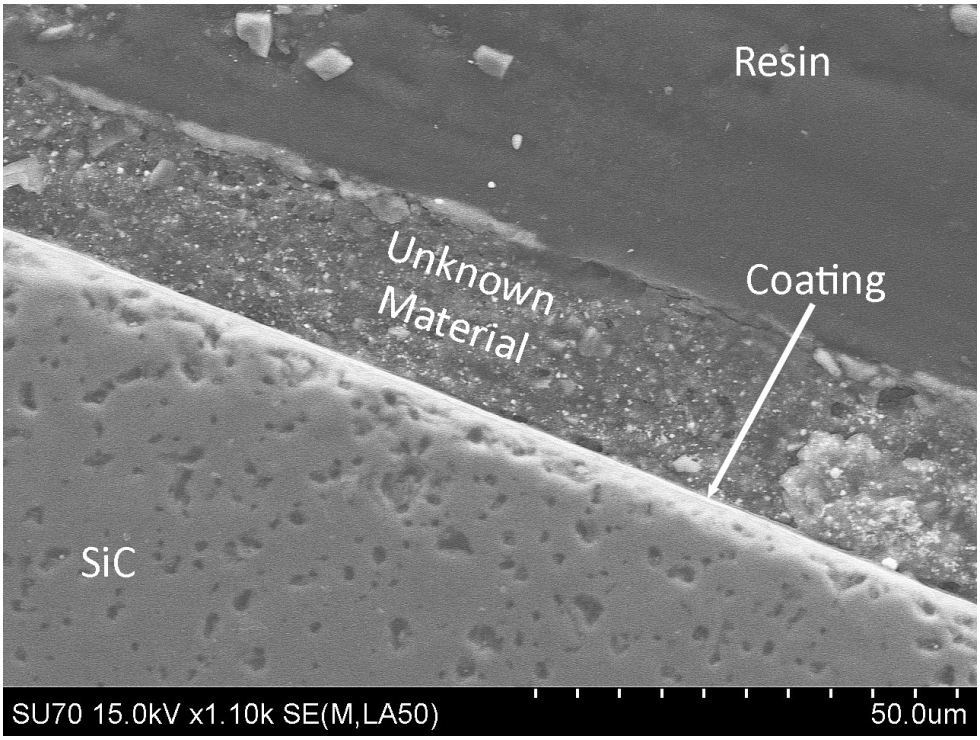


Figure C.2: SEM Image of Al Sputtered Sample 3

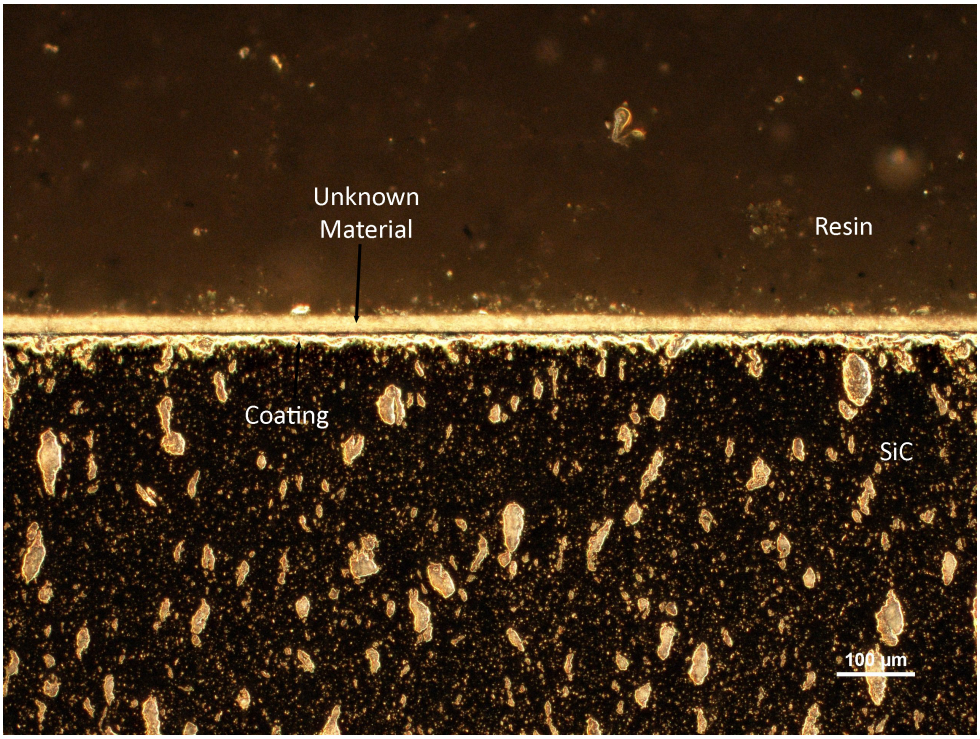


Figure C.3: DF Optical Micrograph of Al Sputtered Sample 4

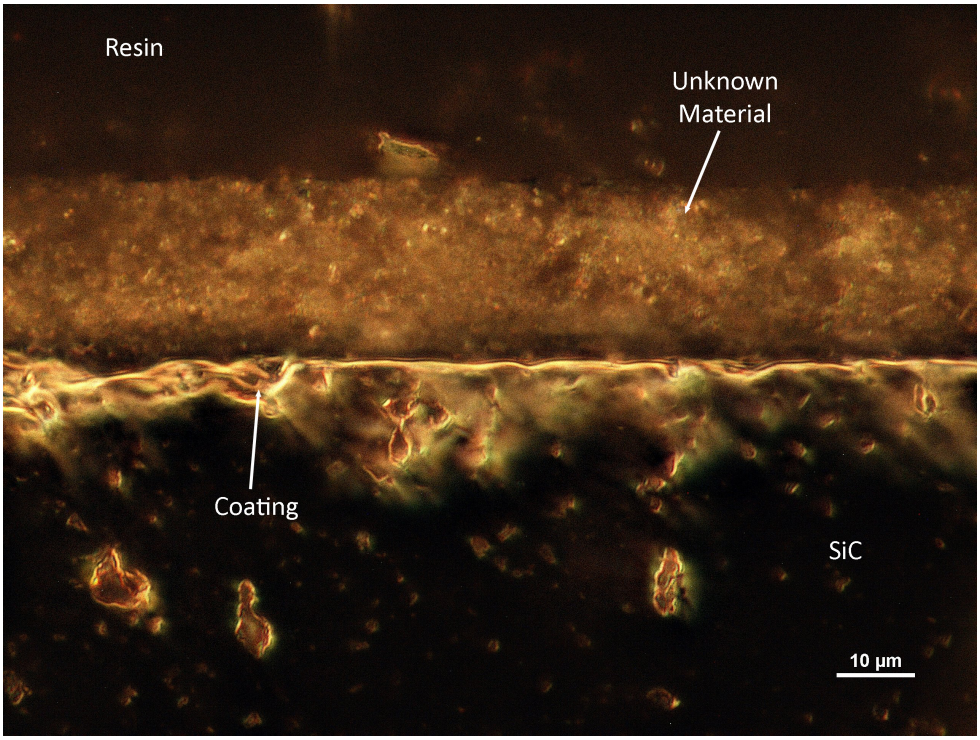


Figure C.4: DF Optical Micrograph of Al Sputtered Sample 4

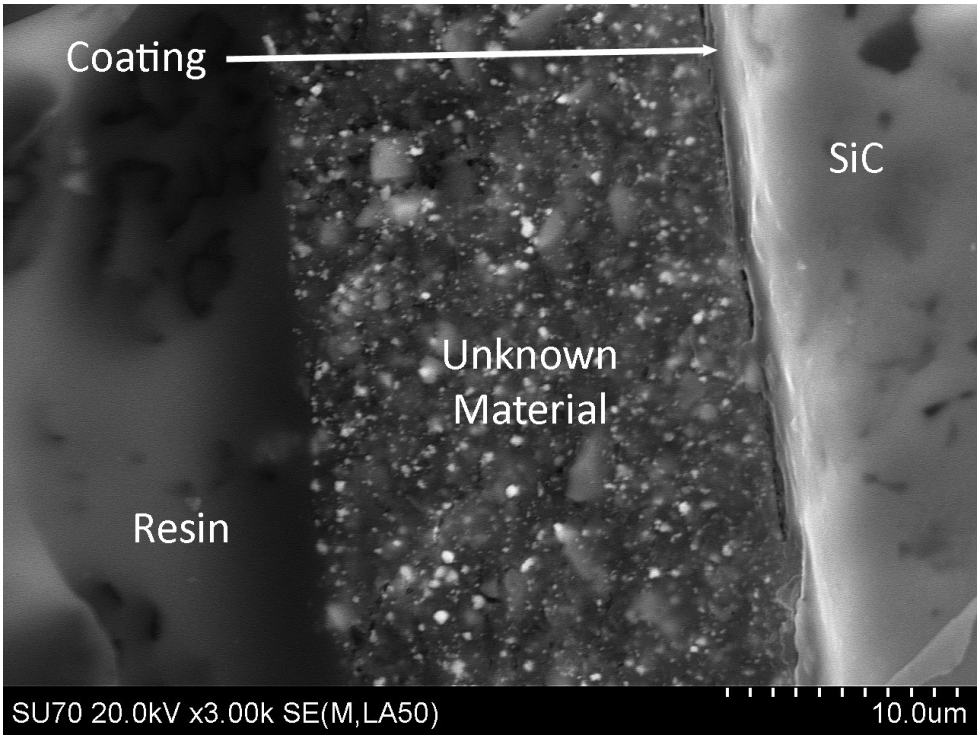


Figure C.5: SEM Image of Al Sputtered Sample 4

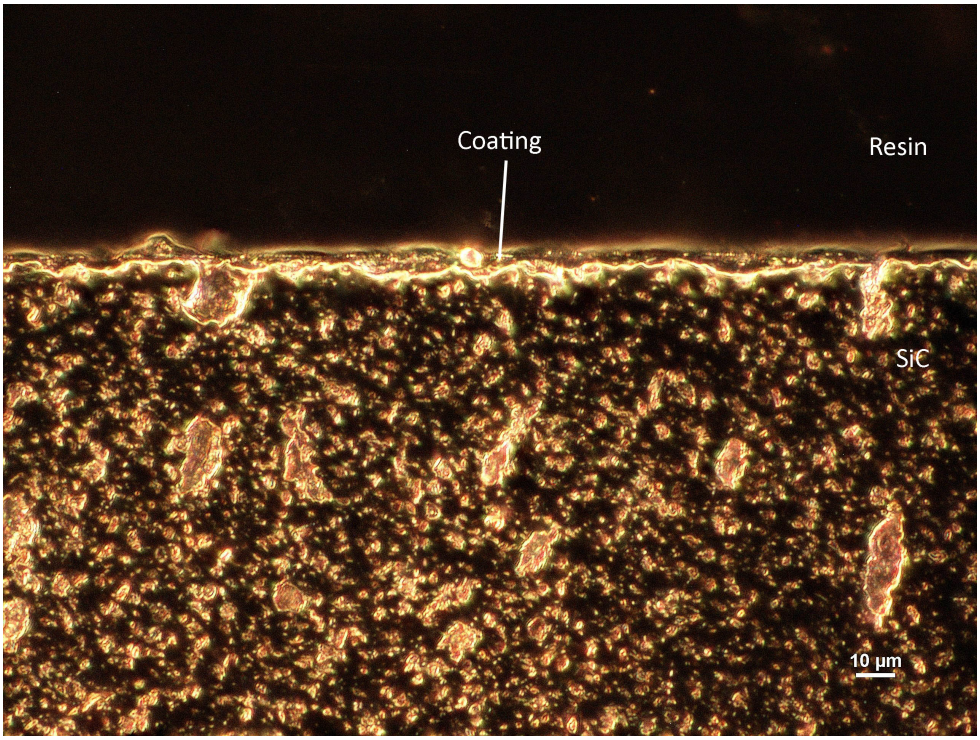


Figure C.6: DF Optical Micrograph of HT Cr Evaporated Sample 2

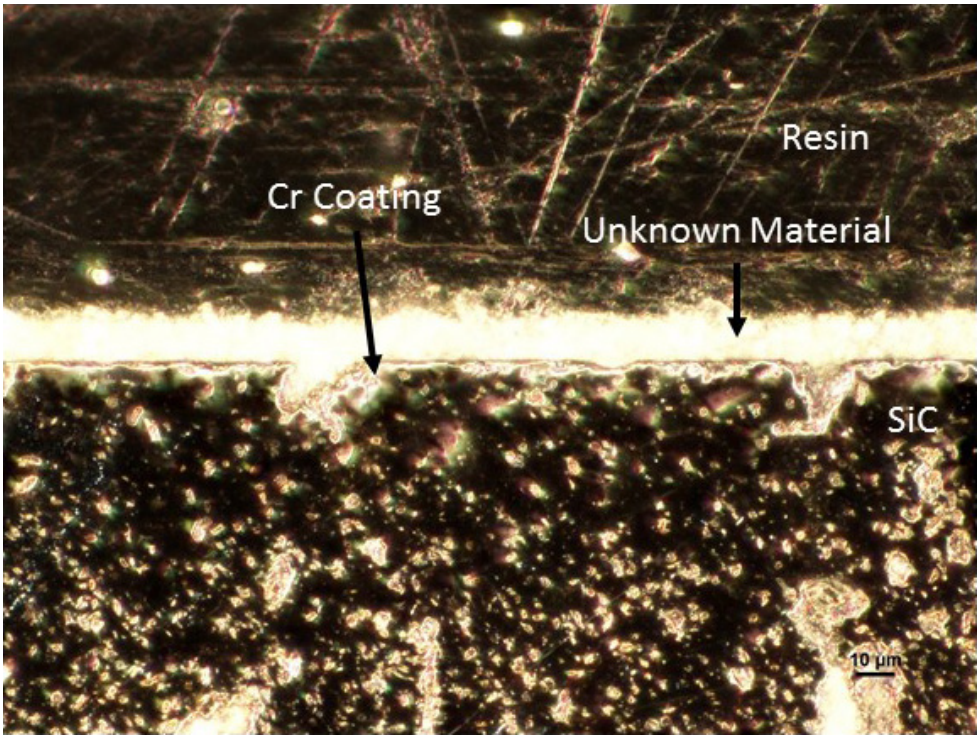


Figure C.7: DF Optical Micrograph of Non-HT Cr Evaporated Sample 3

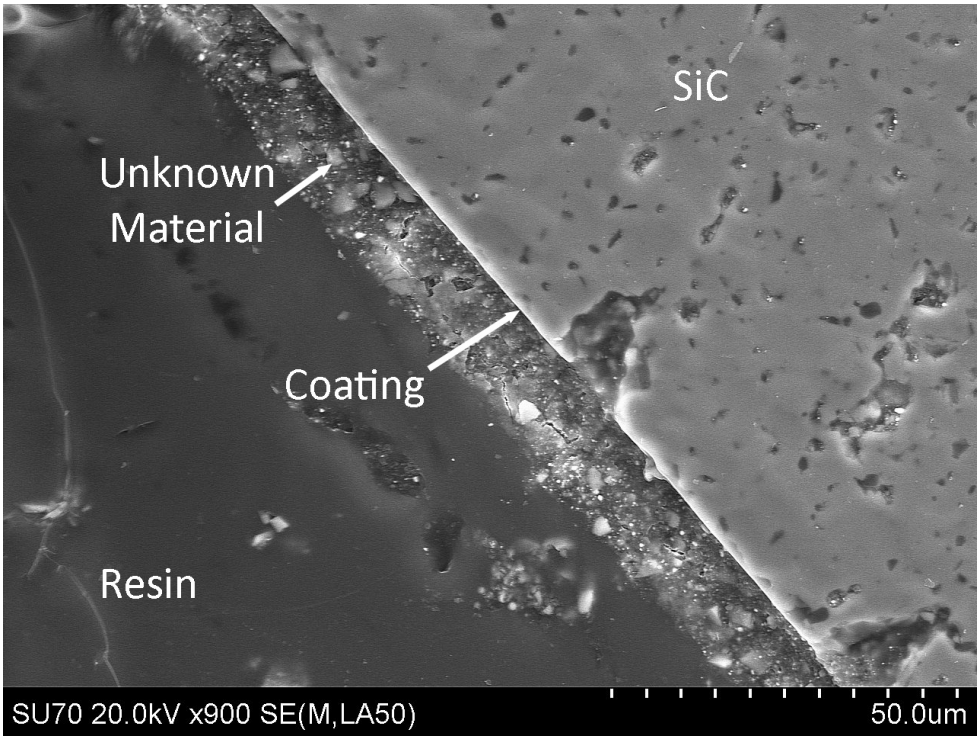


Figure C.8: SEM Image of Non-HT Cr Evaporated Sample 3

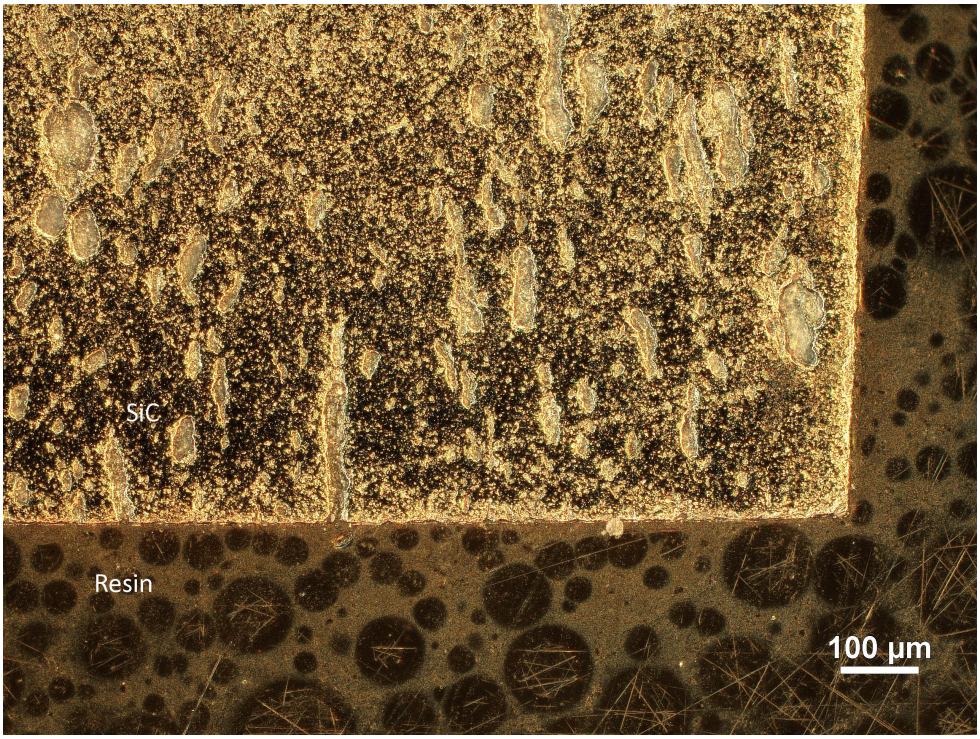


Figure C.9: DF Optical Micrograph of HT Cr/Fe/Al Evaporated Sample 4

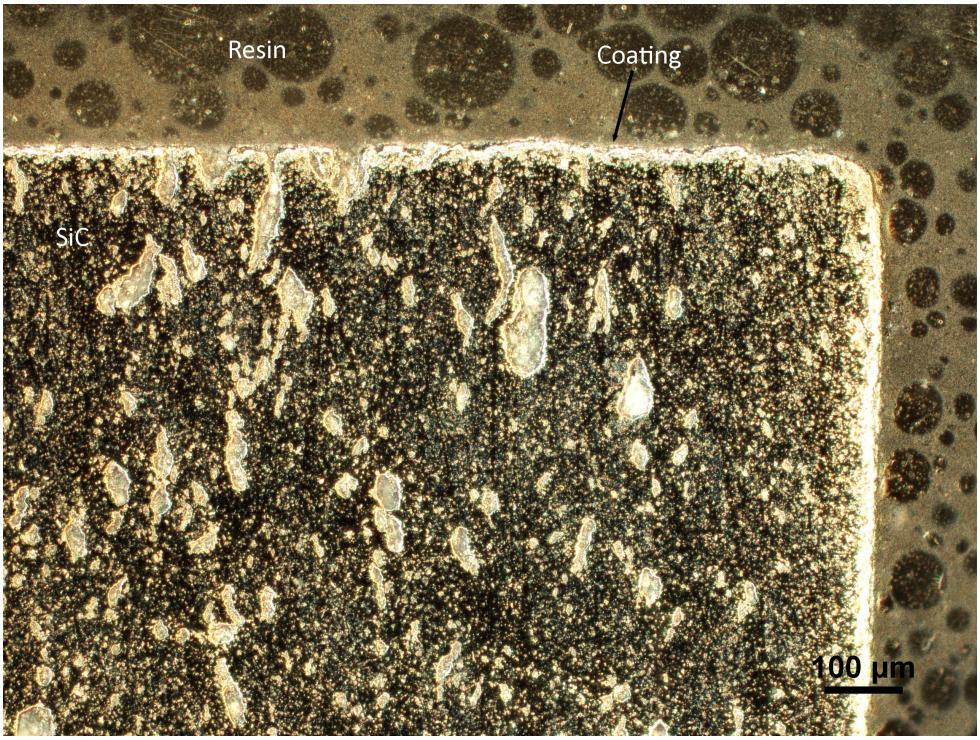


Figure C.10: DF Optical Micrograph of Non-HT Cr/Fe/Al Evaporated Sample 5

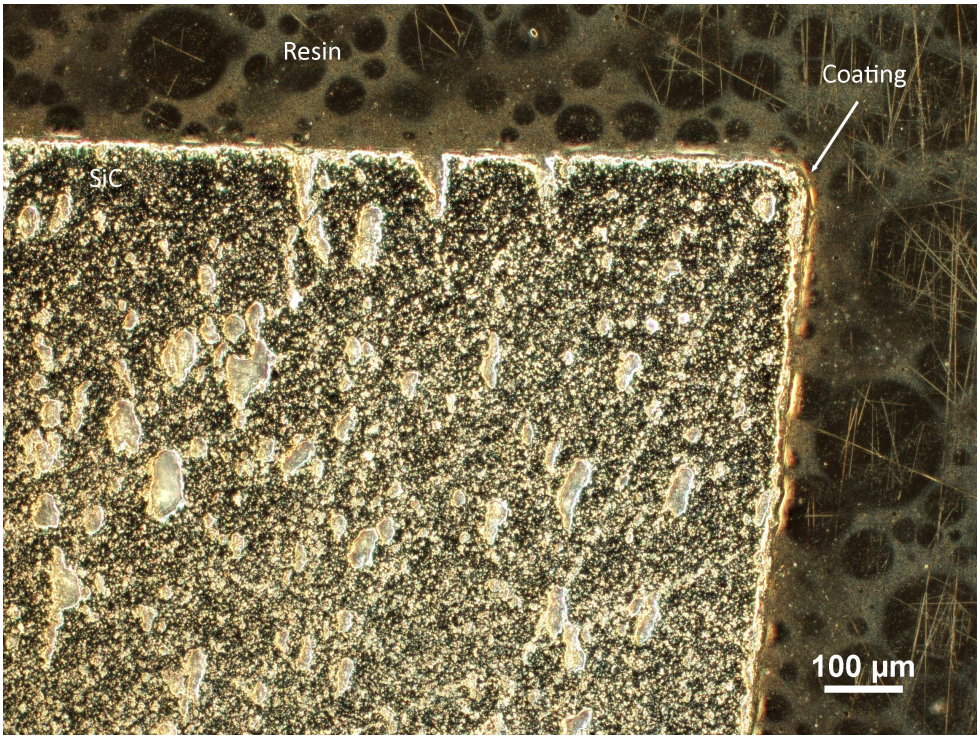


Figure C.11: DF Optical Micrograph of HT Cr/Fe Evaporated Sample 6

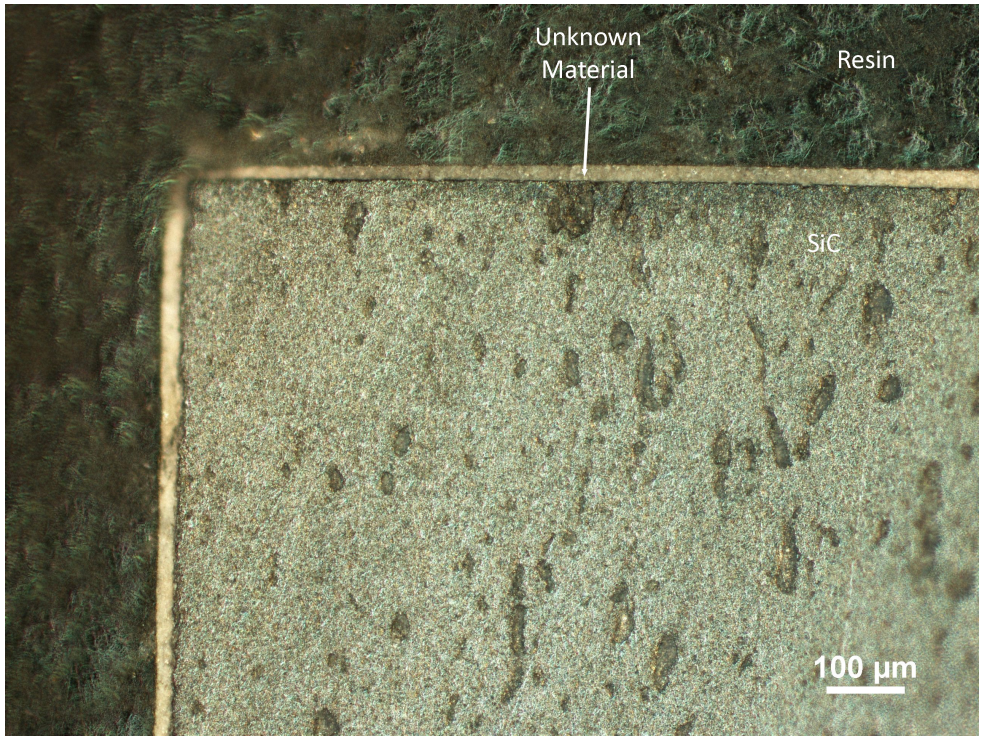


Figure C.12: DF Optical Micrograph of Non-HT Cr/Fe Evaporated Sample 7

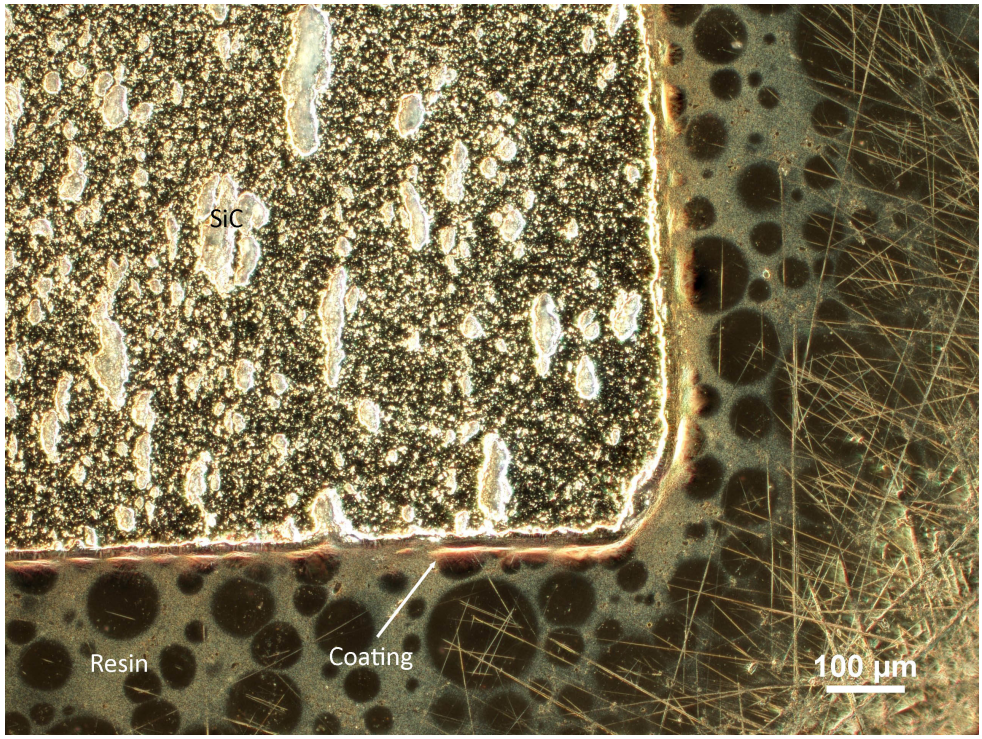


Figure C.13: DF Optical Micrograph of HT Cr/Al Evaporated Sample 8

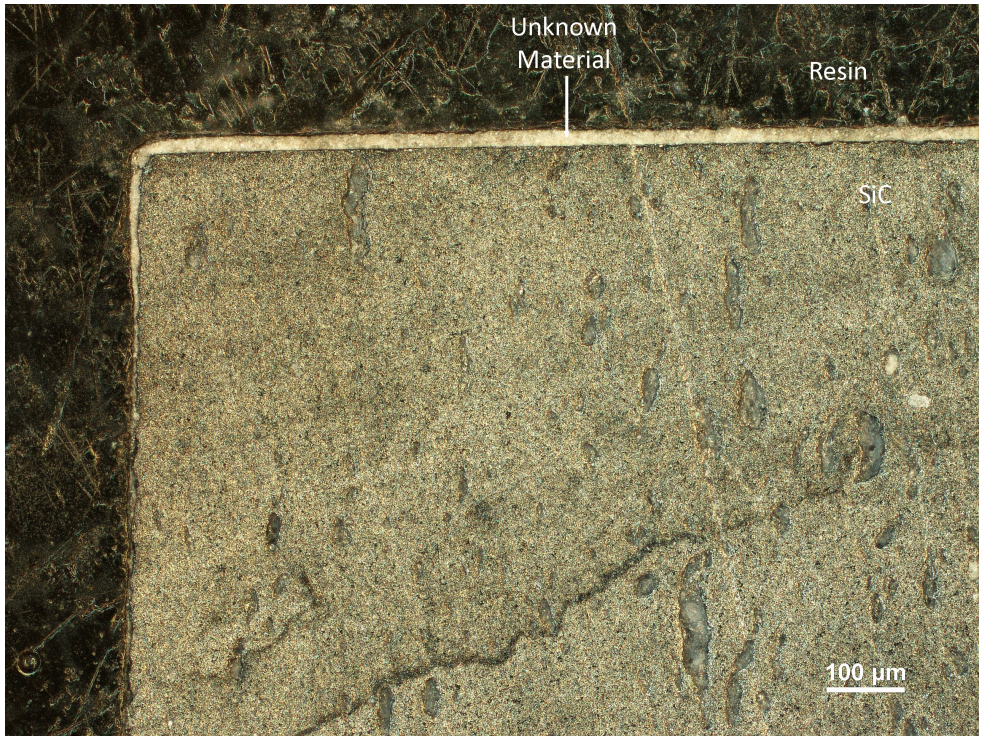


Figure C.14: DF Optical Micrograph of Non-HT Cr/Al Evaporated Sample 9

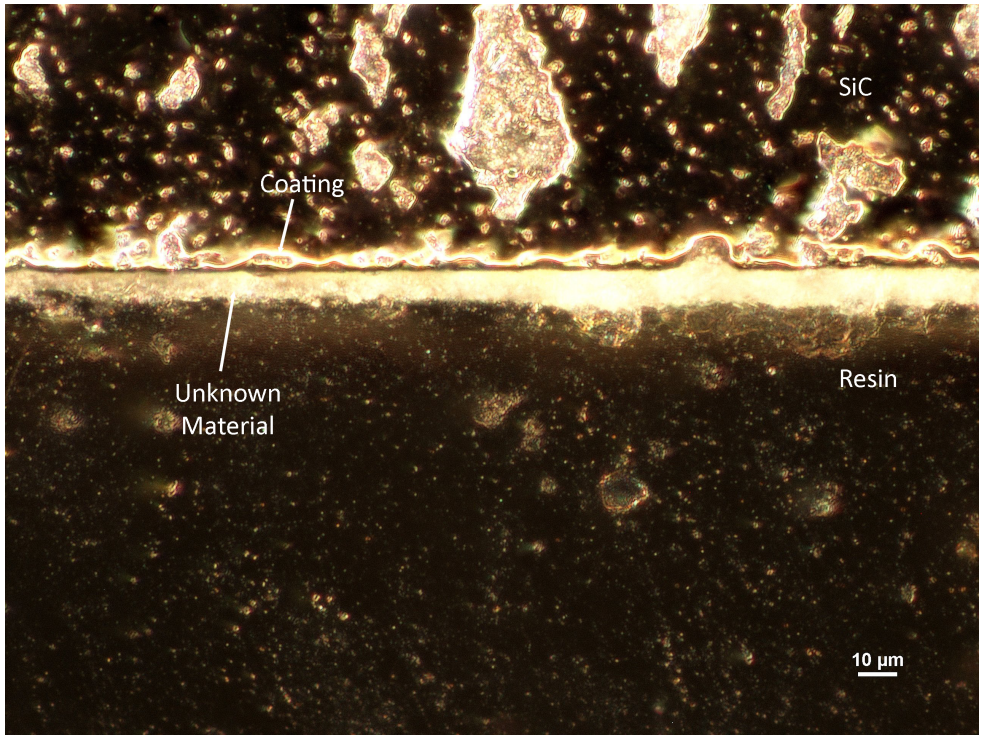


Figure C.15: DF Optical Micrograph of HT Cr/Fe/Al Evaporated Sample 10

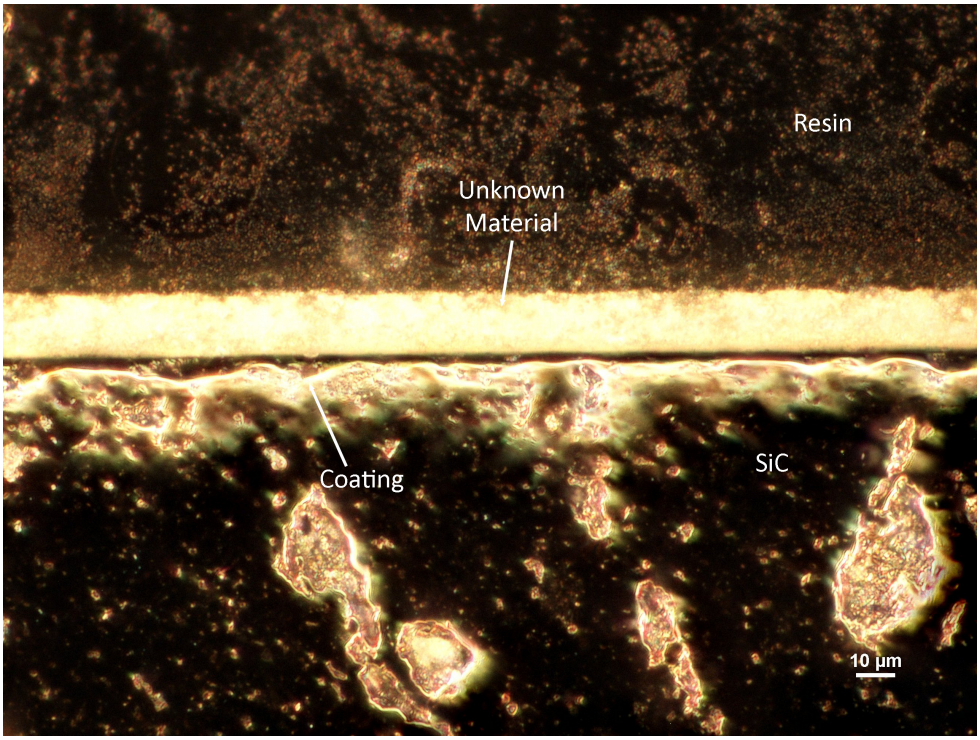


Figure C.16: DF Optical Micrograph of Non-HT Cr/Al Evaporated Sample 11

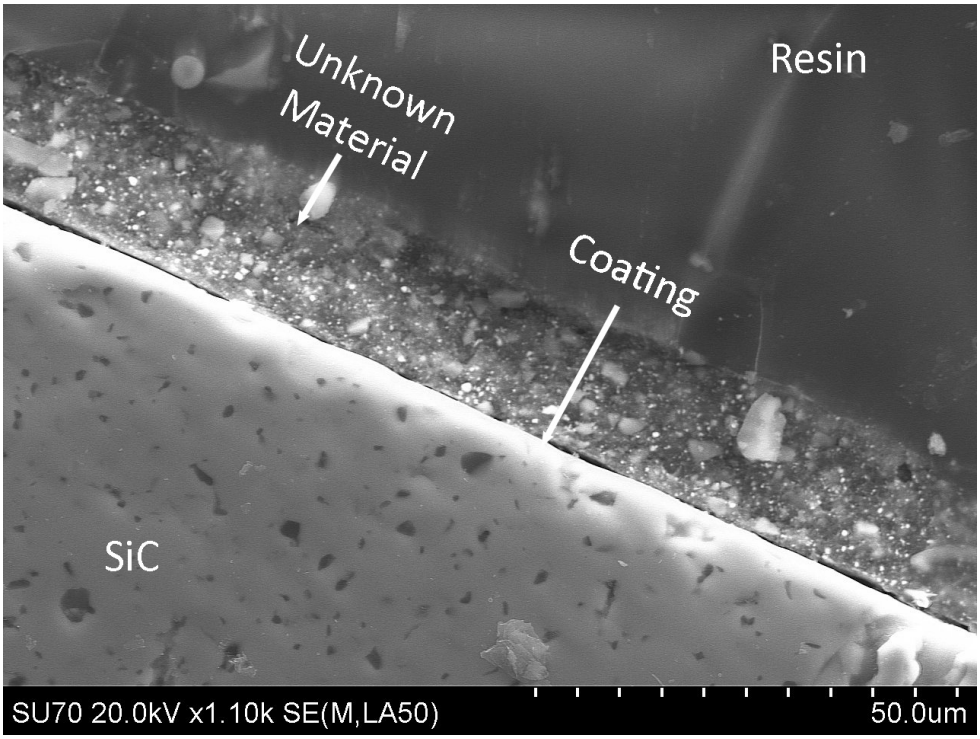


Figure C.17: SEM Image of Non-HT Cr/Al Evaporated Sample 11

# Appendix D

# High-Temperature Diffusion Bonding Results

The operating parameters for the HT diffusion bonding experiments are shown in Table 3.5. Bonding between FeCrAl and SiC are qualitatively characterized by optical and/or SEM.

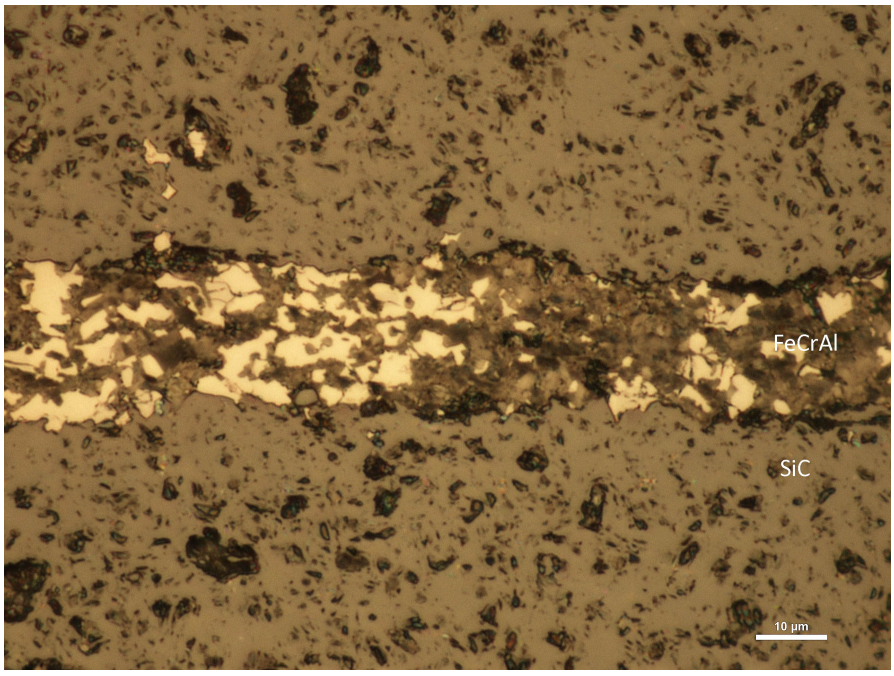


Figure D.1: Optical Micrograph of HT-Diffusion Bonded Sample 1

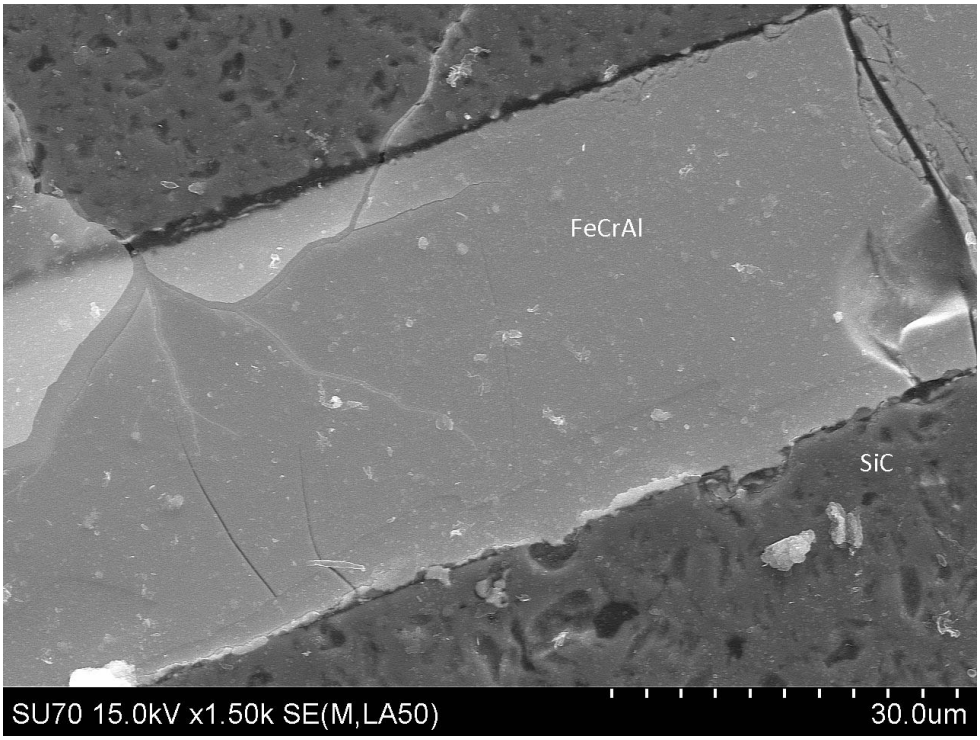


Figure D.2: SEM Image of HT-Diffusion Bonded Sample 1

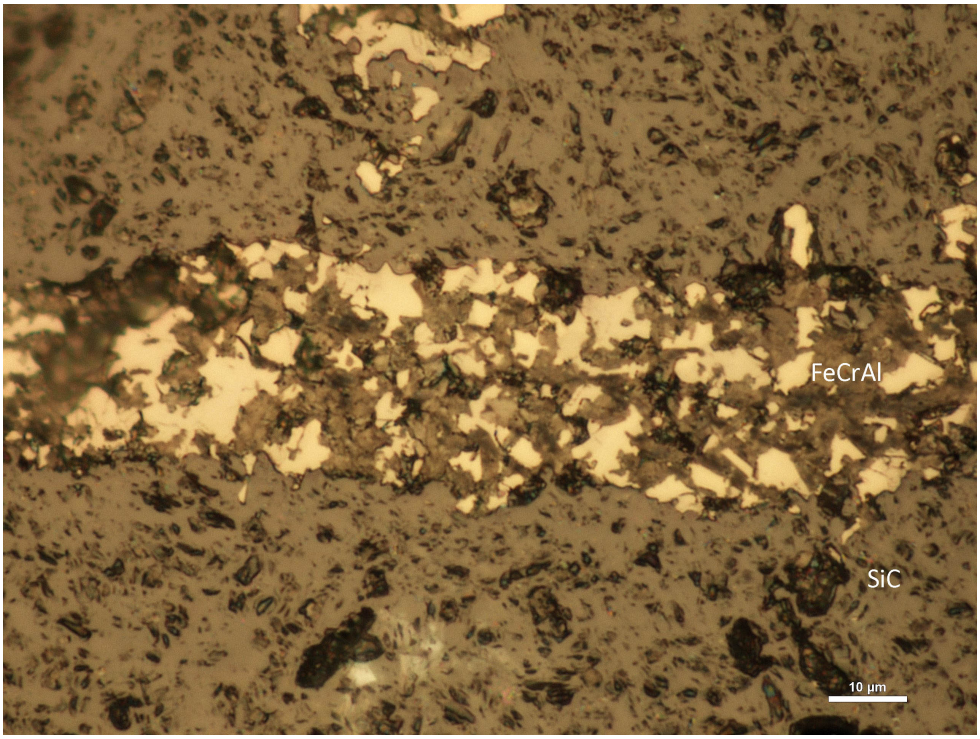


Figure D.3: Optical Micrograph of HT-Diffusion Bonded Sample 2

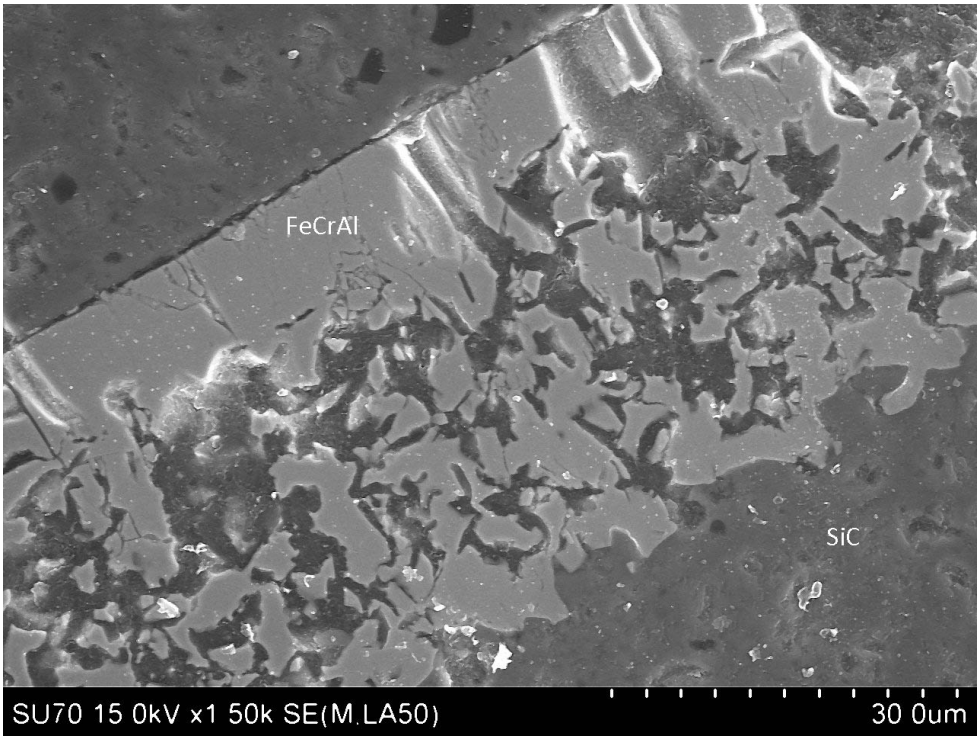


Figure D.4: SEM Image of HT-Diffusion Bonded Sample 2

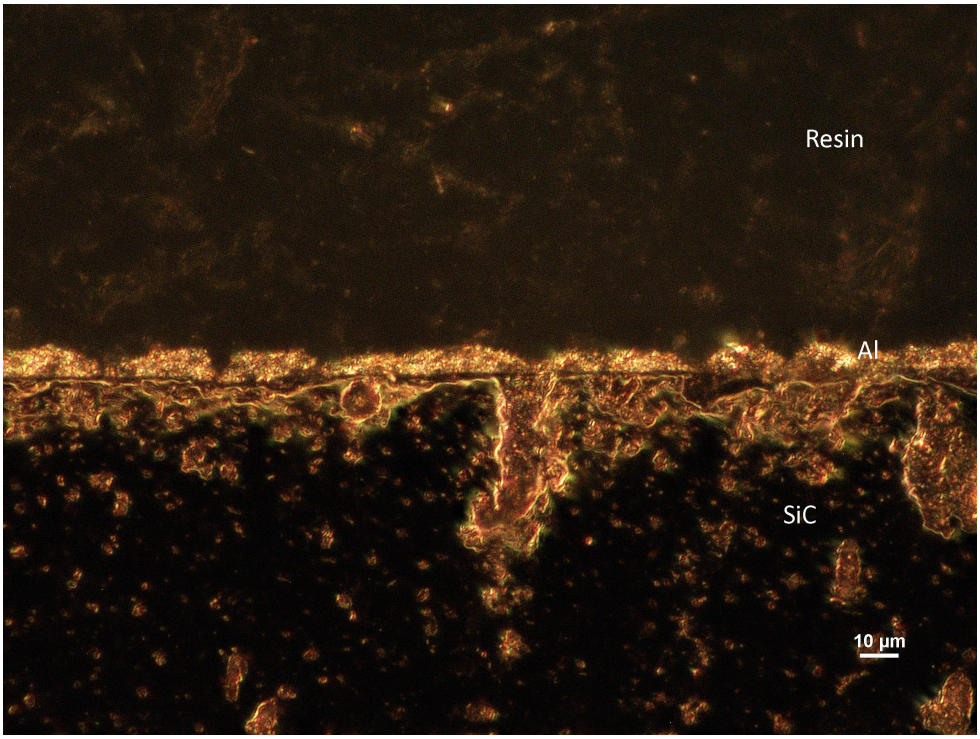


Figure D.5: Optical Micrograph of HT-Diffusion Bonded Sample 3

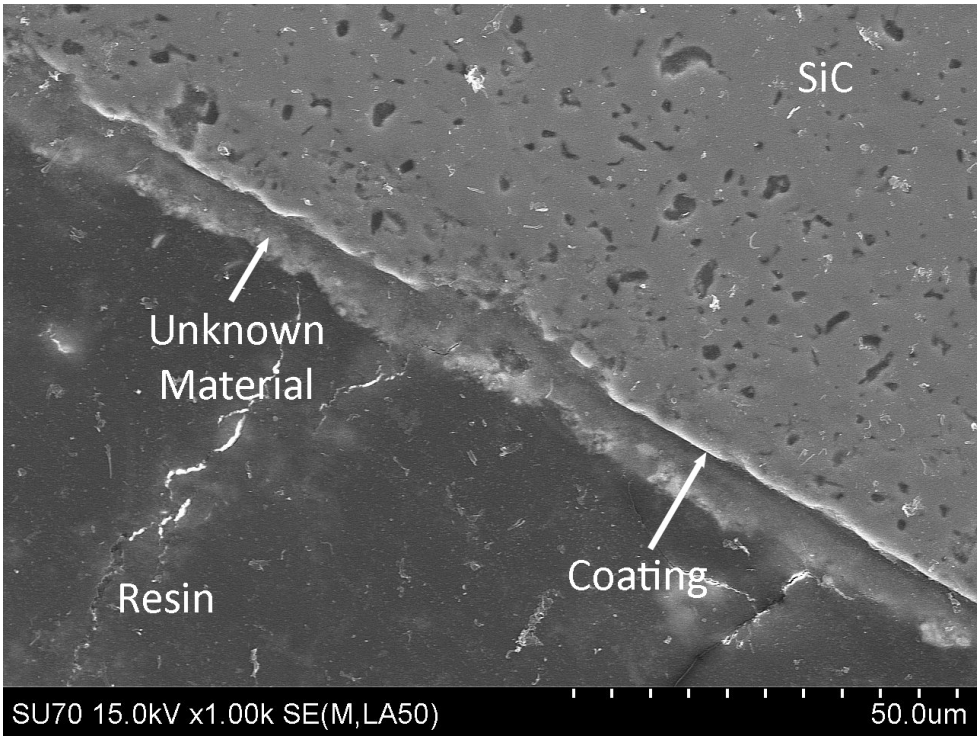


Figure D.6: SEM Image of HT-Diffusion Bonded Sample 3

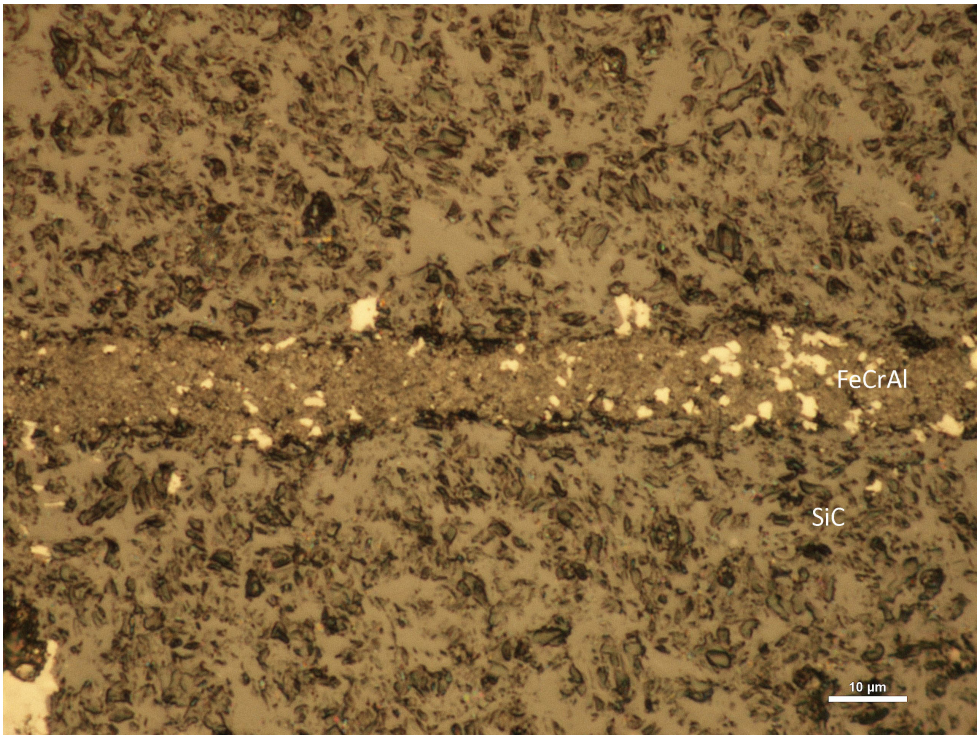


Figure D.7: Optical Micrograph of HT-Diffusion Bonded Sample 4

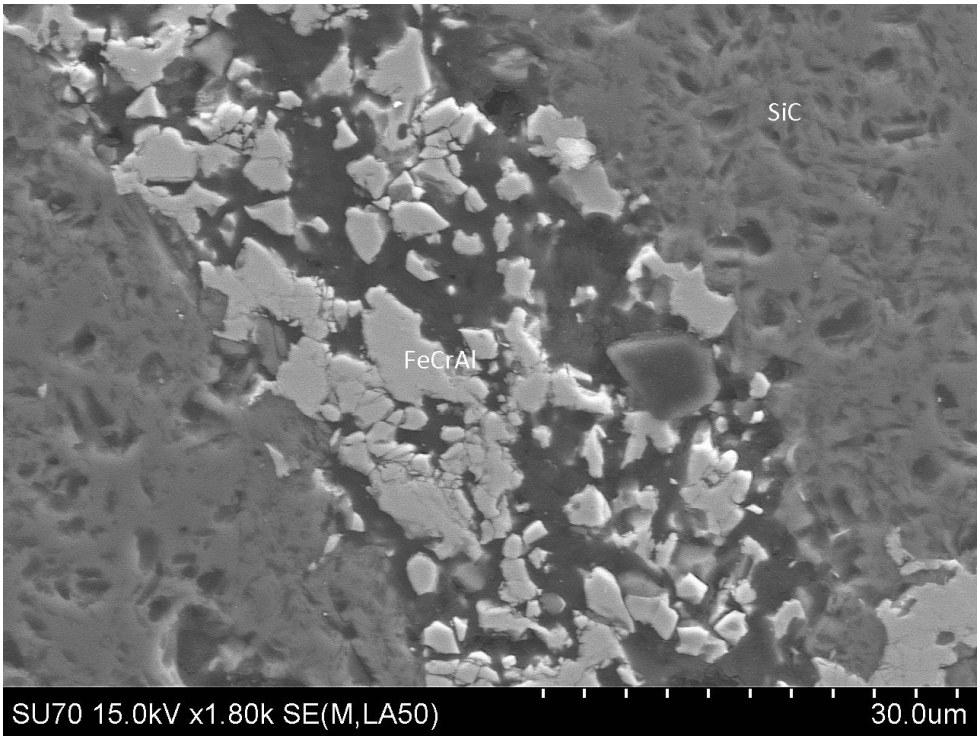


Figure D.8: SEM Image of HT-Diffusion Bonded Sample 4

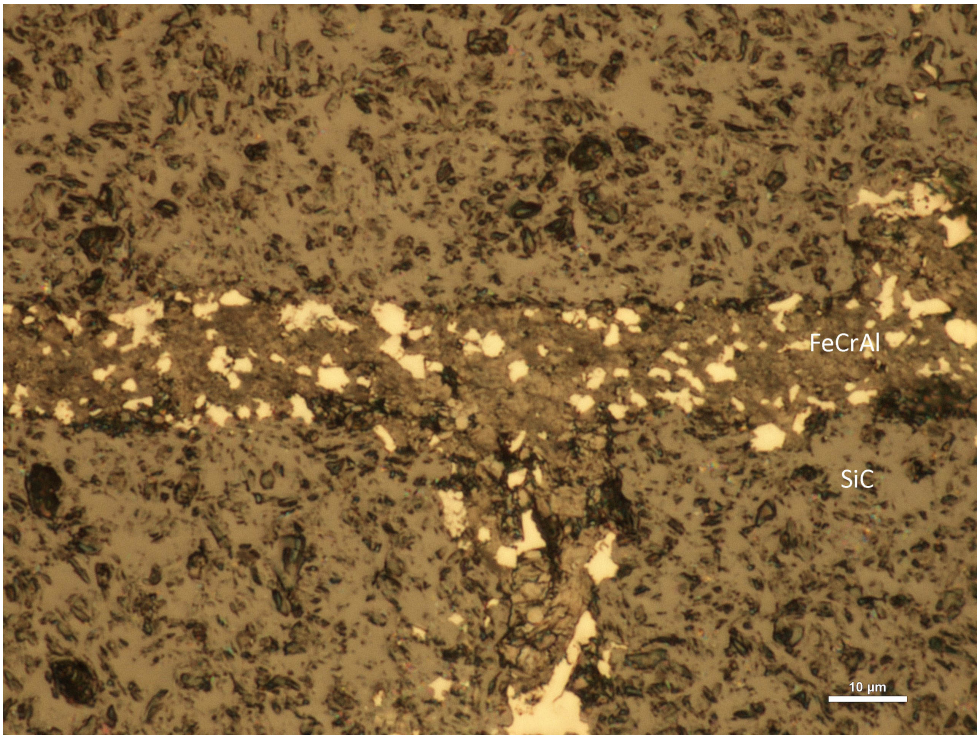


Figure D.9: Optical Micrograph of HT-Diffusion Bonded Sample 5

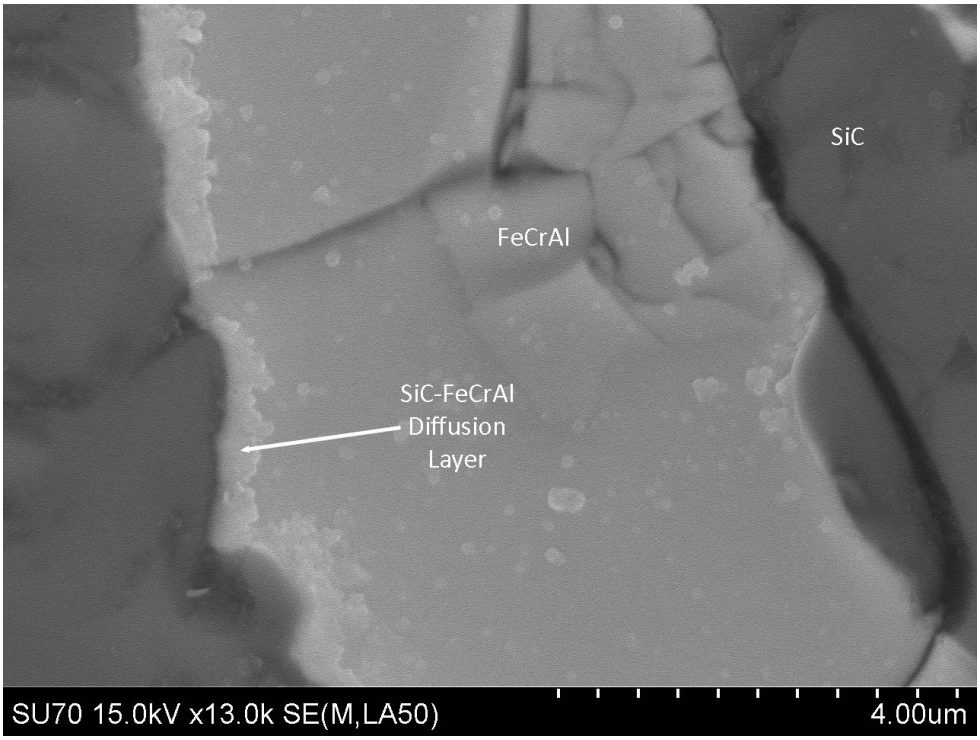


Figure D.10: SEM Image of HT-Diffusion Bonded Sample 5

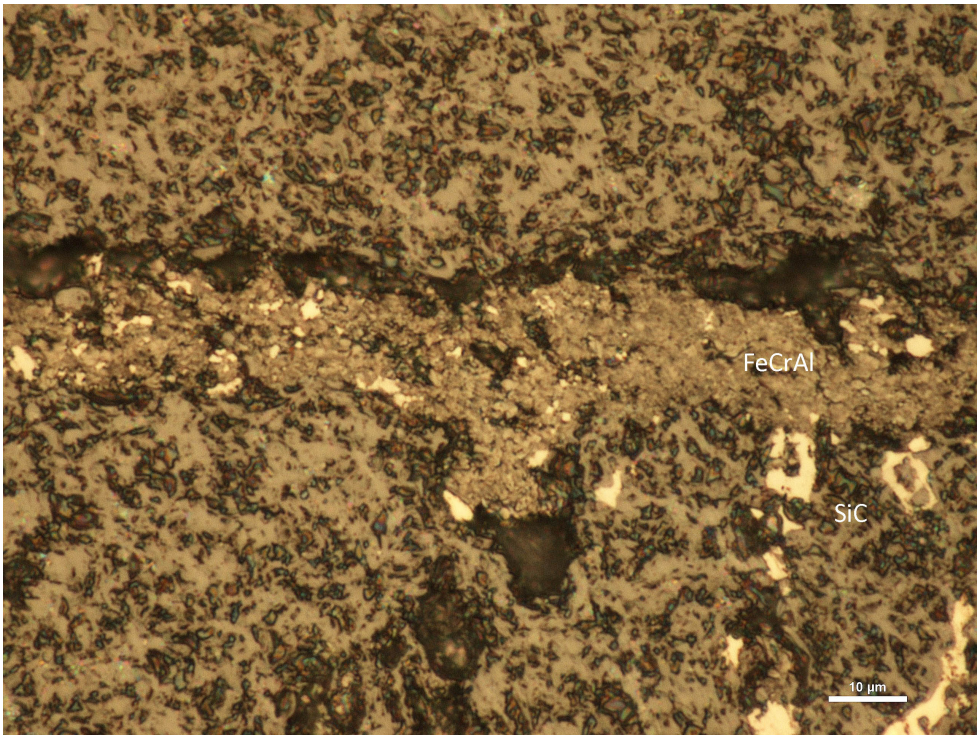


Figure D.11: Optical Micrograph of HT-Diffusion Bonded Sample 6

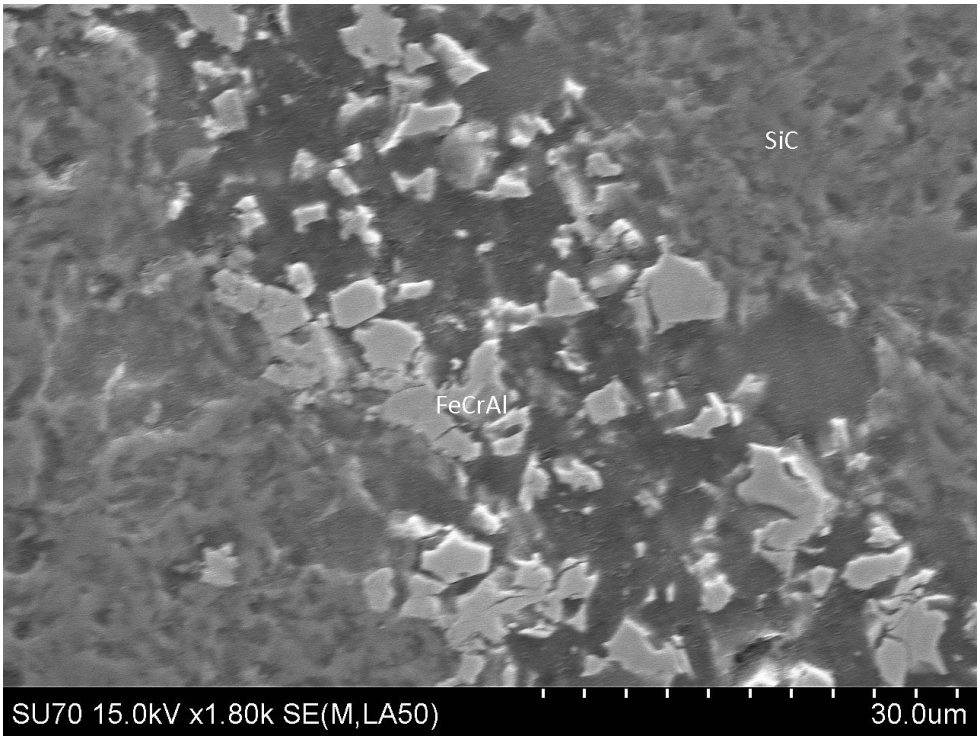


Figure D.12: SEM Image of HT-Diffusion Bonded Sample 6

# Chapter 6

# Vita

Andrew Morgan was born on the January 7, 1989, in Alexandria, Egypt, to Mr. Mofdy Morgan and Mrs. Howyda Takla. He received his high school diploma from Montrose Christian School in Rockville, MD. Later he graduated with a B.S. from Virginia Commonwealth University with a major in mechanical engineering and minors in mathematics and physics. During the senior year of Andrew's undergraduate studies, he received the Sternheimer Senior Design Award for his group capstone design project entitled, "Design and Characterization of a Needle-less Medicine Injection System". Andrew Morgan has had the honor and privilege of conducting research in the fields of polymeric materials and nuclear materials in his undergraduate and graduate studies, respectively. His current research on advanced accident tolerant fuels has been accepted into the conference of Materials Science & Technology 2014. Upon earning his M.S. in mechanical and nuclear engineering, Andrew will travel to Minneapolis to start his professional career as a design engineer at Parker-Hannifin.

This final page is intentionally left blank